# Tunable and Multiwavelength Superlenses for Infrared-Optical Subwavelength Imaging

Von der Fakultät für Mathematik, Informatik und Naturwissenschaften der RWTH Aachen University zur Erlangung des akademischen Grades eines Doktors der Naturwissenschaften genehmigte Dissertation

vorgelegt von

Master of Science

**Peining Li**

aus HuBei, China

Berichter: Universitätsprofessor Dr.rer.nat. Thomas Taubner
Universitätsprofessor Dr.rer.nat. Gero von Plessen

Tag der mündlichen Prüfung: 13.04.2016

Diese Dissertation ist auf den Internetseiten der Universitätsbibliothek online verfügbar.

# Abstract

Recently, new metamaterial-based imaging concepts, such as a perfect lens, a superlens and a hyperlens, offer great possibilities to realize sub-diffraction-limited optical imaging. However, most of these achievements have focused on the visible wavelength range. This thesis aims to develop new designs of infrared superlenses that could be used for future infrared microscopy and spectroscopy.

First, I have provided an experimental study of the basic imaging mechanism of an infrared silicon carbide (SiC) superlens. I have determined the dispersion relation of a 500-nm-thick SiC superlens through real-space optical imaging of the launched surface phonon polariton modes. The experimentally determined dispersion relation clearly reveals that the so-called 'superlensing' effect (subdiffractive imaging using the superlens) originates from the evanescent-field enhancement enabled by the surface polariton modes. Moreover, an imaging resolution of down to $\lambda/30$ ($\lambda$, the free-space wavelength) has been achieved in the same experiment. This resolution is about two times better than that reported in previous superlens experiments.

Second, I have achieved the superlensing of dielectric objects with a resolution of about $\lambda/18$. It is a significant experimental advance, because so far all reported superlens experiments are based on the imaging of metallic or strongly reflective objects that usually exhibit much stronger contrasts. Additionally, the obtained spectroscopic imaging results have also revealed that the superlensing can identify the material properties of the imaged objects. This is the first demonstration that the superlens can be used for infrared index-sensing and spectroscopic applications.

However, the SiC superlens is not suitable for broadband applications owing to a very narrow wavelength bandwidth. In order to overcome this limitation, I have proposed two new designs of infrared superlenses. The first idea is a multiwavelength superlens consisting of multiple polar dielectrics. The presented numerical investigations have demonstrated that the superlensing at multiple wavelengths can be achieved by increasing the number of phonon resonant dielectrics in the

proposed multilayered superlens system. In other words, a subwavelength object can be imaged at many different wavelengths by just one single lens. Considering the abundance of polar dielectrics, the proposed multi-wavelength superlens can cover a wavelength range from infrared to terahertz (THz) by choosing suitable materials.

The second idea is a wavelength-tunable graphene lens that can work at different wavelengths. This graphene lens due to its non-resonant enhancement of evanescent fields yields new promising properties including broad intrinsic bandwidth and low influence by the optical losses, together with a still good subwavelength resolution of around $\lambda/7$ for a two-layer case and over $\lambda/10$ for the multilayered configuration. Most importantly, the working wavelength of the graphene lens can be electrically tuned via the dynamical tuning of the graphene conductivity. This large tunability allows it to cover a broad infrared wavelength range. As a proof of this theory concept, I have experimentally demonstrated that a monolayer-graphene lens offers a 7-fold enhancement of evanescent information, improving conventional infrared near-field microscopy to resolve buried structures at a 500-nm depth with $\lambda/11$-resolution.

Moreover, I have also investigated the near-field optical imaging through a natural hyperbolic material, hexagonal boron nitride (hBN). I have demonstrated that a thin, flat hBN slab exhibits wavelength-dependent multifunctional imaging operations, offering both the superlensing of single objects with down to $\lambda/32$ resolution, as well as enabling an enlarged imaging of the outline of the object. Both imaging functionalities can be explained based on the volume-confined hyperbolic phonon polaritons propagating highly directional in hBN.

The results presented in the thesis would be useful for the development of superlens-based super-resolution infrared microscopy and spectroscopy. In particular, combing the (graphene) superlens with a conventional near-field optical microscope could have the great potential for subsurface imaging of buried subwavelength-sized objects.

# Abstrakt

Neue optische Abbildungskonzepte, wie etwa die Perfekte Linse, die Superlinse oder die Hyperlinse, bieten das große Potential, räumliche Auflösungen unterhalb des Beugungslimits zu realisieren. Ein Großteil der Errungenschaften konzentriert sich dabei jedoch auf den sichtbaren Spektralbereich. Das Ziel dieser Arbeit ist es neue Konzepte für eine infrarote Superlinse zu entwickeln, um so zukünftige Anwendungen in der Infrarot-Mikroskopie und -Spektroskopie zu ermöglichen.

Grundlegend habe ich zuerst die elementaren Abbildungs-Mechanismen einer infraroten Siliziumkarbid (SiC) Superlinse experimentell untersucht. Hierzu wurde die Dispersions-Relation einer 500 nm dicken SiC Superlinse vermessen, indem die an der Oberfläche auftretenden Surface Phonon Polariton (SPhP) Moden im Realraum abgebildet wurden. Die experimentell bestimmte Dispersions-Relation zeigt deutlich, dass der so genannte Superlinsen-Effekt (die Abbildung unterhalb des Beugungslimits mit einer Superlinse) aus der evaneszenten Feldverstärkung durch Oberflächen Polaritonen Moden resultiert. Des weiteren konnte in demselben Experiment eine räumliche Auflösung von bis zu $\lambda/30$ realisiert werden. Dieser Wert bedeutet eine Verbesserung um einen Faktor Zwei im Vergleich zu vorherigen Superlinsen Experimenten.

Ich konnte in einem zweiten Schritt auch dielektrische Objekte durch eine Superlinse mit einer räumlichen Auflösung von $\lambda/18$ abbilden. Dieses Ergebnis stellt einen signifikanten experimentellen Fortschritt dar, da in bisher allen Veröffentlichungen zur Superlinse nur metallische oder stark reflektierende Objekte, mit einem deutlich stärkeren Materialkontrast abgebildet wurden. Außerdem zeigen die gewonnen spektroskopischen Bild-Daten, dass eine Identifizierung verschiedener Materialeigenschaften mit Hilfe der Superlinse möglich ist. Dies ist der erste experimentelle Beweis dafür, dass Superlinsen für infrarote spektroskopische Anwendungen, oder für die Detektion unterschiedlicher Brechungsindizes im Infraroten genutzt werden können.

Die SiC Superlinse ist jedoch durch ihren sehr enge spektrale Bandbreite nicht für einen breiten Anwendungsbereich einsetzbar. Um diese Beschränkung zu überwinden, habe ich zwei neue Konzepte für infraroten Superlinsen vorgeschlagen. Die erste Idee besteht in einer Multi-Wellenlängen Superlinse, die durch die Verwendung von mehreren polaren Dielektrika realisiert werden kann. Die präsentierten numerischen Untersuchungen haben gezeigt, dass ein Superlinsen-Effekt bei mehrere Wellenlängen realisiert werden kann, wenn die Anzahl an Phonon-resonanten dielektrischen Schichten in einem Mehrschicht-Superlinsen-System erhöht wird. Mit anderen Worten, auch Objekte, die kleiner als die verwendete Wellenlänge sind, können bei vielen verschiedenen Wellenlängen unter Verwendung nur einer Linse abgebildet werden. In Anbetracht der Vielfalt an polaren Dielektrika, kann die vorgeschlagene Superlinse, durch Auswahl eines passenden Materials, einen Spektralbereich vom Infraroten bis hin zum Terahertz-Bereich abdecken.

Zusätzlich habe ich das Konzept einer Wellenlängen-abstimmbaren Graphen Superlinse, die bei mehreren Wellenlängen funktioniert, entworfen. Diese neue Graphen Superlinse ermöglicht aufgrund ihrer nicht-resonanten Verstärkung von evaneszenten Feldern neue vielversprechende Eigenschaften: Eine intrinsisch große Bandbreite, sowie geringe Einflüsse durch optische Verluste bei gleichzeitig guter räumlicher Auflösung unterhalb der Wellenlänge von etwa $\lambda/7$ im Zweischicht-Fall und über $\lambda/10$ für Multi-Schicht-Systeme. Von fundamentaler Bedeutung ist, dass die Arbeits-Wellenlänge der Graphen Superlinse elektrisch eingestellt werden kann über die dynamisch steuerbare Leitfähigkeit von Graphen. Dieser große Einstellbereich der Graphen Superlinse ermöglicht es einen äußerst breiten Bereich des infraroten Spektralbereichs abzudecken. Ich konnte experimentell mein theoretisches Konzept beweisen, indem ich zeigen konnte, dass eine Monolage Graphen als Linse eine siebenfache Verstärkung von evaneszenten Informationen, gegenüber der konventionellen infraroten Nahfeldmikroskopie an vergrabenen Strukturen in einer Tiefe von 500 nm bei einer räumlichen Auflösung von $\lambda/11$ bietet.

Außerdem habe ich die Nahfeld-Abbildung durch ein natürlich hyperbolisches Material, hexagonales Bor Nitrid (hBN), untersucht. Ich konnte zeigen, dass ein dünnes flaches hBN-Plättchen Wellenlängen-abhängige Multifunktions Abbildungsoperationen ermöglicht. Es war sowohl möglich durch den Superlinsen-Effekt einzelne Objekte mit einer räumlichen Auflösung von bis zu $\lambda/32$ aufzulösen,

als auch ein vergrößertes Abbild des Umrisses der einzelnen Objekte zu erzeugen. Beide Funktionalitäten lassen sich auf die räumlich eingeschränkten hyperbolischen Phononen Polaritonen zurückführen, die äußerst gerichtet in hBN propagieren.

# Contents

**Abstract** **iii**

**Abstrakt** **v**

**Contents** **viii**

**1 Background and motivation** **1**
1.1 Diffraction limit and sub-diffraction-limited optical imaging . . . . . 1
1.2 Perfect lens, superlens and hyperlens . . . . . 3
1.3 Motivation and outline of this thesis . . . . . 9

**2 Surface polariton modes in superlens** **11**
2.1 Introduction of surface polaritons . . . . . 11
2.1.1 Plasmon polaritons on a metal/dielectric surface . . . . . 11
2.1.2 Plasmon polaritons in dielectric/metal/dielectric waveguide . 13
2.1.3 Phonon polaritons in polar crystals . . . . . 14
2.2 Surface-polariton enhancement in superlens . . . . . 16

**3 Scattering-type scanning near-field optical microscope (s-SNOM) 21**
3.1 Introduction . . . . . 21
3.1.1 Basic setup . . . . . 21
3.1.2 Background suppression . . . . . 22
3.1.3 Mid-infrared laser sources . . . . . 23
3.2 Tip-sample interaction in s-SNOM . . . . . 24
3.2.1 Point-dipole model . . . . . 24
3.2.2 Superlens combined with the s-SNOM . . . . . 27

**4 Dispersion mapping and dielectric-object imaging with a SiC superlens** **29**
4.1 Mapping phonon polaritons in SiC superlens . . . . . 29
4.2 Imaging dielectric objects with the SiC superlens . . . . . 35
4.2.1 Experiments and results . . . . . 35
4.2.2 Understanding and Discussions . . . . . 41
4.3 Conclusion . . . . . 45

**5 Multiwavelength superlens with different phonon-resonant materials 47**
5.1 Introduction and basic idea . . . . . 47
5.2 Results of InSb-SiC superlens . . . . . 49
5.3 Multiple-material configurations . . . . . 52
5.4 Conclusion . . . . . 55

**6 Tunable graphene lens for infrared broadband imaging 57**
6.1 Introduction of graphene plasmons . . . . . 58
6.2 Theory of tunable graphene lens . . . . . 60
6.2.1 Evanescent-field enhancment in a graphene lens . . . . . 60
6.2.2 Bandwidth, tunability and loss-influence . . . . . 65
6.2.3 Multilayered configurations . . . . . 68
6.2.4 Hybrid graphene-superlens imaging system . . . . . 70
6.3 Experiments on graphene-enhanced near-field imaging . . . . . 72
6.4 Conclusion . . . . . 80

**7 Near-field imaging through a natural hBN hyperlens 83**
7.1 Introduction . . . . . 84
7.2 Theory and simulations . . . . . 87
7.3 Experiments of near-field imaging through hBN . . . . . 90
7.3.1 Experimental results in Type I hyperbolic band . . . . . 90
7.3.2 Experimental results in Type II hyperbolic band . . . . . 93
7.4 Near-field focusing and waveguiding by hBN . . . . . 97
7.5 Conclusion . . . . . 99

**8 Summary and outlook 101**
8.1 Summary . . . . . 101
8.2 Outlook . . . . . 103

## Appendix

**A Sample preparation 109**

**B Theory Modeling 111**

**C Supplementary data 115**

**Bibliography 117**

**List of Own Publications 135**

**Acknowledgements 137**

# 1 Background and motivation

## 1.1 Diffraction limit and sub-diffraction-limited optical imaging

In the year of 1873, Ernst Karl Abbe pointed out the fundamental diffraction limit that the optical resolution of classic imaging systems is restricted by the wavelength $\lambda$ as [1]

$$d = \frac{\lambda}{2n\sin\theta} \tag{1.1}$$

where the term $n\sin\theta$ is the so-called the numerical aperture (NA). For instance, the Abbe limit is $d \approx 180$ nm for the case with a green illumination light (around 500 nm) and a NA of 1.4. A more intuitive picture for understanding this fundamental limit can be learned from the diffraction pattern generated by light from two point-objects, which is displayed in Fig. 1.1. When the distance $d$ between the maxima of the two corresponding Airy patterns is larger than the distance between the first minimum and the central maximum (Fig. 1.1a and b), the two points are distinguishable. Otherwise, they cannot be optically distinguished (Fig. 1.1c). This phenomenon is usually used to define the optical resolution for a classical optical lens as

$$d = \frac{1.22 f_{\mathrm{L}} \lambda}{D} \tag{1.2}$$

where $f_{\mathrm{L}}$ is the focal length of the lens and $D$ is the lens diameter.

The basic physics behind the resolution limit is the fast decay of evanescent fields that contain high-spatial-frequency information of the object. As a simple example, we consider a plane light wave with an electric field (unity magnitude) as $E = e^{ik_z z}$, travelling in the free space ($n = 1$, wavevector $k_0 = 2\pi/\lambda$) along the $z$-direction. Here the time dependence $e^{-i\omega t}$ is suppressed. $k_z = \sqrt{k_0^2 - k_x^2}$ is the out-plane wavevector. $k_x$ is the in-plane wavevector that indicates the lateral

distribution of spatial-frequency components. For the components with $k_x < k_0$, the magnitude of the fields does not decay with the increase of the propagation distance $z$. They are usually referred to the **propagating fields** that can be probed by classical far-field optical lenses. On the other hand, for the components of $k_x > k_0$, their magnitude ($|E| = e^{-|k_z|z}$) will exponentially decay with the increase of $z$ (Fig. 1.2a). These non-propagating fields are the so-called **evanescent fields**. The exponential decay of evanescent fields (carrying the high-spatial-frequency information) results in a limited optical resolution in the conventional far-field optical microscope.

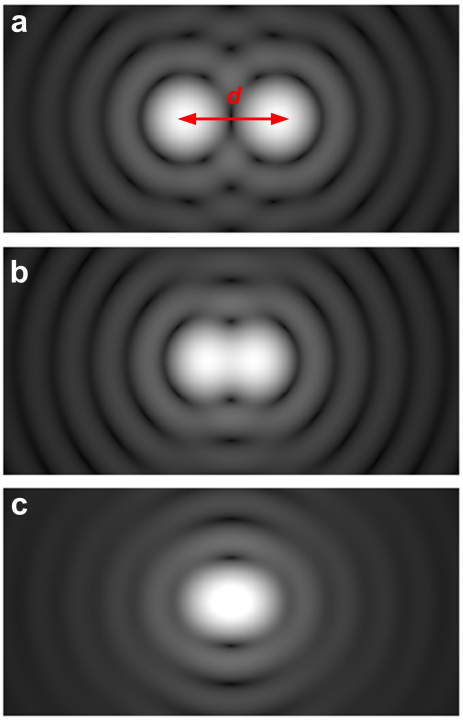


FIGURE 1.1: Airy diffraction patterns from two separated point-objects. Points far apart (a) or at the Rayleigh criterion (b) can be distinguished. Points closer than the Rayleigh criterion (c) are difficult to distinguish. (Adapted from the image of Spencer Bliven[1])

In order to improve the optical resolution, many great ideas of achieving super-resolution optical microscopy have been created. One of the most intuitive idea is to decrease the wavelength of light. This inspires the invention of ultraviolet microscope (August Köhler and Moritz von Rohr, 1904) and electron microscopes

[1]Wikipedia/Angular resolution: en.wikipedia.org/wiki/Angular resolution

[2, 3] that can be considered to use a electron beam with much smaller 'wavelengths'. Although these methods can achieve the high-resolution imaging, they do not break the diffraction limit and are still restricted by the wavelength.

Sub-diffraction-limited optical imaging methods have been also developed, which may be classified into two main categories [4]. One of them is based on special experimental techniques (e.g., color-dependence, temporal, nonlinear responses) to reconstruct a super-resolution image, such as STED [5], PALM [6], STORM [7], etc. These functional super-resolution techniques usually relying on specific molecules are widely used for imaging biological samples.

The other group of super-resolution techniques tries to capture or restore the evanescent fields, such as the scanning near-field optical microscope (SNOM) [8, 9] and the perfect lens [10]. The SNOM relies on a tiny aperture [8] or a sharp tip [9], which is coupled with a laser source. By scanning this tiny probe on the sample surface and directly collecting evanescent fields of the sample in the near field, it can construct a high-resolution near-field optical image. The resolution of the SNOM is no longer limited by the wavelength, but restricted by the size of the probe, which can reach the 10-nm scale(see Chapter 3). However, the SNOM measurement is usually time-consuming due to the pixel-by-pixel scan. In addition, its scanning area is usually less than $100\times100$ $\mu$m$^2$. Thereby, it is not suitable for the applications requiring real-time, large-area imaging.

## 1.2 Perfect lens, superlens and hyperlens

**Perfect lens.** The perfect lens proposed by Pendry [10] would provide a way to probe a large-area, real-time optical image with unlimited resolution. This concept is based on a material with a negative refraction index (both permittivity and permeability are negative), which does not exist in the nature. The underlying physics behind its unlimited resolution can be understood by the 'amplification' of evanescent fields in the negative-index material. We now consider the plane light wave $E \propto e^{ik_z z}$ propagates in a medium with a negative refraction index of $n = -1$. For evanescent components with $k_x > k_0$, the electric field in the negative-index medium becomes as $E \propto e^{|k_z|z}$ [10]. The magnitude of the evanescent field will be amplified with increasing distance $z$ (Fig. 1.2b). Therefore this slab of the

negative-index material can compensate the decay of evanescent fields and restore a super-resolution image that contains the high-$k_x$ information of the object.

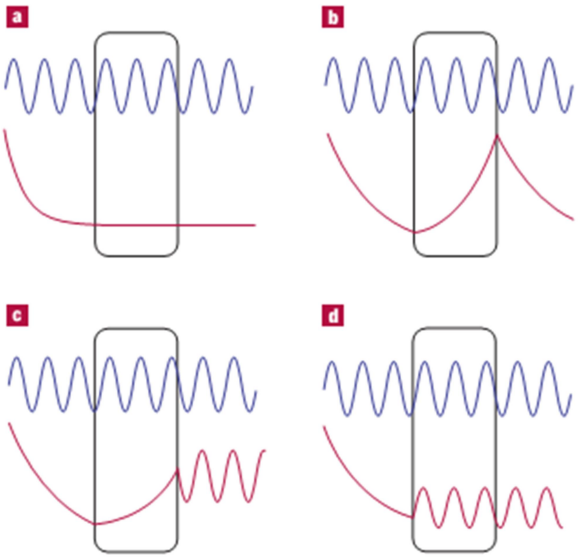


FIGURE 1.2: Propagating waves (blue lines) and evanescent waves (red lines) in various optical lenses: (a) conventional lens, (b) perfect lens (superlens). (c) far-field superlens, (d) hyperlens. Taken from [11]

However, it is known that the negative-index material does not exist in the nature (Noting that negative refraction can happen in some natural anisotropic crystals [12–14]). The lack of candidate materials makes the fabrication of such a planar device to be challenging. Artificial metamaterials could offer a possibility to realize the perfect lens [15–20]. However, substantial absorption losses (namely large imaginary parts of permittivity and permeability) of the metamaterial will dramatically limit the resolution of the perfect lens.

**Superlens.** A practical version of the perfect lens is the so-called superlens [10]. It is a thin slab (thickness $d$) of a material with a negative permittivity ( $\epsilon_{\mathrm{SL}} < 0$) sandwiched by two dielectric layers (each layer thickness $d/2$, permittivity $\epsilon_{\mathrm{diel}} > 0$). At the matching condition of $\epsilon_{\mathrm{SL}}(\lambda) = - \mid \epsilon_{\mathrm{diel}}(\lambda) \mid$, the superlens can support resonant surface polariton modes for enhancing the evanescent fields and perfectly restoring a sub-diffraction-limited image (this will be explained in Chapter 2). Importantly, materials with a negative permittivity can be easily found, such as metals at frequencies below their plasma frequencies or polar crystals in their Reststrahlen bands. So far, the superlens has been experimentally

proved in several ways [16, 21–26], such as a silver superlens in the ultraviolet regime ($\sim \lambda/5$-resolution, Fig. 1.3 a-c) [22], a SiC superlens at mid-infrared frequencies ($\sim \lambda/15$-resolution, Fig. 1.3 d-f) [24], and mid-infrared perovskite-based [25, 26] and doped-semiconductor-based [27] superlenses.

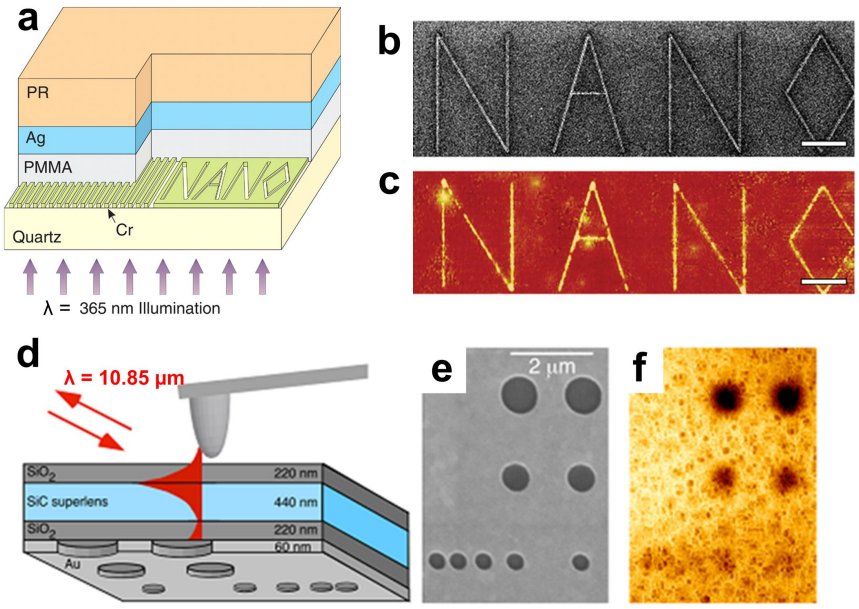


FIGURE 1.3: Experimental demonstrations of the superlens. (a) Sketch of a ultraviolet silver superlens experiment. A silver layer is used as a superlens at the wavelength of 365 nm. A PMMA layer works as a spacer layer between the silver superlens and the object structures made by focused in-beam (FIB) milling. The superlens-formed optical images are recorded by a photoresist layer. (b) Scanning electron microscope (SEM) image of the object ("Nano" structures made by FIB with a 40-nm linewidth). (c) Atomic force microscopy (AFM) image of the developed image on photoresist with the silver superlens. (d) Schematic of a mid-infrared SiC superlens experiment. A 440-nm SiC layer works as a superlens at the wavelength of about 10.85 $\mu$m. Two $SiO_2$ layers with each thickness of 220 nm are used for matching the required superlensing condition. The s-SNOM tip is used to collect the superlens-reconstructed images. (e) SEM image of the investigated object − subwavelength holes with different diameters). (f) Infrared SNOM amplitude image through the SiC superlens. Taken from [22] and [24].

The superlens is a near-field imaging device. This is because evanescent fields are enhanced only inside the superlens. They decay again outside the superlens and cannot propagate to the far field (Fig. 1.2 b). Therefore, the super-resolution image restored by the superlens needs to be collected in the near field [22, 24] or be projected to the far field by some designed surface scatters [28–31]. For example,

in Ref. [24], a sharp tip of the scattering-type SNOM (s-SNOM) is used to probe the image formed by the SiC superlens. In ref. [28], a far-field superlens has been realized by projecting evanescent fields to high-order modes of a optical grating (Fig. 1.2 c).

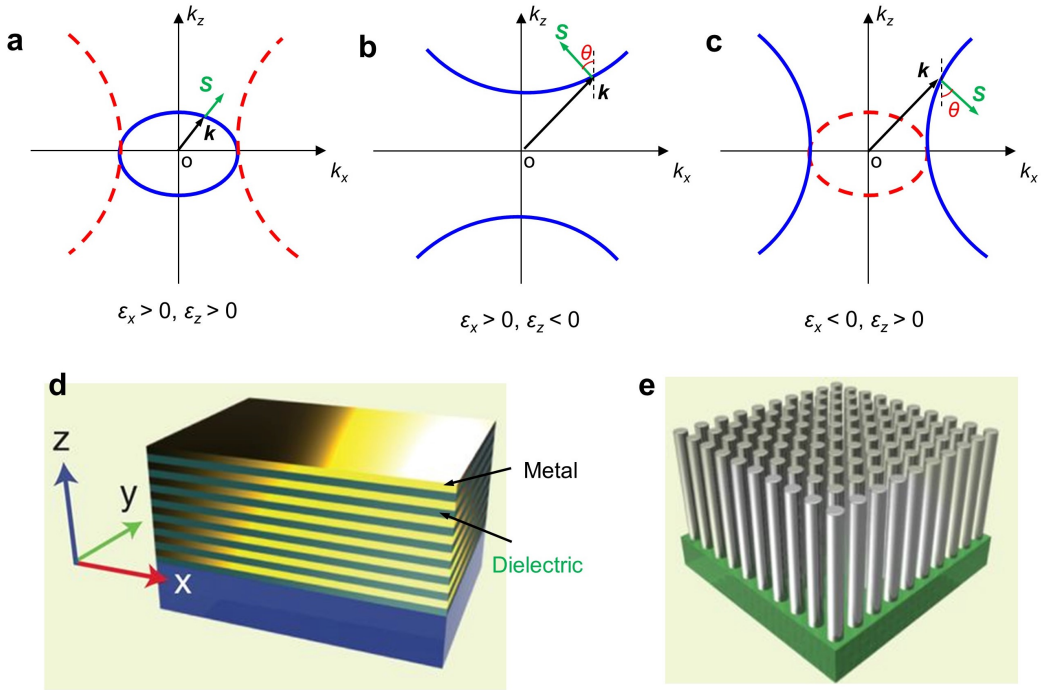


FIGURE 1.4: Hyperbolic materials. (a) In conventional anisotropic media ($\epsilon_x, \epsilon_z > 0$), the propagating fields determined by an elliptical optical dispersion ($k_x^2/\epsilon_z + k_z^2/\epsilon_x = k_0^2$, blue solid line). Outside this ellipse, the fields are evanescent (Red dashed line). Two types of hyperbolic dispersions in strongly anisotropic materials: (b) Type I, $\epsilon_x > 0, \epsilon_z < 0$ (c) Type II, $\epsilon_x < 0, \epsilon_z > 0$. $\theta$ is the angle between the Poynting vector $\boldsymbol{S}$ and the $k_z$ axis. (d) A hyperbolic metamaterial made of metal/dielectric multilayers and (e) a hyperbolic metamaterial consisting of subwavelength-sized metal wires. (d) and (e) taken from [32]

**Hyperlens.** Although the far-field superlens is capable of far-field subwavelength imaging, it still cannot provide an image magnification that is an essential functionality in conventional optical lenses. In 2006, two groups independently proposed a hyperlens concept capable of far-field magnifying subwavelength imaging [33, 34]. This new concept relies on *hyperbolic* optical dispersions in extremely anisotropic materials. It is known that the in-plane wavevector $k_x$ and the out-of-plane $k_z$ of light in an anisotropic dielectric (the in-plane permittivity $\epsilon_x$, the out-plane

permittivity $\epsilon_z$) satisfy an equation of

$$\frac{k_x^2}{\epsilon_z} + \frac{k_z^2}{\epsilon_x} = k_0^2. \tag{1.3}$$

In a normal dielectric ($\epsilon_x, \epsilon_z > 0$), the real solutions of this equation determine a closed elliptical optical dispersion (blue solid line in Fig. 1.4a), which indicate the propagating waves in the dielectric. The large wavevectors outside the ellipse have only purely imaginary solutions (red dashed line in Fig. 1.4a), which correspond to evanescent waves.

In contrast, in a material with dielectric properties of either ($\epsilon_z < 0, \epsilon_x > 0$) or ($\epsilon_z > 0, \epsilon_x < 0$), the light waves with large wavevectors can also find real solutions from the Equation 1.3. This means they become propagating in such a medium. These propagating components accordingly form two types of hyperbolic dispersions as shown in Fig. 1.4b and c. The materials with such two types of hyperbolic dispersions are usually called as hyperbolic media. Since no natural material exhibits the hyperbolic dispersion at visible optical frequencies, man-made hyperbolic metamaterials are explored in this frequency region. They are usually based on metal/dielectric multilayered structures [35, 36] and arrays of subwavelength-sized metal wires [37, 38].

Hyperbolic metamaterials have been used for rich nanophotonic applications such as hyperlensing [33–35], negative refraction [36, 37], enhanced quantum radiation [39], nanolithography [40] to sub-diffractional resonators [41]. Recently, some natural anisotropic (or indefinite) materials such as graphite [12], hexagonal boron nitride (hBN) [42, 43] and calcite [44], have been considered as natural hyperbolic material [45] with much smaller losses in different frequency ranges (most in the mid-infrared regime). Therefore these low-loss natural hyperbolic materials can provide better performances in a large variety of nanophotonic applications (see a hBN hyperlens in Chapter 7).

The hyperlens is one of the most representative applications of hyperbolic media. It is usually based on a cylindrical structure made of a multilayered hyperbolic metamaterial (Fig. 1.5a). As presented in the simulations (Fig. 1.5b), high-$k_x$ electric fields generated by two subwavelength-sized objects (two point sources) can propagate through the hyperlens due to the unique hyperbolic dispersion. More importantly, the cylindrical geometry of the hyperlens offers a magnified separation to the images reconstructed on the other side of the hyperlens. When

the separation of the images is larger than the half of the wavelength, the two objects can be imaged and resolved in the far field. The first circular hyperlens is experimentally realized in ref. [35] with about 130-nm resolution at the wavelength of 365 nm, which is based on a multilayered $Ag/Al_2O_3$ hyperbolic metamaterial. It is worth to note that another wedge-shaped hyperlens design proposed by A. Salandrino and N. Engheta [34] can also offer the possibility of far-field magnifying imaging as shown in (Fig. 1.5c and d). However, so far no experimental work has been reported for verifying this idea.

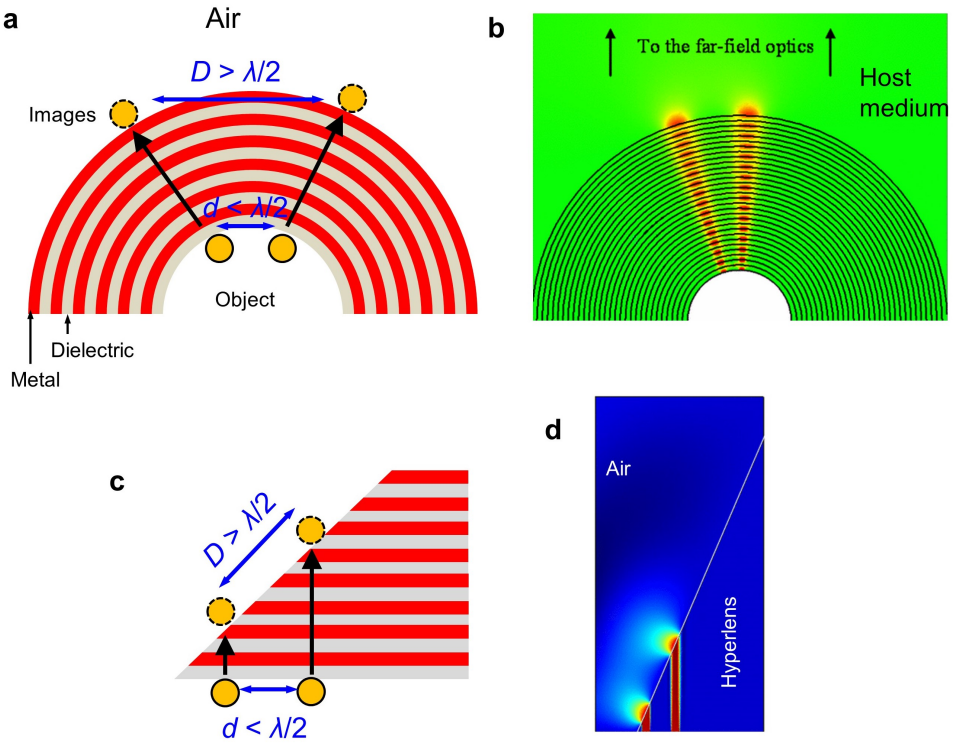


FIGURE 1.5: Two designs of a magnifying hyperlens. (a) Sketch of a circular hyperlens consisted of metal/dielectric multilayer. (b) Simulated field distribution through a circular hyperlens. The permittivities of the layers are chosen as 2 and -2, respectively. (c) Sketch of a wedge-shaped hyperlens. (d) Simulated field distribution through a wedge-shaped hyperlens made of a lossless anisotropic crystal. (b) and (d) taken from [34].

## 1.3 Motivation and outline of this thesis

It is known that the so-called 'fingerprint' region exists in the mid-infrared regime, which contains characteristic bands of molecular vibration and absorption. Infrared spectroscopy and microscopy can identify these bands for characterizing the material and chemical information of the samples. However, their spatial resolution is limited by diffraction to be several microns, which cannot be used for the characterization of nanomaterials and nanostructures. The motivation of this thesis is to understand and develop new superlenses and hyperlenses in the mid-infrared spectrum range, which could be used for large-area, real-time and high-spatial-resolution infrared spectroscopy and microscopy. The thesis is organized as following.

In Chapter 2 I give a general introduction of surface polariton modes, including surface plasmon polariton and surface phonon polariton. Using an infrard SiC superlens as an example, I also introduce that the high resolution of the superlens originates from the evanescent-field enhancement provided by resonant surface polariton modes.

Since the superlens is a near-field imaging device, in all the experiments presented in this thesis, the s-SNOM is used for reading out the superlens-restored near-field images. In Chapter 3, I give an introduction to the s-SNOM, including the basic setup and the working principle. Chapter 3 also introduces a point-dipole coupling mode for describing and interpreting the tip-sample interaction in the s-SNOM. In the last part, I discuss how the tip-sample interaction of the s-SNOM affects the read-out of the superlens-probed images.

Chapter 4 first presents an work of quantifying the dispersion relation of a 300-nm-thick infrared SiC superlens from the s-SNOM imaging of excited surface phonon polariton modes. In the second part, an experiment of using the superlens to image dielectric objects is presented and discussed.

The superlens only has a narrow bandwidth owing to the sharp dispersion relation of surface polariton modes. It is not suitable for broadband spectroscopic applications. In Chapter 5, I show an idea to extend the working wavelength range of the superlens. I theoretically propose a multilayered polar-dielectric superlens capable of sub-diffraction-limited imaging simultaneously at different wavelengths. The theory and simulation results show that the superlensing wavelengths of this

new lens can be tuned by controlling the number of polar dielectrics. Ideally, by suitably choosing polar dielectrics, the proposed superlens can have multiple working wavelengths locating in infrared and terahertz (THz) regions.

In Chapter 6, I theoretically propose that a layered 'graphene lens' enables the enhancement of evanescent waves for near-field subdiffractive imaging. Most importantly, thanks to the large tunability of graphene, this graphene lens is in principle a continuously frequency-tunable subwavelength-imaging device in the infrared and THz regions, thus allowing for ultrabroadband spectral applications. Moreover, I also experimentally demonstrate a graphene-based imaging application. I show that monolayer graphene offers a 7-fold enhancement of evanescent information, improving conventional infrared near-field microscopy to resolve buried structures at a 500-nm depth with $\lambda/11$-resolution.

In Chapter 7, I experimentally demonstrate sub-diffraction-limited optical imaging using a flat slab of the low-loss, natural hyperbolic material, hBN. This thin natural hyperlens exhibits wavelength-dependent multifunctional operations, offering both the superlens imaging of single objects with down to $\lambda/32$ resolution, as well as enabling a enlarged imaging of the outline of the object. Both imaging functionalities can be explained based on the volume-confined, wavelength dependent propagation angle of hyperbolic phonon polaritons in hBN.

Chapter 8 concludes the thesis and gives an outlook to future development prospects.

# 2 Surface polariton modes in superlens

Chapter 2 will explain the imaging mechanism of the superlensing, namely the evanescent-field enhancement provided by surface polariton modes. First, I introduce the general background of surface polariton modes in Section 2.1. Afterwards, I will discuss the role of surface polariton modes in the superlens in Section 2.2.

## 2.1 Introduction of surface polaritons

### 2.1.1 Plasmon polaritons on a metal/dielectric surface

Surface plasmon polariton (SPP) is the coupling of collective electrons (plasmon) and incident photons at a metal-dielectric interface [46, 47]. The SPP is strongly bound at the metal-dielectric interface and has the transverse magnetic (TM) nature of a electromagnetic mode. The field distribution of the SPP in the metal half space ($z < 0$ as defined in Fig. 2.1a) can be written as [46, 47]

$$E_m(x, z, t) = E_{p,0} e^{ik_x x} e^{ik_{z,m} z} e^{-i\omega t}. \tag{2.1}$$

The dielectric half space ($z > 0$) can be expressed as

$$E_d(x, z, t) = E_{p,0} e^{ik_x x} e^{ik_{z,d} z} e^{-i\omega t}. \tag{2.2}$$

$k_x = k_p$ is the in-plane wavevector of the SPP and $k_{z,j} = \sqrt{\epsilon_j k_0^2 - k_x^2}$ ($j = m, d$; $k_0 = \omega/c$) is the wavevector along the $z$-axis. $\epsilon_m$, $\epsilon_d$ are dielectric functions of the metal and the dielectric, respectively. Continuous boundary conditions of the Maxwell equations at the metal/dielectric interface requires [46, 47]

$$\frac{k_{z,m}}{\epsilon_m} = \frac{k_{z,d}}{\epsilon_d}, \tag{2.3}$$

which further leads to the well-known equation describing the dispersion relation of the propagating SPP as

$$k_p = k_0 \sqrt{\frac{\epsilon_m \epsilon_d}{\epsilon_m + \epsilon_d}}. \tag{2.4}$$

The real part of $k_p$ indicates the wavelength of the SPP, $\lambda_p = 2\pi/\mathrm{Re}(k_p)$. The imaginary part determines the propagation length ($L_p$) of the SPP as

$$L_p = \frac{1}{\mathrm{Im}(k_p)}. \tag{2.5}$$

In the lossless case (namely, $\epsilon_m$ and $\epsilon_d$ are pure real), the $k_p$ will approach infinity ($k_p \to \infty$) at the condition of $\epsilon_m + \epsilon_d = 0$ (indicated by a horizontal line in Fig. 2.1b), leading to an infinitely small wavelength ($\lambda_p \to 0$). In reality, the unavoidable material losses (in either the metal or the dielectric) results in a finite $k_p$. However, the $k_p$ of the SPP is still larger than the $k_x$ of the light in free space. Therefore, the SPPs can concentrate and confine electromagnetic energies into the subwavelength scale, resulting abundant subwavelength-optical applications [46–52].

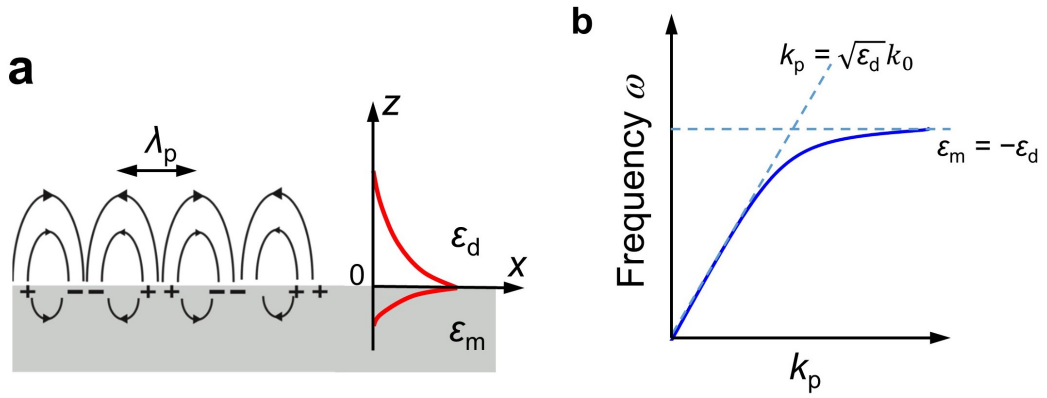


FIGURE 2.1: (a) SPP, collective oscillation of electrons with the incident electromagnetic field at a flat metal–air interface. (b) Dispersion curves of SPPs (red). Dashed line indicates light line in free space.

It should be pointed out that the SPPs on a flat metal/dielectric surface cannot directly be excited by a plane wave of light because of the mismatch of the $k_x$. In order to compensate this mismatch, various methods can be used (see an overview in [46]), such as increasing the incident angle and the index of dielectric

environment, using the diffraction effect from a grating, nanoparticle, sharp edge and rough surface, and near-field tip excitation.

### 2.1.2 Plasmon polaritons in dielectric/metal/dielectric waveguide

The SPPs can also exist in multilayers consisting of alternating metal and dielectric layers. When the separation between adjacent layers is smaller than the decay length of the SPPs, the SPP modes at different interfaces will be coupled together. Here I will discuss these coupled SPPs in a specific layered structure, which will be used for understanding the superlensing effect later in this Chapter. It is an insulator/metal/insulator (IMI) waveguide structure as depicted in Fig. 2.2, namely a thin metallic layer sandwiched between two (infinitely) thick dielectrics. The thickness of the metal film is $d$. The dispersion relation of SPPs in this system is implicitly expressed as [46, 47]

$$e^{-4k_m d} = \frac{k_m/\epsilon_m + k_{d,1}/\epsilon_{d,1}}{k_m/\epsilon_m - k_{d,1}/\epsilon_{d,1}} \frac{k_m/\epsilon_m + k_{d,2}/\epsilon_{d,2}}{k_m/\epsilon_m - k_{d,2}/\epsilon_{d,2}} \tag{2.6}$$

where $k_j = \sqrt{\epsilon_j k_0^2 - k_x^2}$ $[j = m, (d,1), (d,2)]$. For infinite thickness $(d \to \infty)$, this equation will reduce to Equation 2.3, indicating two uncoupled SPPs at the respective interfaces. For a symmetric case $(\epsilon_{d,1} = \epsilon_{d,2})$, the Equation 2.6 can be split into a pair of equations,

$$\tanh(k_m d) = -\frac{k_{d,1}\epsilon_m}{k_m \epsilon_{d,1}} \tag{2.7}$$

$$\tanh(k_m d) = -\frac{k_m \epsilon_{d,1}}{k_{d,1}\epsilon_m} \tag{2.8}$$

This pair of equations describes the dispersion relations of odd and even SPP modes (depending on that $E_x(z)$ is an odd or an even function), respectively. For example, the SPP dispersion relations of an air/silver/air layered structure has been deduced from these equations as shown in Fig. 2.2. When decreasing metal film thickness, the wavevectors of odd modes will become smaller ($k_p$ approaching $k_0$). Thus theses surface modes usually have much longer propagation length ($k_p$ close to $k_0$), which are referred to 'long-range SPPs'. In contrast, the even modes

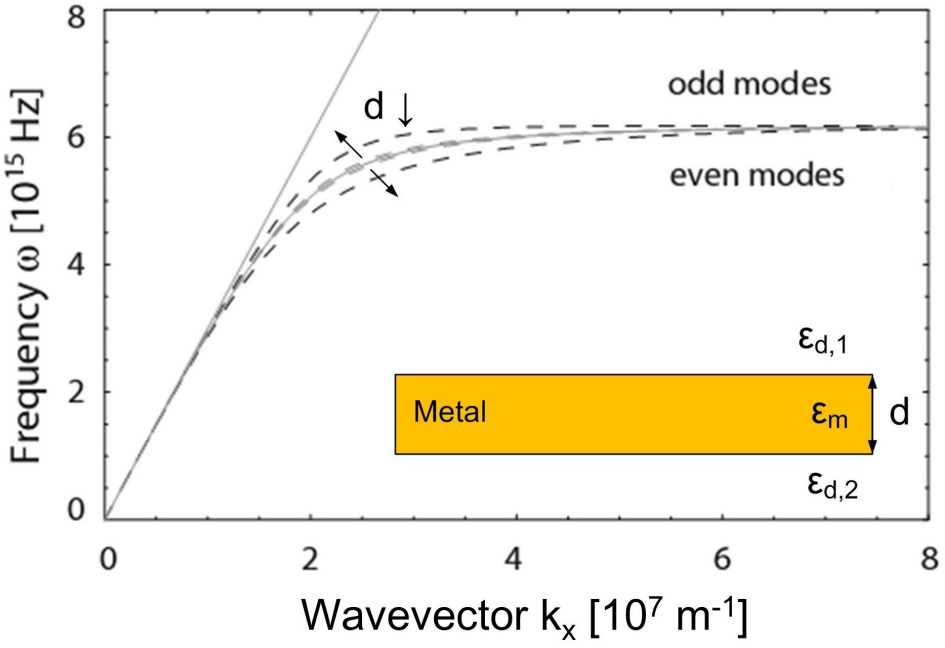


FIGURE 2.2: Dispersion relation of SPP modes in air/silver/air cases with a silverl core of thickness 100 nm (dashed gray curves) and 50 nm (dashed black curves), respectively. Also shown is the dispersion of a single silver/air interface (gray curve). Insert,the sketch of a dielectric/metal/dielectric multilayer. Adapted from [47]

exhibit the opposite behaviour - their wavevectors increase with decreasing metal film thickness, leading to a short propagation length. These coupled surface modes in thin metallic layer are the origin of local field enhancement in the superlensing effect, which I will discuss in detail later.

### 2.1.3 Phonon polaritons in polar crystals

The subwavelength-scale confinement of SPPs in noble metals can only be achieved at high frequencies (near-infrared and visible regimes). This is because the metals have large negative permittivities in mid-infrared and THz frequencies, thus resulting in that their $k_p$ is very close to the free-space $k_0$ (deduced from the Equation 2.4 using the condition of $|\epsilon_m| \gg |\epsilon_d|$). In this context, new materials are needed for low-frequency plasmonic applications.

*Polar* crystals are one of the most promising material candidates for infrared and THz plasmonics [24, 53–60]. They show '*metallic*' properties of high optical

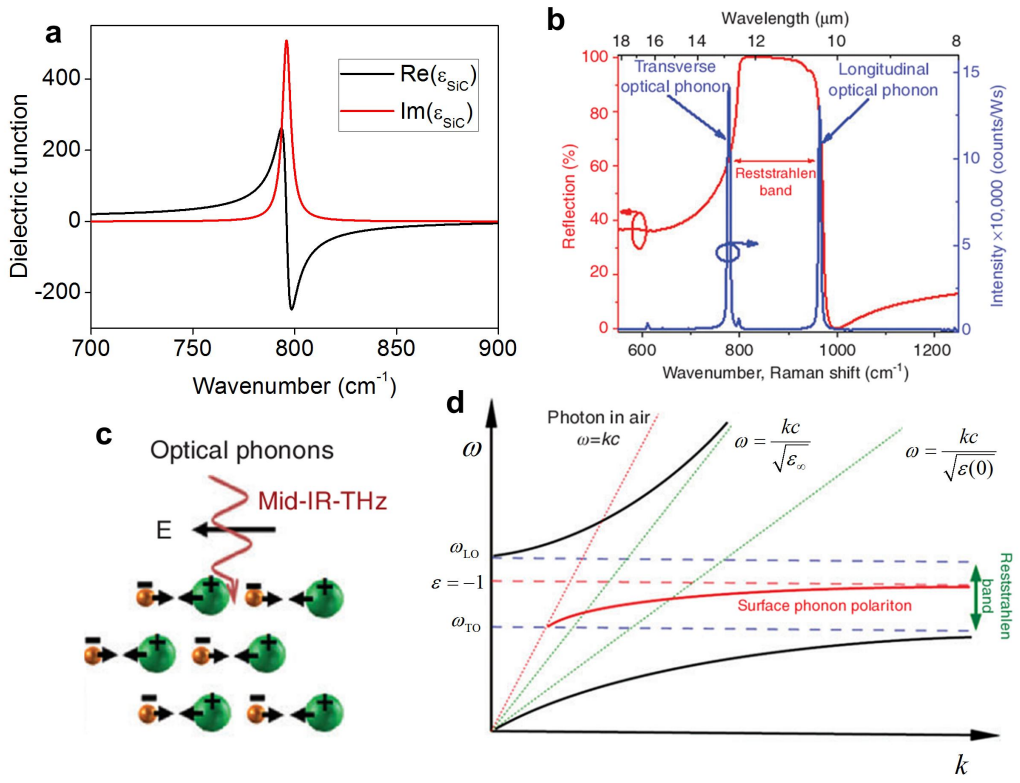


FIGURE 2.3: (a) Dilectric function of a representative polar crystal - SiC. (b) Infrared reflectivity and Raman spectra of the SiC. (c) Sketch of the optical phonon in polar crystal. (d) Dispersion relation of the SPhP in the SiC. (b-d) adapted from [53]

reflectivity (Fig. 2.3b) due to a negative real part (Fig. 2.3a) of dielectric function in the so-called *Reststrahlen* band locating in mid-infrared and THz regimes. This Reststrahlen band is the spectral range between the transverse optical (TO) phonon and longitudinal optical (LO) phonon of the polar crystal. As an example, the dielectric function of a representative polar crystal - SiC - is shown in Fig. 2.3a. This dielectric function is calculated using a Lorentz oscillator model,

$$\epsilon_{\mathrm{SiC}} = \epsilon_{\infty}(1 + \frac{f_{\mathrm{LO}}^2 - f_{\mathrm{TO}}^2}{f_{\mathrm{TO}}^2 - f^2 - if\gamma}) \tag{2.9}$$

where $\epsilon_{\infty} = 6.7$ is high-frequency permittivity. $f_{\mathrm{LO}} = 972$ cm$^{-1}$ and $f_{\mathrm{TO}} = 796$ cm$^{-1}$ are the respective longitudinal and transverse optical phonon frequencies. $\gamma = 5$ cm$^{-1}$ is the damping factor. It can be seen in Fig.2.3a that SiC has a finite negative permittivity in its Reststrahlen band between the $f_{\mathrm{TO}}$ and $f_{\mathrm{LO}}$ phonon frequencies. Due to this negative permittivity, the polar crystal supports

propagation of the surface phonon polaritons (SPhP), which is the coupling state of the incident photon and the optical phonon (collective mode of lattice vibration, see Fig. 2.3c) in the polar crystal. Similar to the SPPs in the metal at visible frequencies, the infrared SPhPs also have a polariton wavevector $k_p$ that is larger than the $k_0$ in free space (Fig. 2.3d), giving rise to the sub-diffractional confinement of electromagnetic energies. More discussions on the SPhPs can be found in a recent intensive review by J. D. Caldwell [53].

## 2.2 Surface-polariton enhancement in superlens

In order to present the role of surface polariton modes in the superlens, I first consider an infrared SiC superlens (500 nm thick) as sketched in Fig. 2.4a. The surrounding dielectric environment is air ($\epsilon_{\text{Air}} = 1$). The condition of $\epsilon_{\text{SiC}} = -\epsilon_{\text{Air}}$ for resonant surface polariton modes can be satisfied at the wavelength of about 10.5 $\mu$m. This condition is usually referred to the so-called 'superlensing condition' determining the wavelength where the superlens can achieve the best imaging resolution. I calculate the electric-field distribution of the deeply sub-diffractional component $k_x = 15.5k_0$ in this SiC superlens at the matching condition as plotted in Fig. 2.4a. It can be observed that the high-$k_x$ (evanescent) field is significantly enhanced in the superlens. This enhancement of evanescent fields allows the superlens for the reconstruction of subwavelength information of the investigated object.

The found enhancement is provided by surface polariton modes in the superlens [61]. In this case the negative-permittivity SiC superlens supports SPhP modes at its two interfaces. When the layer thickness of the superlens is smaller than the penetration depth of the SPhPs, the two modes on the top and bottom surfaces couple with each other and propagate together. In Fig. 2.4b, I plot simulated results of electric field ($\text{Re}(E_z)$) distribution in the SiC superlens at the case of $\epsilon_{\text{SiC}} = -1.7$ (lossless, for the sake of visualizing the SPhPs). Apparently, the SPhPs are found on both interfaces of the superlens. The polariton wavelength $\lambda_p$ of these SPhPs is much smaller than the free-space wavelength $\lambda_0$ ($\lambda_p \sim \lambda/5$). Therefore, by using this polariton wavelength $\lambda_p$, the superlens is able to resolve a subwavelength-sized object (relative to the free-space wavelength). In particular, at the superlensing condition, the polariton wavelength $\lambda_p$ of the SPhPs (in the lossless superlens) is infinitely small (namely, $\lambda_p \to 0$), leading to the unlimited

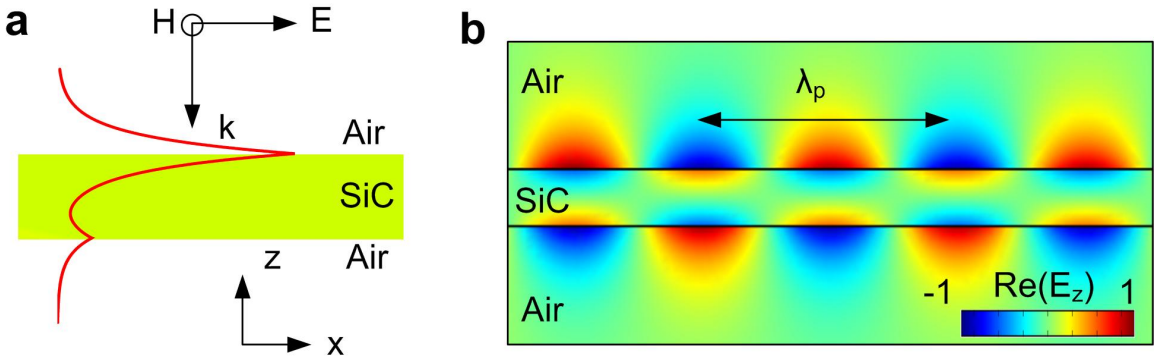


FIGURE 2.4: SPhP modes in a SiC superlens. (a) Schematic of a 500 nm thick SiC superlens. The red line plot indicates the magnitude of electric fields (with $k_x = 15.5k_0$) in the superlens at the superlesning condition $\epsilon_{\text{SiC}} = -1$. (b) Simulated field ($\text{Re}(E_z)$) distribution in the SiC superlens with $\epsilon_{\text{SiC}} = -1.7$ at the wavelength of 10.66 $\mu$m ($\lambda_p \sim 2.1$ $\mu$m).

imaging resolution of the lossless superlens. However, in practical cases, the unavoidable material losses (in either the superlens or the surrounding environment) results in an limited imaging resolution of the superlens.

The enhancement of the SPhP modes can be well presented by means of evaluating the transmission of high-$k_x$ fields through the superlens. As displayed in Fig. 2.5a, I consider two superlens configurations: the matched sandwich [Air (250 nm)-SiC (500 nm)-Air (250 nm)] and the single-layer 500-nm SiC superlens. I calculate the transmission coefficient $|T(\lambda_0, k_x)|$ through those two respective configurations at the superlensing wavelength of 10.5 $\mu$m ($|T_{\text{Air-SiC-Air}}|$ for the sandwich, $|T_{\text{SiC}}|$ for the single-layer SiC). The absorption loss in the SiC dielectric function is included, namely the damping of $\gamma = 5$ cm$^{-1}$. The calculated results are plotted in Fig. 2.6b, which are compared to the case of electric field propagating in free space ($T_{\text{Air}}$, black line). Both the single-layer (red line) and sandwiched (blue line) superlens have significant transmission enhancement of high-$k_x$ fields. However, the enhancement in the sandwiched case is much lower than the single-layer SiC superlens, e.g., for $k_x = 10k_0$, $|T_{\text{Air-SiC-Air}}/T_{\text{Air}}| = 7.5$ and $|T_{\text{SiC}}/T_{\text{Air}}| = 146$, while $|T_{\text{Air}}| = 0.05$. This is because the enhanced high-$k_x$ field will have a fast decay in the additional (250-nm) air layer. This decay suppresses an 'over-amplification' (the peak at $k_x \sim 10k_0$) caused by the SPhP mode in the single-layer SiC case,

resulting in a relatively flat and uniformly enhanced transmission spectra for all different $k_x$ components ($|T_{\text{Air-SiC-Air}}| \approx 1$ until $k_x = 5k_0$). The uniformly enhanced transmission enables for a nearly perfect reconstruction of the object information without potential imaging distortions.

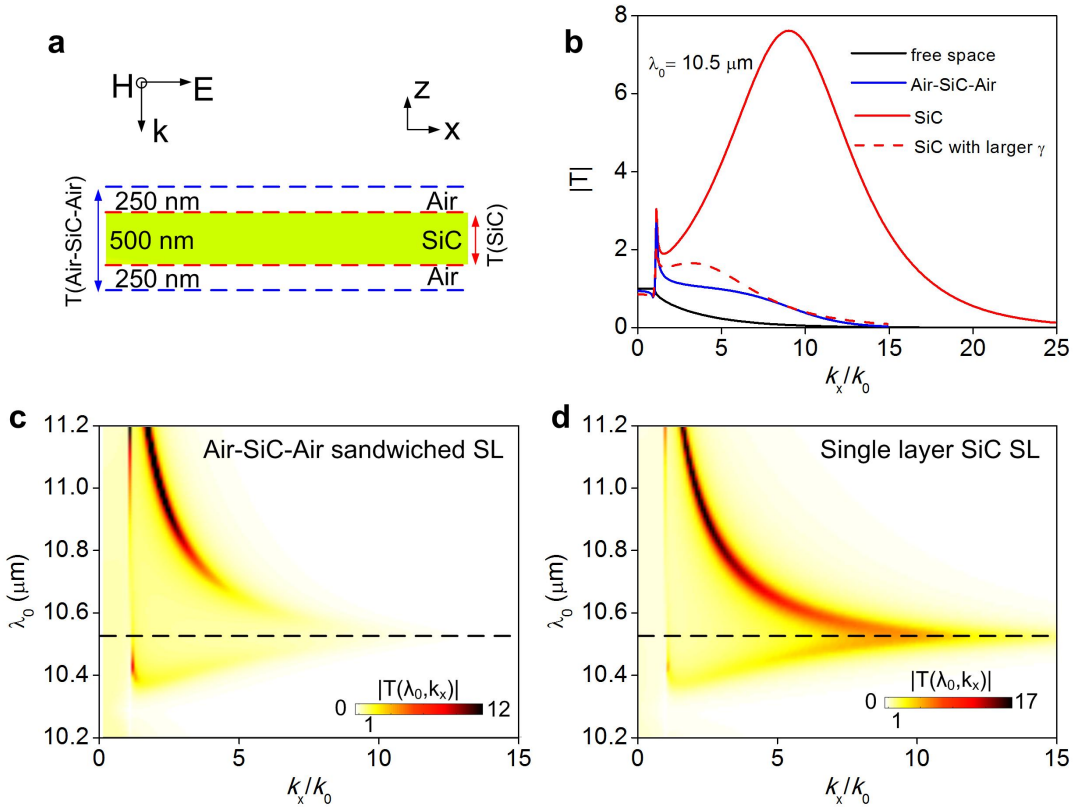


FIGURE 2.5: (a) Sketch of the free-standing 500-nm-thick SiC superlens in air. Two imaging configurations can be used in this superlens: the matched Air(250 nm)-SiC (500 nm)-Air (250 nm) case and the single-layer SiC superlens. (b) The transmission coefficient $|T(\lambda_0, k_x)|$ through the two respective configurations at the superlensing wavelength of 10.5 $\mu$m (Red line, $|T_{\text{Air-SiC-Air}}|$ for the sandwich. Blue line, $|T_{\text{SiC}}|$ for the single-layer SiC). For comparison, red dashed line presents the transmission through a 500-nm single-layer SiC with larger damping ($\gamma = 30$ cm$^{-1}$). Black line shows the case of propagating the 500-nm distance in free space. Transmission coefficient of the SiC (500 nm thick) superlens as a function of the wavelength and the wavevector $k_x$ for (c) the sandwiched case and (d) the single-layer SiC case. Dashed horizontal lines in (c) and (d) mark the superlensing wavelength for $\epsilon_{\text{SiC}} = -\epsilon_{\text{Air}}$.

Although the transmission of the single-layer SiC superlens is obviously distorted by the over-amplification of SPhP modes, its much stronger enhancement could lead to stronger signal strengths in practical measurements. Furthermore, when

the SiC layer has larger absorption losses (e.g., damping $\gamma = 30$ cm$^{-1}$), the distortion introduced by the SPhP mode can be suppressed (see red dashed line in Fig. 2.5b). Therefore, this single-layer configuration could still be useful for practical applications. In Fig. 2.5c and d, I also plot the transmission coefficient as a function of the wavelength and the wavevector for the sandwich and the single-layer case, respectively. The high transmission peaks of the high-$k_x$ ($k_x > k_0$) components are observed in both plots, which corresponds to the SPhP modes. It is seen that the SPhP mode is more pronounced in the single-layer case, which suggests that this configuration will be more suitable for the purpose of imaging SPhP modes in the superlens (see Chapter. 4).

# 3 Scattering-type scanning near-field optical microscope (s-SNOM)

## 3.1 Introduction

As introduced in Chapter 1, the superlens-restored high-resolution images still locate in the near field. In order to read out these near field images, scattering-type scanning near-field optical microscope (s-SNOM) is usually used [24–26]. Here I will introduce the basic setup and mechanism of the s-SNOM.

### 3.1.1 Basic setup

Generally, the imaging mechanism of the s-SNOM is due to the scanning of a sharp metallic tip across the sample surface. This tip is illuminated by a mid-infrared light source. Due to the optical antenna effect, the tip converts the free-space incident light into strong localized near field below the tip apex [54]. Therefore, the tip works as a near-field 'lightning-rod' probe [62] to examine the sample area of interest. By collecting the tip-backscattered light, the high-resolution near-field image can be recorded. The resolution of the s-SNOM depending on the tip size is usually about 20 to 30 nm.

In this thesis the used s-SNOM is is commercially available from Neaspec GmbH, which is based on a tapping-mode AFM [54, 63]. The basic setup of the s-SNOM is shown in Fig. 3.1. A zinc selenide beam splitter separates the infrared laser into two optical paths. One path is guided to a parabolic mirror (numerical aperture: 0.46, focal length: 11 mm), which focuses the laser beam to the AFM tip (Pt-coated tip from Nanoworld). Due to this mirror focusing, the focused light has an angle of 50° - 60° with respect to the direction normal to the sample surface. The

tip working as an optical antenna resulting in a strong near-field interaction [54]. The s-SNOM works in reflection mode. Namely, backscattered (reflected) light is collected by the same parabolic mirror. Another optical path is the reference beam path of a Michelson interferometer, which ends at a movable reflection mirror oscillating with a frequency of $f \sim 300$ Hz. Both beams are guided to a liquid nitrogen cooled MCT (mercury cadmium telluride) infrared detector. In a practical measurement the position of the s-SNOM tip is fixed, the sample is scanned by a motorized sample stage. The s-SNOM tip (radius $a \sim 30$ nm) vibrates at a tapping frequency of $\Omega \sim 270$ kHz with an amplitude of several 10 nm. The detector signals are demodulated at higher harmonic $n\Omega$ (usually, $n = 2$ or 3) in order to suppress the background (cf. Sec. 3.1.2). Near-field optical amplitude $s_n$ and phase $\varphi_n$ were separated with the used interferometric setup and a lock-in amplifier [63].

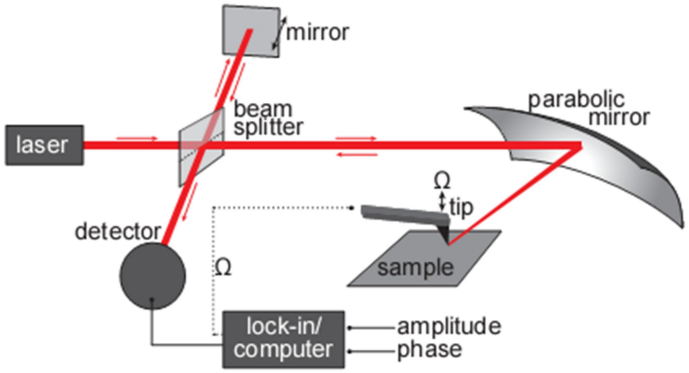


FIGURE 3.1: Experimental setup of the infrared s-SNOM. A metallic sharp tip under the infrared laser scans at the sample surface. This tip works as a near-field probe to collect optical information from the scanned sample surface. The collected backscattered light is analysed with an interferometric setup and a lock-in. Taken from [64].

### 3.1.2 Background suppression

In s-SNOM the useful optical signals are the scattered fields ($E_{\text{sca}}$) from the tip end. However, the collected backscattered light also contains substantial background fields ($E_{\text{bg}}$), either reflection fields of the upper tip shaft, or reflection fields from the surrounding sample areas. In order to suppress the background

from the detected light signals, an important method is the tip modulation (oscillation with the frequency $\Omega$). The near fields generated from the tip end have a strong non-linear decay on the length scale of 100 nm. On the other hand, the background fields are generally diffraction-limited fields that have a weak decay in the regime of the tip oscillation (several 10 nm). Therefore the background signals can be suppressed at higher Fourier components ($n\Omega$, $n > 1$) of the time-dependent detector signals.

However, since the detector only records the field intensity $I$, which is the square of the electric fields as $I \propto |E_{\mathrm{sca}} + E_{\mathrm{bg}}|^2$. The term of $E_{\mathrm{sca}} \cdot E_{\mathrm{bg}}$ containing both the near-field signal and the background cannot be suppressed by the tip modulation and the detector demodulation. In order to suppress this *multiplicative* background, I use the so-called *pseudoheterodyne* detection scheme [63], which use a a phase-modulated reference beam to interfere with the tip-scattered light. As introduced in Fig. 3.1, the end mirror in the reference beam path is set to oscillate with a frequency of $f \sim 300$ Hz ($f \ll \Omega$) by a piezoelectric actuator. This additional mirror modulation creates sidebands at the frequency of $n\Omega \pm mM$ in the Fourier transform of the detector signals. By comparing the higher $m$-order components ($m \geq 1$) with the component of $n\Omega$, the multiplicative background $E_{\mathrm{sca}} \cdot E_{\mathrm{bg}}$ can be avoided. This enables a complete background-free near-field optical detection [63].

### 3.1.3 Mid-infrared laser sources

The experiments presented in this thesis rely on different mid-infrared lasers, including $CO_2$ lasers, quantum cascade lasers (QCL) and a tunable broadband laser.

The $CO_2$ gas lasers (from Edinburgh Instruments) are filled with $^{12}C^{16}O_2$ and $^{12}C^{16}O_2$ gases. The wavelength of the $CO_2$ lasers are line tunable with a tunable grating at one end of the cavity, which have the output laser wavelengths spanning from about 890 $cm^{-1}$ to about 1080 $cm^{-1}$ (but with several wavelength gaps). The output power of the $CO_2$ gas lasers can be up to 6 W. During the measurements the power is attenuated to less than 10 mW (by infrared attenuators, from Lasnix).

The QCLs are semiconductor lasers based on inter-subband transitions between different quantum states in layered heterostructure quantum wells [65]. The output wavelength is also tunable with a grating of the laser cavity. In our laboratory the

six laser heads nearly cover the wavelength ranging from 900 $cm^{-1}$ to 1900 $cm^{-1}$. The laser power of QCLs can be several 100 mW.

A tunable broadband laser is also used for the broadband s-SNOM. The laser system was developed at Fraunhofer Institute for Laser Technology (ILT) [66, 67]. It consists of a commercially available ps-laser as the pump source and two subsequent nonlinear converter steps to cover the mid-infrared range. The peak wavelength is continuously tunable from $\omega = 625$ $cm^{-1}$ ($\sim 16$ $\mu$m) to $\omega = 1100$ $cm^{-1}$ ($\sim 9$ $\mu$m) with bandwidths of some tens to more than hundred wavenumbers. At a repetition rate of 20 MHz and pulse duration of 10 ps, the system provides an average power of up to 10 mW. In the broadband s-SNOM, for spectral analysis, the position of the sample is kept constant, while the reference mirror is continuously moved to record interferograms. The spectral information is then extracted by complex Fourier transformation. More detailed introduction of the broadband s-SNOM can be found in [67–69].

## 3.2 Tip-sample interaction in s-SNOM

### 3.2.1 Point-dipole model

The tip-sample interaction in the s-SNOM is usually described by a simple point-dipole model [54, 70, 71], which can provide a qualitative understanding of the s-SNOM imaging mechanism. As sketched in Fig. 3.2a, the s-SNOM tip is scanning on a sample surface (permittivity $\epsilon_s$) under the incident field $E_i$. The s-SNOM tip can be represented by a point dipole at the tip end with a sphere radius $a$ fitting the apex curvature. For the tip permittivity $\epsilon_t$ the dipole polarizability is expressed as [72]

$$\alpha = 4\pi a^3(\epsilon_t - 1)/(\epsilon_t + 2). \tag{3.1}$$

The resulting dipole moment is

$$p = \alpha E_i \tag{3.2}$$

This tip dipole will induce a 'mirror image' dipole in the sample as $p' = \beta p$, where $\beta$ is the quasi-static reflection coefficient [72],

$$\beta = (\epsilon_s - 1)/(\epsilon_s + 1) \tag{3.3}$$

The distance between the tip dipole and the image dipole is assumed to be $L = 2(a + h)$. For the case that the applied electric field $E_\mathrm{i}$ is perpendicular to the sample surface, the electric field induced by the image dipole at the position of the tip dipole is

$$E_\perp = \frac{p'}{2\pi L^3} \tag{3.4}$$

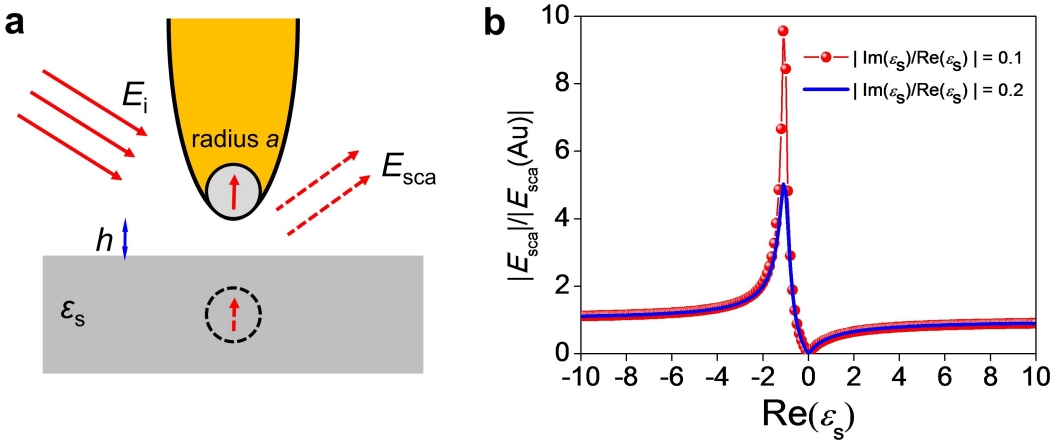


FIGURE 3.2: (a) Sketch of the point-dipole tip-sample coupling model. (b) Calculated s-SNOM signal $E_\mathrm{sca}$ (normalized to the s-SNOM signal $E_\mathrm{sca}$(Au) from a Au substrate) as a function of the sample permittivity $\epsilon_\mathrm{s}$.

The tip dipole moment is expressed as [71]

$$p = \alpha(E_\mathrm{i} + \frac{p'}{2\pi L^3}) = \frac{\alpha}{1 - \dfrac{\alpha\beta}{16(a+h)^3}} E_\mathrm{i} \tag{3.5}$$

Now the overall dipole is the superposition of $p + p'$, which introduces an effective polarizability for indicating the tip-sample interaction as

$$\alpha_{\mathrm{eff},\perp} = \frac{\alpha(1+\beta)}{1 - \dfrac{\alpha\beta}{16(a+h)^3}} \tag{3.6}$$

For the case that $E_\mathrm{i}$ is parallel to the sample surface, the polarizability changes to [71]

$$\alpha_{\mathrm{eff},\parallel} = \frac{\alpha(1-\beta)}{1 - \dfrac{\alpha\beta}{32(a+h)^3}} \tag{3.7}$$

In reality, the s-SNOM tip is elongated along the direction perpendicular to the sample surface. The contribution of $\alpha_{\text{eff},\perp}$ dominates and $\alpha_{\text{eff},\parallel}$ is usually neglected.

**Determining material contrasts with s-SNOM**. The scattered field $E_{\text{sca}} = se^{i\varphi}$ probed by the s-SNOM (amplitude $s$, phase $\varphi$) is proportional to the local field $E_{\text{tip}}$ at the tip end, $E_{\text{sca}} \propto \alpha_{\text{eff}} E_{\text{tip}} = \alpha_{\text{eff}} E_{\text{i}}$. Here the structure-induced (or polariton) field is not involved (discuss later). Figure 3.2b plots the calculated $E_{\text{sca}}$ (normalized to $E_{\text{sca}}$(Au) from an Au substrate) as a function of the real part of the sample permittivity $\epsilon_{\text{s}}$. It can be clearly seen that the s-SNOM probed field $E_{\text{sca}}$ strongly depends on $\epsilon_{\text{s}}$. A resonance is at the position of $\text{Re}(\epsilon_{\text{s}}) \approx -1$ because the substrate is resonant ($\beta \to \infty$). By increasing the imaginary part (namely absorption) of $\epsilon_{\text{s}}$, this resonance is suppressed. These calculations indicate that the optical contrasts observed in a s-SNOM image are related to the dielectric contrasts of the samples. The s-SNOM can probe local dielectric information of samples for local chemical and structural analysis with ultra-high resolution (typically 20 nm) [70, 71, 73, 74].

**Field mapping with s-SNOM**. In addition to determine the dielectric properties of the imaged sample, the s-SNOM can also be applied for imaging local field distribution in nanophotonic systems, such as modal mapping of optical antennas [60, 75, 76], real-space imaging of polarion fields [77–81] and the read-out of the superlens-restored images [24, 25, 27, 82]. In those cases, the tip-collected field $E_{\text{tip}}$ is expressed as $E_{\text{tip}} = E_{\text{i}} + E_{\text{p}}$, which contains both the incident field $E_{\text{i}}$ and the structure or polariton field $E_{\text{p}}$. Therefore, the s-SNOM signal becomes $E_{\text{sca}} \propto \alpha_{\text{eff}}(E_{\text{i}} + E_{\text{p}})$. In cases that $\alpha_{\text{eff}}$ and $E_{\text{i}}$ are constant or less varied with the position change, the s-SNOM mainly resolves the distribution of $E_{\text{p}}$ in those nanostructures as $E_{\text{sca}}(x, y) \propto \alpha_{\text{eff}}(E_{\text{i}} + E_{\text{p}}(x, y))$. This gives rise to the possibilities of field mapping in the nanostructures. In particular, when using a weak scattering s-SNOM tip like a Si tip [75] or a carbon nanotube tip [83], the s-SNOM can significantly avoid the tip-structure influences, thus allowing for well representing the actual field distribution in nanostructures.

Here the tip-sample coupling in the s-SNOM is introduced by using the point-dipole model. However, it should be pointed out that the point-dipole model is not completely accurate for quantitatively analysing the experimental data. More advanced tip-sample coupling models like a finite-dipole model [84] and a lightening-rod model [62] have been developed. However, the point-dipole model

due to its simplicity works well for understanding the s-SNOM imaging mechanism and qualitatively interpreting the experiment data.

### 3.2.2 Superlens combined with the s-SNOM

The s-SNOM probing of a superlens image can be represented by the experiment of a SiC superlens [24]. As sketched in Fig. 3.3, a mid-infrared sandwiched $SiO_2/SiC/SiO_2$ superlens is used to image the underlying Au subwavelength-sized holes. The polariton field $E_p$ supported by the superlens carries the subwavelength information of the object, which form a high-resolution image at the top $SiO_2$ surface. The s-SNOM tip scans at the same surface to probe and read out the high-resolution image for visualization.

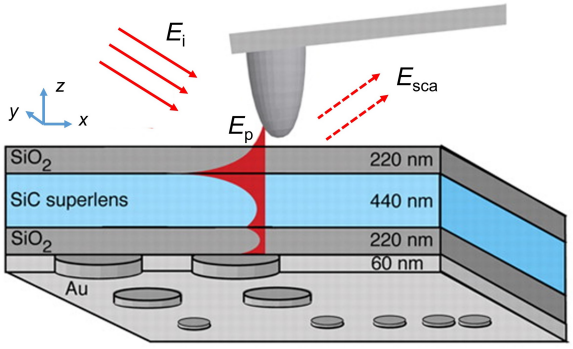


FIGURE 3.3: Sketch of the experiment of using s-SNOM to read out the image restored by a sandwich $SiO_2/SiC/SiO_2$ superlens [24]. $E_i$, the incident field. $E_{sca}$, the scattering field recorded by the s-SNOM. $E_p$, the polariton field carrying the subwavelength information of the object.

In this combination, the local field at the tip apex is not only related to the incident field but also the polariton field as $E_{tip} = E_i + E_p$. The effective polarizability $\alpha_{eff}$ is mainly attributed to the coupling between tip and the top $SiO_2$ layer, namely $\alpha_{eff} \approx \alpha_{eff}^{SiO_2}$. This is because the thickness of the dielectric $SiO_2$ layer is 220 nm, as two times as the coupling depth ($\sim$ 100 nm) in the subsurface s-SNOM [85, 86]. Therefore, the scattering field $E_{sca} = se^{i\varphi}$ recorded by the s-SNOM can be expressed as

$$E_{sca}(x, y) \propto \alpha_{eff}^{SiO_2}[E_i + E_p(x, y)] \tag{3.8}$$

This equation indicates that the image recorded by this combined system mainly relies on the polariton field $E_p$ supported by $SiO_2/SiC/SiO_2$ superlens.

It should be noted that the polariton field $E_{\mathrm{p}}$ may also be launched by the s-SNOM or the object depending on the sample configuration (e.g. a single SiC superlens without outer dielectric layers, cf. Chap. 4) as well as the matching of the in-plane wavevector (cf. Chapter 2). By considering this, the field $E_{\mathrm{p}}$ is described as the superposition of the tip-launched polariton field $E_{\mathrm{p,tip}}$ and the object launched polariton field $E_{\mathrm{p,obj}}$. The factors $\xi_{\mathrm{tip}}$ and $\xi_{\mathrm{obj}}$ are used for indicating their corresponding excitation efficiencies as $E_{\mathrm{p,tip}} = \xi_{\mathrm{tip}} E_{\mathrm{i}}$ and $E_{\mathrm{p,obj}} = \xi_{\mathrm{obj}} E_{\mathrm{i}}$. Then a more general expression can be obtained as

$$E_{\mathrm{p}} = E_{\mathrm{p,tip}} + E_{\mathrm{p,obj}} = (\xi_{\mathrm{tip}} + \xi_{\mathrm{obj}}) E_{\mathrm{i}} \tag{3.9}$$

By changing the ratio of $\xi_{\mathrm{tip}}/\xi_{\mathrm{obj}}$, different configurations of launching the polariton field can be described, see an example in Section 4.1.

The basic mechanism of the s-SNOM probing of the superlens images has been introduced above. However, a well-established theoretical model is still needed for quantitatively interpreting the s-SNOM-based superlens images. This missing step will limit the further development of this field. Hopefully, inspired by experimental results presented in this thesis, more attention from the theoretical side will be paid to this field in near future.

# 4 Dispersion mapping and dielectric-object imaging with a SiC superlens

As introduced in Section 2.2, highly confined surface polariton modes provide the enhancement of evanescent fields in the superlens. In this Chapter, I experimentally demonstrate and visualize this physical mechanism by the s-SNOM imaging of surface modes (SPhPs) in an infrared SiC superlens (Section 4.1). Furthermore, I also show the experiments that utilize the surface modes for realizing the superlens-based imaging of dielectric objects (Section 4.2).

## 4.1 Mapping phonon polaritons in SiC superlens

Surface polariton modes play the key role in the superlensing effect. However, it is difficult to image or visualize these modes. This is because these sub-diffractional modes are strongly bound at the surface of the superlens so that they cannot be imaged by conventional far-field methods. Furthermore, a low-loss superlens is required for this task, because the surface modes will be significantly damped by a large absorption loss in either the superlens or the dielectric layer. In this Section, by using the infrared s-SNOM, real-space imaging of the SPhP modes in a low loss Air-SiC-Air superlens has been achieved.

The experimental system consists of the SiC superlens and the s-SNOM as depicted in Fig. 4.1a. A 500-nm-thick SiC window (see details of the sample preparation in Appendix A) is supported by a Si substrate. The free-standing SiC layer works as a typical infrared superlens: the superlensing wavelength is at $\lambda_0 = 10.5$ $\mu$m ($\mathrm{Re}[\epsilon_{\mathrm{SiC}}] = -1$) for the Air/SiC/Air combination. This combination has smaller absorption losses compared to the previous design of the $SiO_2$/SiC/$SiO_2$ case [24], because the loss exists only in the SiC superlens and air is lossless. Furthermore,

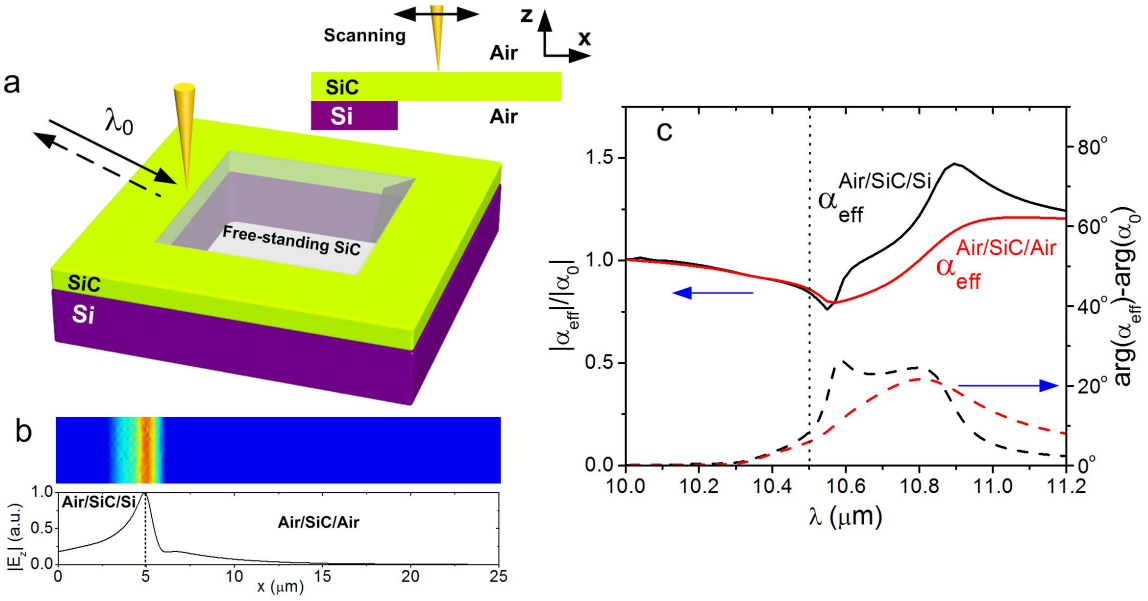


FIGURE 4.1: Nano-imaging experiment of field contrasts induced by a buried Si edge. (a) Schematic of a superlens-SNOM experiment of mapping the underlying Si edge. The top inset is the cross section of the set-up. (b) Upper panel, simulated electric field $|E_z|$ distribution at the upper surface of the SiC superlens without employing the tip. Lower panel is the line profile of $|E_z|$. (c) The effective polarizability $\alpha_{\text{eff}}$ (normalized to the polarizability $\alpha_0$ of the tip in absence of the sample) for describing the tip-sample coupling in our combined imaging system. Solid lines are the magnitude and dashed lines are phase.

the absent of dielectric ($SiO_2$) layers also makes that the s-SNOM can collect the electric fields of launched SPhP modes at the surface of the SiC superlens, which would have stronger field strength without the decay in the dielectric layer.

In this experiment, the underlying Si edge is considered as a dielectric object. The imaging resolution of the SiC superlens is determined by evaluating the optical width of the edge. At the superlensing condition, a bright line pattern corresponding to the underneath edge will be restored by the superlens at the upper Air/SiC interface, which can be seen from the prediction of the simulated field distribution ($|E_z|$, without employing the near-field tip in the simulation) as shown in Fig. 4.1b. The width of this reconstructed edge image indicates the resolution of the superlens.

A line-tunable $CO_2$-gas laser (monochromatic, ranging from 9.2 $\mu$m to 11.2 $\mu$m) is used to illuminate the sample. The high-resolution image formed by the superlens is bound at the superlens surface, which cannot be transferred in the far

field. In order to read out this image, a metallized tip of the s-SNOM is scanned to simultaneously collect the optical superlens image and the AFM topographic profiles.

In contrast to the simulated result of the isolated superlens shown in Fig. 4.1b, the metallized tip in our experiment will affect the experimental results. The backscattering field from the tip can be approximated by $E_{\mathrm{sca}} \propto \alpha_{\mathrm{eff}} E_{\mathrm{tip}}$. Here the tip field $E_{\mathrm{tip}}$ does not only involve the incident field $E_i$ but also the field $E_p$ of the launched SPhP mode in the superlens. This means that the scattered field from the tip can be further expressed by

$$E_{\mathrm{sca}}(x) \propto \alpha_{\mathrm{eff}}[E_{\mathrm{i}} + E_{\mathrm{p}}(x)] \tag{4.1}$$

Furthermore, the s-SNOM tip has a different tip-sample interaction when scanning on the SiC/Si part and on the SiC/Air part. In order to understand the coupling between the tip and the underlying layered stack, a tip-sample coupling model developed recently by B. Hauer for near-field imaging on the layered systems [87] has been used. By treating the probing tip as a dipole with an extended geometric shape in the $z$-axis, the tip-sample interaction results in an effective polarizability $\alpha_{\mathrm{eff}}$ of the coupled system as plotted in Fig. 4.1c. In the calculation of $\alpha_{\mathrm{eff}}$ shown in Fig. 4.1c, it can be seen that at the expected superlensing wavelength of 10.5 $\mu$m, the tip-sample interactions are relatively low in both the Air/SiC/Si ($|\alpha_{\mathrm{eff}}^{\mathrm{Air/SiC/Si}}| = 0.84|\alpha_0|$, $\mathrm{Arg}[\alpha_{\mathrm{eff}}^{\mathrm{Air/SiC/Si}}] - \mathrm{Arg}[\alpha_0] = 8.7^o$ ) and the Air/SiC/Air ($|\alpha_{\mathrm{eff}}^{\mathrm{Air/SiC/Air}}| = 0.85|\alpha_0|$, $\mathrm{Arg}[\alpha_{\mathrm{eff}}^{\mathrm{Air/SiC/Air}}] - \mathrm{Arg}[\alpha_0] = 6.2^o$) parts, yielding very low near-field contrasts ($\alpha_{\mathrm{eff}}^{\mathrm{Air/SiC/SiC}} \approx \alpha_{\mathrm{eff}}^{\mathrm{Air/SiC/Air}}$). $\alpha_0$ is the polarizability of the tip in absence of the sample. This result indicates that the s-SNOM tip can probe the superlensing image nearly without any obvious distortion at this specific wavelength. However, for the other wavelengths, the difference of tip polarizabilities on distinct sample areas will introduce an additional contrast to the superlens-reconstructed images.

Figure 4.2 shows the images systematically recorded with the superlens-SNOM by changing the excitation wavelengths. Since the scanning tip (Fig. 4.2a) cannot access the buried edge, the obtained AFM topography contains no information of the underlying edge while near-field optical images (Fig. 4.2b-i, both amplitude $s_3$ and phase $\varphi_3$) have succeeded in revealing this surface feature. For the case at $\lambda_0 = 9.2$ $\mu$m ($\epsilon_{\mathrm{SiC}} = 2.9$, far away from the superlensing condition) shown in

Fig. 4.2b, the edge has been seen with a wide optical width and a weak optical contrast due to the thick SiC layer.

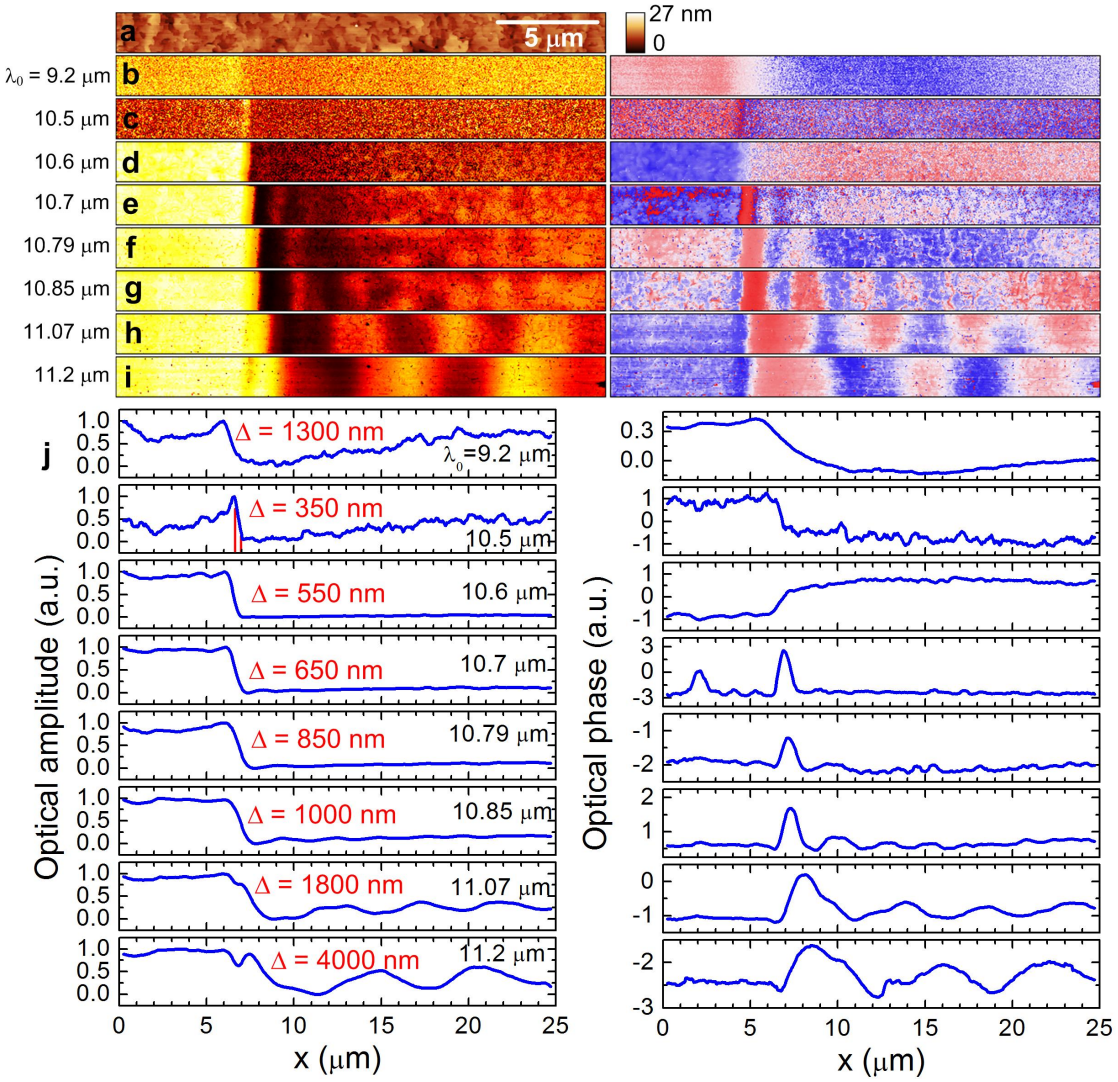


FIGURE 4.2: Infrared near-field images of the launched SPhPs in the SiC superlens. (a) Topography image taken from the upper surface of the SiC superlens. (b-i) Infrared spectral amplitude (left) and phase (right) images measured at different excitation wavelengths. (j) line profiles of the images shown in (b-i). All the amplitude data are normalized to the maximum field value in each case, respectively

By contrast, the sharpest optical feature is obtained at the superlensing wavelength of 10.5 $\mu$m, where a sharp line pattern is clearly revealed as shown in Fig. 4.2c. Strongly confined SPhPs contribute to the large enhancement of evanescent fields at the edge, enabling the reconstruction of the fields from the edge. This is in a good agreement with the numerical simulation shown in Fig. 4.1b. When the

illumination is slightly tuned to larger wavelengths, obvious optical contrasts are found between the Air/SiC/Si and Air/SiC/Air part. This is because of distinct tip-sample interactions (see Fig. 4.1c) when the tip is on the Si or on the air region. These contrasts and launched propagating SPhPs (fringes in the images) result in the distortion of actual edge information (comparison of the Fig. 4.2c and Fig. 4.2d-i).

To quantify the resolution in these images, the measured optical width (the distance from 90% to 10% of the peak value) of the edge can be extracted from the line profiles plotted in Fig. 4.2j. Consistent with our analysis, the best imaging resolution is around 350 nm at $\lambda_0 = 10.5$ $\mu$m corresponding to a resolution of about $\lambda_0/30$. For the cases away from the resonance, the edge images are distorted by the propagating SPhPs.

Another important outcome from the obtained spectroscopic results is a near-field mapping of the dispersion relation of the SPhPs in the superlens. At the wavelengths (from 10.7 $\mu$m to 11.2 $\mu$m) away from the superlensing condition, obvious optical fringes are observed in the measured optical images, which result from the interference of the launched SPhPs. Following the discussion in Section 3.2.2, these fringes are understood as a result of the interference of three SPhP terms (sketched in Fig. 4.3a): the tip-launched SPhPs ($E_{\mathrm{p1}} = \xi_{\mathrm{tip}} E_{\mathrm{i}}$, $\xi_{\mathrm{tip}}$ indicating tip-launching efficiency), tip-launched and edge-reflected SPhPs ($E_{\mathrm{p2}} = r_{\mathrm{p}} E_{\mathrm{p1}} e^{\mathrm{i}2k_{\mathrm{p}}x}$, $r_{\mathrm{p}}$ being the reflection coefficient of SPhPs at the underlying Si/Air boundary), and the edge-launched SPhPs ($E_{\mathrm{p3}} = \xi_{\mathrm{edg}} E_{\mathrm{i}} e^{\mathrm{i}(k_{\mathrm{p}} - k_0 \cos\theta)x}$, $\xi_{\mathrm{edg}}$ indicating edge-launching efficiency). The overall polariton field $E_{\mathrm{p}}$ are now expressed as

$$\begin{aligned} E_{\mathrm{p}}(x) &= E_{\mathrm{p1}} + E_{\mathrm{p2}}(x) + E_{\mathrm{p3}}(x) \\ &= \xi_{\mathrm{tip}} E_{\mathrm{i}} + r_{\mathrm{p}} \xi_{\mathrm{tip}} E_{\mathrm{i}} e^{\mathrm{i}2k_p x} + \xi_{\mathrm{edg}} E_{\mathrm{i}} e^{i(k_{\mathrm{p}} - k_0 \cos\theta)x} \\ &= E_{\mathrm{i}}[(1 + r_{\mathrm{p}} e^{i2k_{\mathrm{p}}x})\xi_{\mathrm{tip}} + \xi_{\mathrm{edg}} e^{i(k_{\mathrm{p}} - k_0 \cos\theta)x}] \end{aligned} \tag{4.2}$$

where $\theta \sim 50^{\mathrm{o}}$ is the incident angle of the illumination. Taking into the account the fact that here the tip is close to the highly reflective (negative permittivity) SiC surface and the resulting strong field enhancement inside the nanoscale gap between the tip and the SiC [88], the launching efficiency of the tip ($\xi_{\mathrm{tip}}$) is assumed to be larger than that of the edge-launched SPhPs ($\xi_{\mathrm{edg}}$), as $\xi_{\mathrm{edg}}/\xi_{\mathrm{tip}} = 0.2$. Using Equation 4.2, the calculated results of the SPhP interferences are shown in Fig. 4.3b-d. A good agreement is found between the experiment and the modelling results at three different wavelengths. This comparison allows extracting the

corresponding $k_p$ of the SPhPs from the fringes measured in the optical images, e.g., $\mathrm{Re}(k_p) = 6.1k_0$ at $\lambda_0 = 10.7$ $\mu$m, $\mathrm{Re}(k_p) = 2.9k_0$ at $\lambda_0 = 11.07$ $\mu$m and $\mathrm{Re}(k_p) = 2.2k_0$ at $\lambda_0 = 11.2$ $\mu$m.

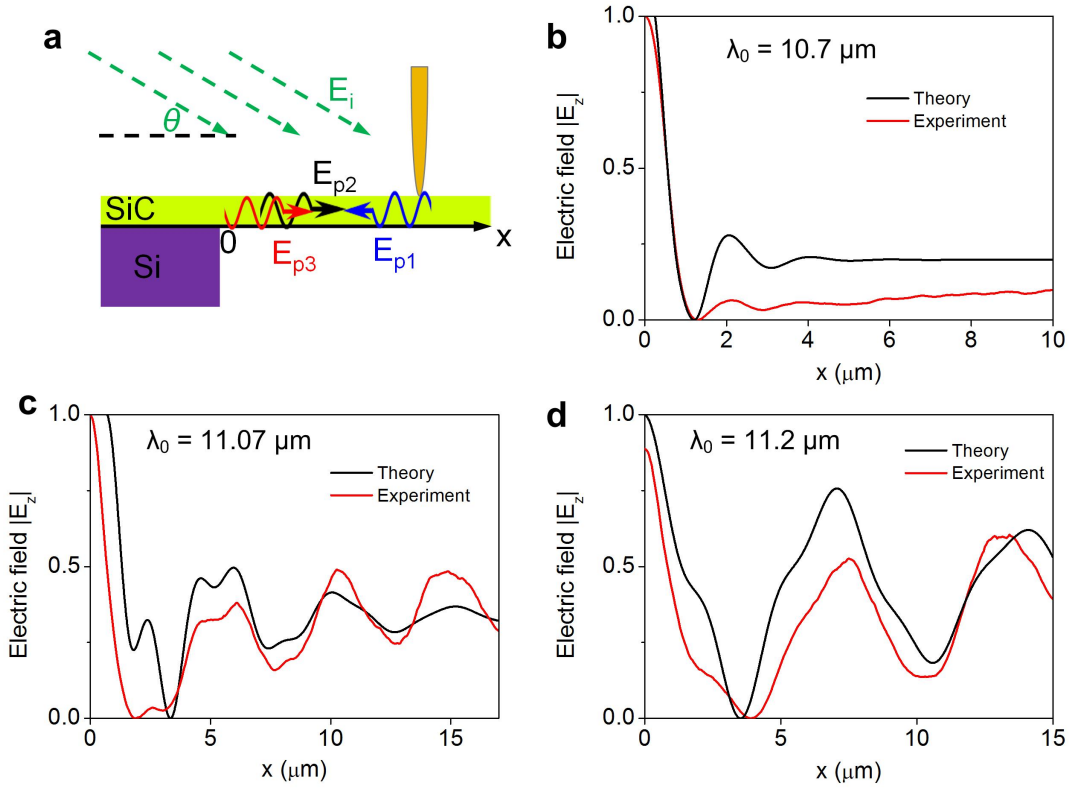


FIGURE 4.3: Determination of the polariton wavevector. (a) Schematic of the interference of tip- and edge-launched SPhPs. (b - d) Comparison of the theory and experiments at three wavelengths.

Figure 4.4 compares the extracted dispersion relation of the SPhPs with the theoretical calculations, which also shows a good agreement. These experimental and theoretical results verify the superlensing mechanism: the coupled surface waves (with much shorter $\lambda_p$) at the two superlens/dielectric interfaces enhance the evanescent information for subwavelength imaging. The presented results have provided the direct and visualized evidence for better understanding of the fundamental physics of the superlensing effect in addition to previous far-field experiments of measuring the enhancement of evanescent waves in the superlens [89, 90].

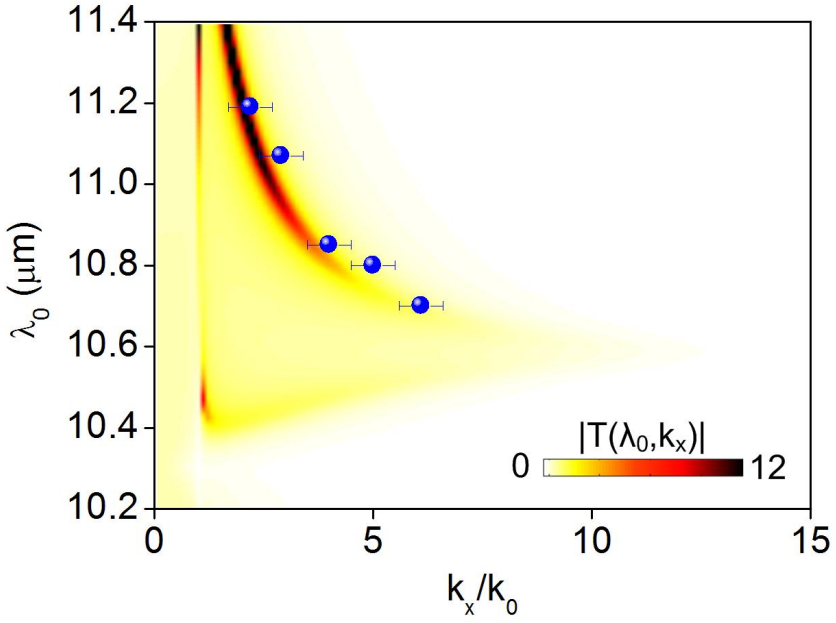


FIGURE 4.4: Comparison of the calculated superlens (Air-SiC-Air) dispersion and the measured results (blue dots). It is noted that the theoretical dispersion is red shifted about 0.1 $\mu$m to fit the experimental results. This could be due to the deviation of the used SiC dielectric function.

## 4.2 Imaging dielectric objects with the SiC superlens

### 4.2.1 Experiments and results

Section 4.1 gave the experimental demonstration and the visualized proof that the near-field superlensing effect is due to the ultra-confined surface polariton modes existing in the thin superlens (in the presented case, SPhPs for the SiC superlens). On basis of these ultra-confined polariton modes, the superlens can reconstruct the subwavelength information of the buried object on its top surface and realize the sub-diffraction-limited near-field imaging at mid-infrared frequencies, which would inspire rich infrared spectroscopic applications for chemistry, biology and material science, such as polymer characterization [68, 73], organic structure identification [91] and vibrational spectroscopy [70].

However, up to date, all other reported superlens experiments are based on investigations of metallic or strongly reflective structures [22–26, 89, 90, 92, 93]. The imaging of dielectric objects is still a challenging issue in the research field of superlens because of one obvious technological difficulty involving the low signal-to-noise ratio (the signal level detected from dielectric objects is usually lower than that from metallic ones). This missing step limits practical applications of a superlens for most of chemical and biological samples. In this Section, I will show near-field imaging experiments that use the infrared SiC superlens to image two kinds of dielectric objects: polystyrene (PS) and $SiO_2$ spheres. The obtained results verify that superlens-based spectroscopic images do not only provide the high-resolution visualization ($\lambda/18$-resolution) of the investigated dielectric objects (the PS and $SiO_2$ spheres), but also enable spectroscopic characterization and identification of the material properties of these subwavelength spheres.

The experimental system consists of a SiC superlens and the s-SNOM as depicted in Fig. 4.5a. A single free-standing (300-nm-thick) SiC layer works as a typical infrared superlens to image the underlying objects. I firstly investigate the case that PS spheres with different diameters (0.5 $\mu$m and 1 $\mu$m) are beneath the SiC superlens. Compared to previous designs of the sandwiched superlens [24–26], our single-layered configuration has removed the two outer matching-layers, which avoids additional absorption losses, thus for increasing the signal level and improving the superlens resolution. In this case (the combination of Air/SiC/Air) the superlensing wavelength of the superlens is at around $\lambda = 10.5$ $\mu$m ($\mathrm{Re}[\epsilon_{\mathrm{SiC}}] = -\epsilon_{\mathrm{Air}} = -1$). The whole sample is illuminated by an infrared line-tunable $CO_2$ laser. The s-SNOM tip is scanning across the top surface to simultaneously collect topographic profiles and the high-resolution optical image reconstructed by the superlens.

The experimental results are shown in Fig. 4.5b-e. From the topography image shown in Fig. 4.5b, it cannot observe any object information since the tip cannot access the PS spheres. Also in the control experiment (Fig. 4.5c) taken at the wavelength of 9.2 $\mu$m ($\mathrm{Re}[\epsilon_{\mathrm{SiC}}] = 2.8$, far away from the superlensing condition), no optical feature can be revealed due to the fast decay of evanescent fields through the thick SiC layer. On the contrary, when the illumination light is tuned to the superlensing wavelength range ($\mathrm{Re}[\epsilon_{\mathrm{SiC}}(\lambda)] = -1$), infrared near-field images clearly resolve the PS spheres under the SiC superlens: the best amplitude imaging obtained at $\lambda = 10.5$ $\mu$m (Fig. 4.5d) and the best phase imaging at $\lambda =$

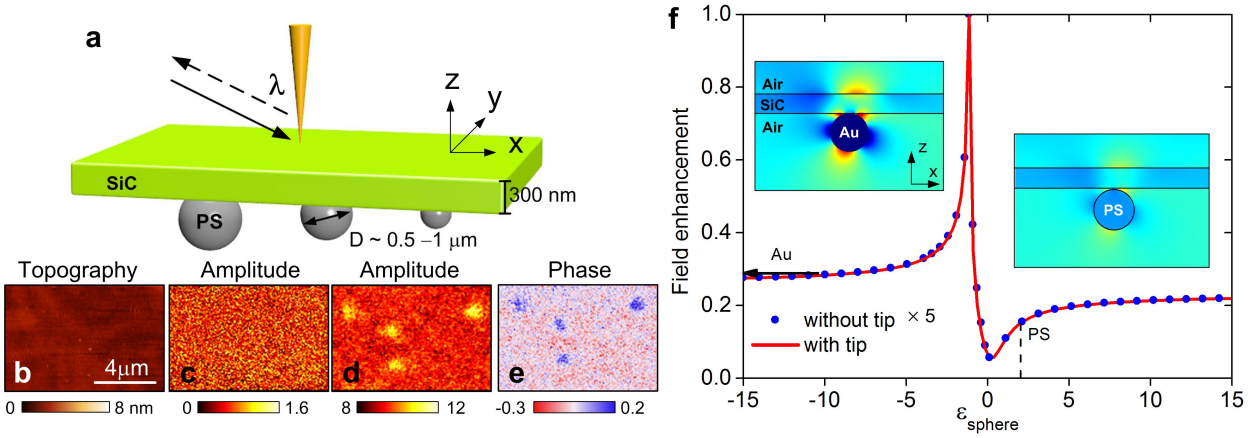


FIGURE 4.5: Nanoimaging of PS spheres below a SiC superlens. (a) Sketch of the experimental configuration. (b) The AFM topography image taken from the upper SiC surface. This image shows that buried spheres are not accessible to the tip. (c) A control experiment showing infrared amplitude $s_2$ at $\lambda = 9.2$ $\mu$m, which is out of the working wavelength range of the SiC superlens. (d) Infrared amplitude ($s_2$) image taken at the superlensing wavelength $\lambda = 10.5$ $\mu$m. (e) Infrared phase ($\varphi_2$) image measured at $\lambda = 10.68$ $\mu$m. (f) The simulated electric field ($|E_z/E_\mathrm{i}|$, taken from the top surface, above the sphere) as a function of the dielectric permittivity of the nanosphere. Red solid line is for the case with the tip. Blue dots are for the case without considering the tip (multiplied by about 5 times). Black arrow marks the field enhancement obtained from the gold case. Inserts, simulated field ($|E_z|$) distributions for the cases of a gold sphere (left) and a PS sphere (right) beneath the 300-nm-thick SiC superlens, respectively. The diameter of the spheres is set to be 600 nm.

10.68 $\mu$m (Fig. 4.5e). An optical resolution of about 580 nm [$\sim \lambda/18$] has been demonstrated.

To quantitatively compare the field strength of dielectric-object imaging with that of metallic-object imaging, as shown as color plots in the inset of Fig. 4.5f, numerical simulations are performed to investigate the cases that different spheres (with the same diameter $D = 600$ nm, but various dielectric permittivities) are under the SiC superlens. First, the simulated electric-field ($|E_z|$) distributions at $\lambda = 10.5$ $\mu$m for the two cases that a gold sphere and a PS sphere are below the superlens (without the tip), respectively. For both cases the nanosphere can be resolved by the superlens (see hot spots at the top surface of the superlens). The image field of the gold sphere is obviously (nearly two times) stronger than that of the PS case. This is because the SPhP fields excited by the gold sphere are stronger than that by low dielectric-constant PS spheres ($\epsilon_\mathrm{PS} = 2.3$).

More detailed analyses are shown as curve and dotted plots in Fig. 4.5f. In these cases the probed electric field (normalized to incident field as $|E_z/E_\mathrm{i}|$) is taken from the top surface as a function of the dielectric permittivity (lossless) of the sphere at $\lambda = 10.5$ $\mu$m. From these results, it can be seen that the electric field restored by the superlens involves with the material property of the sphere. Namely, the maximum field is obtained when the sphere ($\epsilon_\mathrm{sphere} \sim -1.2$) is resonantly coupled to the superlens. In addition, the fields induced by dielectric sphere cases ($\epsilon_\mathrm{sphere} > 0$) are lower than those in metallic sphere cases ($\epsilon_\mathrm{sphere} < 0$). For instance, the field in the gold sphere case ($|E_z/E_\mathrm{i}| \sim 0.27$) is nearly twice as large as that in the PS sphere case ($|E_z/E_\mathrm{i}| \sim 0.15$). In the same figure, I also plot the result (dotted) from the case with a metallic s-SNOM tip on top of the superlens and the sphere. The near-field tip significantly increases the electric field to about five times as large as before due to the strong enhancement of excited SPhP fields inside the nanoscale gap between the tip and the superlens [88]. Additionally, it can be also noticed that this strong tip-enhancement does not influence the superlens-sphere interaction, because the shapes of the two curves for the cases with and without the tip are coincident.

Figure. 4.6 shows the recorded spectroscopic amplitude ($s_2$ signals) and phase ($\varphi_2$ signals) images of the PS spheres. In the narrow wavelength range ($\Delta\lambda = 0.6$ $\mu$m, $\Delta\lambda/\lambda = 0.05$) the superlens achieves the high-resolution amplitude and phase imaging of the subwavelength spheres. Particularly, these superlensing images show obvious spectroscopic variations of imaging contrasts. At $\lambda = 10.5$ $\mu$m, the restored image of PS spheres shows bright amplitude contrasts ($\Delta s_\mathrm{PS} = s_{2,\mathrm{PS}}/s_{2,\mathrm{B}} > 1$, $s_{2,\mathrm{PS}}, s_{2,\mathrm{B}}$ being s-SNOM amplitude signals of PS spheres and background) and no phase contrasts ($\Delta\varphi_\mathrm{PS} = \varphi_{2,\mathrm{PS}} - \varphi_{2,\mathrm{B}} \approx 0$, $\varphi_{2,\mathrm{PS}}$, $\varphi_{2,\mathrm{B}}$ being s-SNOM phase signals of PS spheres and background, respectively). When tuning the wavelength to larger wavelengths (until $\lambda = 10.68$ $\mu$m), the amplitude contrasts of the sphere images become weaker and the phase images appear with negative contrasts ($\Delta\varphi_\mathrm{PS} < 0$). For wavelengths larger than $\lambda = 10.68$ $\mu$m, the amplitude contrasts of the spheres becomes negative (namely $\Delta s_\mathrm{PS} < 1$). Moreover, all the resolved PS spheres with different optical widths show the same spectroscopic variation, indicating that these wavelength-dependent behaviours are mainly involved with the material property of the sphere.

The experimental results shown in Fig. 4.6 already prove that the superlens is able to image dielectric objects with an ultrahigh resolution. However, only the

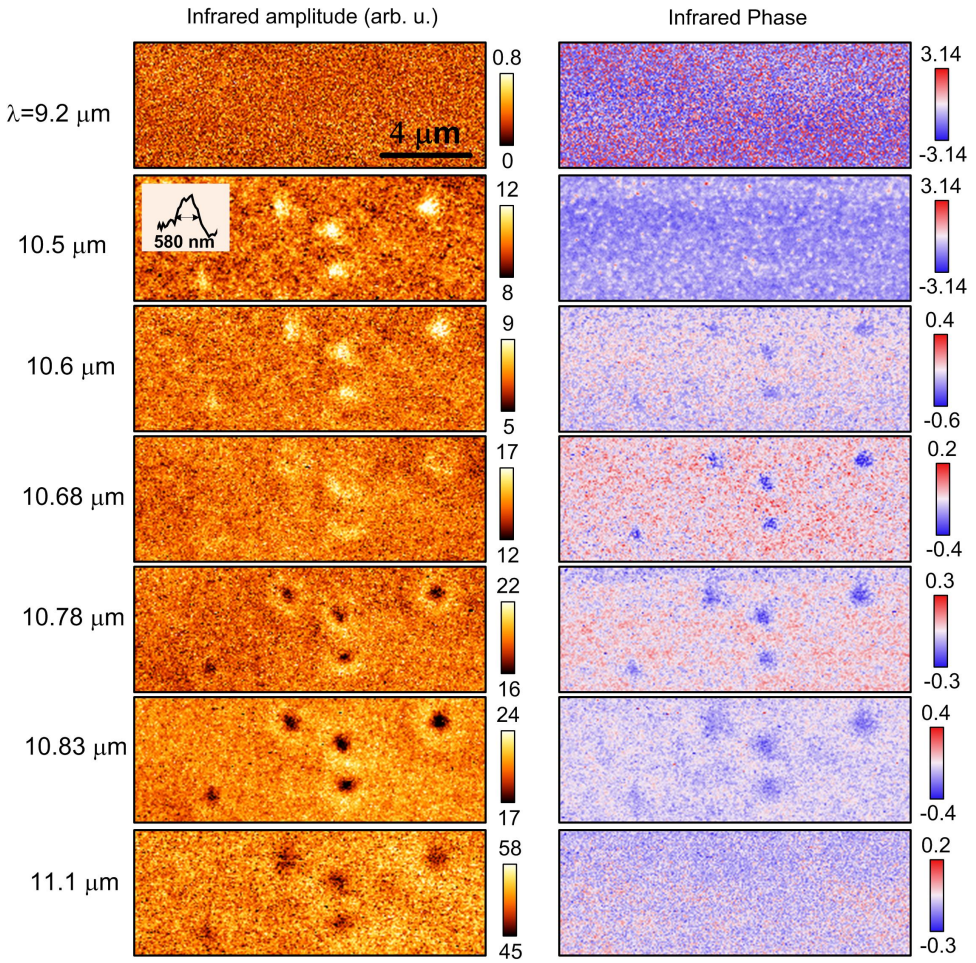


FIGURE 4.6: Infrared spectroscopic nanoimaging of PS spheres through the superlens. Infrared spectral amplitude and phase images measured at different illumination wavelengths. The imaging contrasts of PS spheres show clear spectroscopic variations. The line profile inserted in the amplitude image at the wavelength of 10.5 $\mu$m shows that the resolved optical width (FWHM) of the smallest PS sphere is about 580 nm.

case with PS spheres is explored in these experiments. What will happen if the superlens is utilized to image various kinds of dielectric spheres? To answer this question, as sketched in Fig. 4.7a, I perform experiments to image two different kinds of dielectric spheres (PS and $SiO_2$) beneath the superlens. Representative infrared near-field amplitude $s_2$ and phase $\varphi_2$ images are shown in Fig. 4.7b. It can be seen that the imaged spheres (marked by black and white arrows) are distinguished by the spectroscopic s-SNOM images: i) At $\lambda = 10.5$ $\mu$m, two spheres marked by white arrows (PS spheres, identified from later analyses) show nearly no phase contrast ($\Delta\varphi_{PS} \approx 0$) while the other ($SiO_2$) sphere marked by the black

arrow has the positive phase contrast ($\Delta\varphi_{SiO_2} > 0$). ii) The two PS spheres show the dark amplitude contrast ($\Delta s_{PS} < 1$ ) at $\lambda = 10.78$ $\mu$m. On the other hand, the amplitude contrast of the $SiO_2$ sphere is still positive ($\Delta s_{SiO_2} > 1$) at $\lambda = 10.78$ $\mu$m and becomes negative at larger wavelength of $\lambda = 10.85$ $\mu$m. Therefore, these two kinds of spheres can be distinguished at the wavelength of $\lambda = 10.78$ $\mu$m due to the opposite amplitude contrasts.

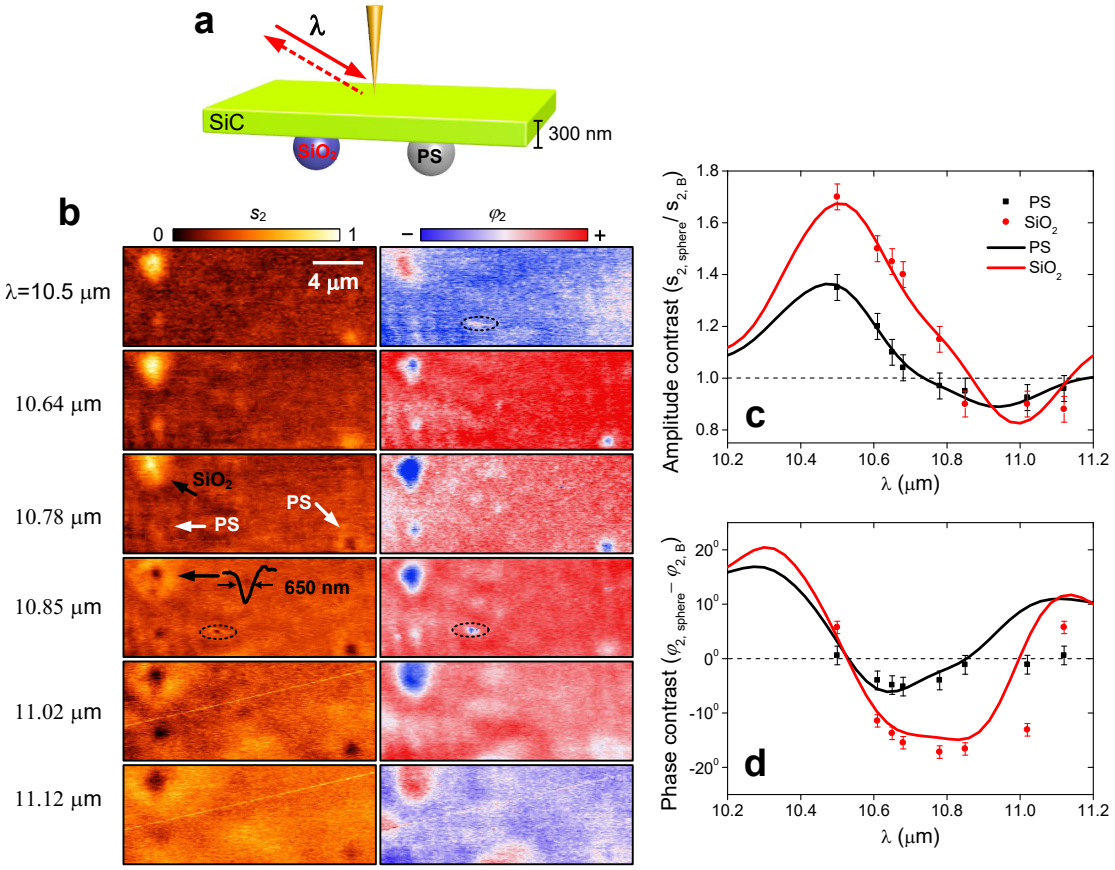


FIGURE 4.7: Spectroscopic identification of PS and $SiO_2$ spheres through the SiC superlens. (a) Sketch of the experiment. (b) Infrared amplitude $s_2$ and phase $\varphi_2$ images taken at different wavelengths. The PS and $SiO_2$ spheres can be clearly distinguished in the amplitude image taken at the wavelength of $\lambda = 10.78$ $\mu$m. The insert in the amplitude image at $\lambda = 10.85$ $\mu$m is the line plot of amplitude signals $s_2$ across the $SiO_2$ sphere, showing a 650-nm optical width. The observed ring-like field distributions are due to the SPhPs. Experimentally determined amplitude (c) and phase (d) contrasts of the PS and $SiO_2$ spheres vary with the illumination wavelength. The dots are the measured data. For comparison, simulated results for the cases of imaging different spheres are also plotted: PS (black line), $SiO_2$ (red line). The simulated curves are blue shifted about 0.1 $\mu$m for fitting the experimental data. Note that optical features marked by dashed circles are caused by mechanical artefacts (tip jumping, see the topography image in Appendix C) during scanning.

Figure 4.7c and d systematically plot the experimentally determined amplitude and phase contrasts (black dots: $\Delta s_{\mathrm{PS}}$ and $\Delta\varphi_{\mathrm{PS}}$, red dots: $\Delta s_{\mathrm{SiO_2}}$ and $\Delta\varphi_{\mathrm{SiO_2}}$) of the PS and $SiO_2$ spheres (with similar optical widths $\sim$ 650 nm) as a function of the wavelength. It can be seen that both PS and $SiO_2$ spheres show their maximum amplitude contrasts at $\lambda = 10.5\mu$m ($\Delta s_{\mathrm{PS}} \approx 1.65$, $\Delta s_{\mathrm{SiO_2}} \approx 1.3$). At larger wavelengths, the amplitude contrasts get weak and nearly vanish ($\Delta s_{\mathrm{PS}}$, $\Delta s_{\mathrm{SiO_2}} \approx 1$) at about $\lambda = 10.7$ $\mu$m for the PS sphere and at around $\lambda = 10.82$ $\mu$m for the $SiO_2$ case. Further increasing the wavelength, the darkest amplitude contrasts ($\Delta s_{\mathrm{PS}} \approx 0.9$, $\Delta s_{\mathrm{SiO_2}} \approx 0.8$) are obtained at about $\lambda = 10.9$ $\mu$m for the PS sphere and at around $\lambda = 11\mu$m for the $SiO_2$ case. Meanwhile, phase contrasts of the spheres also show material-dependent behaviors. For example, the best phase contrasts are obtained at around $\lambda = 10.64$ $\mu$m for the PS sphere ($\Delta\varphi_{\mathrm{PS}} = -5.2°$) and at $\lambda = 10.78$ $\mu$m for the $SiO_2$ sphere ($\Delta\varphi_{\mathrm{SiO_2}} \approx -17.2°$).

To further verify the experimental data, numerical simulations are carried out for the cases that PS and $SiO_2$ spheres are beneath the superlens (c.f. Appendix B), respectively. The simulations are two-dimensional cases due to a limit of our computing resources. The gold tip is modeled with an elliptical shape with the length $L = 600$ nm and the apex radius $a = 30$ nm. The tip end is at the height of 10 nm above the top surface of the SiC superlens. First, the tip is considered on the top of the underlying object and obtain the simulated z-component of electric field $E_{z,\mathrm{s}}$ from the bottom end of the tip. In a subsequent simulation, the tip position is set to be 2 $\mu$m away from the object and record the tip field $E_{z,\mathrm{o}}$. Afterwards, the normalized amplitude contrasts ($|E_{z,\mathrm{s}}|/|E_{z,\mathrm{o}}|$) and phase contrasts ($\mathrm{Arg}(E_{z,\mathrm{s}}) - \mathrm{Arg}(E_{z,\mathrm{o}})$) are obtained from those two simulations. The simulated amplitude and phase contrasts are also shown in Fig. 4.7c and d for comparison. A reasonable agreement has been found between the experimental data and the theoretical simulations. All these results confirm that the superlens does not only allow for imaging dielectric objects with high spatial resolution, but also enables further spectroscopic identification of their material properties.

### 4.2.2 Understanding and Discussions

The physics behind the results shown in last section can be understood by the distinct SPhP dispersion relations on different superlens-sample systems. I first consider the case that the s-SNOM tip is scanning at a position with air below the

superlens (namely the background areas). In this case, the tip probes the optical near fields reflected from the Air/SiC/Air system (as sketched in Fig. 4.8a). I calculate its reflection coefficient (amplitude: $|r_{\mathrm{Air/SiC/Air}}|$; phase: $\mathrm{Arg}[r_{\mathrm{Air/SiC/Air}}]$) as a function of the wavelength $\lambda$ and in-plane wavevector $k_x$. These two maps describe the complete electromagnetic response (amplitude and phase) of both propagating ($k_x < k_0$) and evanescent ($k_x > k_0$) fields on this symmetric system. It is seen that two branches of reflection peaks exist and coincide at $\lambda = 10.5$ $\mu$m, which correspond to the SPhP modes supported on the Air/SiC interfaces. These SPhPs at the resonance ($\mathrm{Re}[\epsilon_{\mathrm{SiC}}] = -1$) of $\lambda = 10.5$ $\mu$m are deeply subdiffractional (polariton wavevector $k_p \gg k_0$), leading to the high-resolution imaging of the superlens.

When the tip position is above the PS sphere, the recorded fields will be modified by the underlying PS sphere. In order to calculate the reflection coefficient of the resulting superlens-sphere system, I approximate it as a planar Air/SiC/PS case (as sketched in Fig. 4.8b). The calculated results ( $|r_{\mathrm{Air/SiC/PS}}|$ and $\mathrm{Arg}[r_{\mathrm{Air/SiC/PS}}]$) for the layered system are shown below the sketch, in which the reflection peaks of high-$k_x$ components split into two modes. The lower mode is still at around $\lambda = 10.5$ $\mu$m corresponding to the SPhPs at the Air/SiC interface. The upper one shifts to about $\lambda$ =10.78 $\mu$m to match the resonant condition ($\mathrm{Re}[\epsilon_{\mathrm{SiC}}] = -\mathrm{Re}[\epsilon_{\mathrm{PS}}]$) of the SPhPs at the PS/SiC interface. For the $SiO_2$ case shown in Fig. 4.8c (I also use the planar approximation for the reflection calculations), this upper mode further red shifts to around $\lambda = 11$ $\mu$m due to the condition of $\mathrm{Re}[\epsilon_{\mathrm{SiC}}] = -\mathrm{Re}[\epsilon_{\mathrm{SiO_2}}]$.

In principle, the s-SNOM imaging contrasts depend on the reflection contrasts of the high-$k_x$ fields: $\Delta s_{\mathrm{PS}} = |r_{\mathrm{Air/SiC/PS}}|/|r_{\mathrm{Air/SiC/Air}}|$ and $\Delta\varphi_{\mathrm{PS}} = \mathrm{Arg}(r_{\mathrm{Air/SiC/PS}}) - \mathrm{Arg}(r_{\mathrm{Air/SiC/Air}})$ for the PS sphere, $\Delta s_{\mathrm{SiO_2}} = |r_{\mathrm{Air/SiC/SiO_2}}|/|r_{\mathrm{Air/SiC/Air}}|$ and $\Delta\varphi_{\mathrm{SiO_2}} = \mathrm{Arg}(r_{\mathrm{Air/SiC/SiO_2}}) - \mathrm{Arg}(r_{\mathrm{Air/SiC/Air}})$ for the $SiO_2$ case. Therefore, the shifted SPhP dispersion influences the reflected fields that further give rise to the spectral variations of imaging contrasts in our experimental images. Figure 4.9a and b plot the reflection contrasts of the high-spatial-frequency component $k_x = 10k_0$ ($k_0$ being the free-space wavevector) for the PS and $SiO_2$ cases by using the $r_{\mathrm{Air/SiC/Air}}$ as the background. It is clear that the reflection amplitude and phase contrasts indeed show the spectral variations and reversions. This agrees with and explain our experimental results shown in Fig. 4.7c and d.

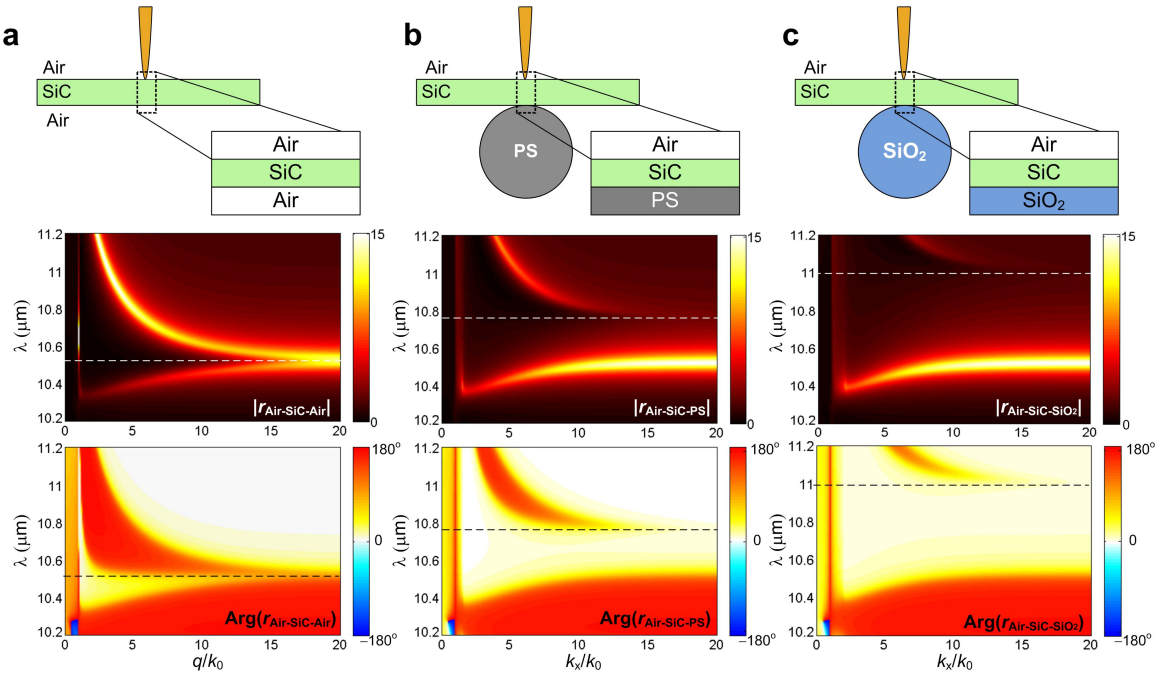


FIGURE 4.8: Understanding of the spectroscopic contrast-variation in the superlens imaging. (a) Top, sketch of that the tip on the SiC/Air area. Calculated reflection coefficient (amplitude $|r_{\mathrm{Air/SiC/Air}}|$, phase $\mathrm{Arg}(r_{\mathrm{Air/SiC/Air}})$) of the Air/SiC/Air system as a function of the wavelength $\lambda$ and in-plane wavevector $k_x$. (b) Top, sketch of the case that the tip is on the top of the PS sphere. I approximate the superlens-sphere system as the planar Air/SiC/PS case. Calculated reflection coefficient (amplitude $|r_{\mathrm{Air/SiC/PS}}|$, phase $\mathrm{Arg}(r_{\mathrm{Air/SiC/Air}})$) of the Air/SiC/PS layered system as a function of the wavelength $\lambda$ and in-plane wavevector $k_x$. (c) Top, sketch of the case that the tip is on the top of the SiO2 sphere. Calculated reflection coefficient (amplitude $|r_{\mathrm{Air/SiC/SiO_2}}|$, phase $\mathrm{Arg}(r_{\mathrm{Air/SiC/SiO_2}})$) of the approximated Air/SiC/PS system as a function of the wavelength $\lambda$ and in-plane wavevector $k_x$. In the calculations, dielectric permittivities of PS and $SiO_2$ are set as $\epsilon_{\mathrm{PS}} = 2.3$ and $\epsilon_{\mathrm{SiO_2}} = 3.7$ by neglecting the imaginary parts of their permittivities and the material dispersion for the sake of simplification.

Figure 4.9c and d further present the calculated reflection contrasts as a function of the wavelength $\lambda$ and the dielectric permittivity $\epsilon_{\mathrm{obj}}$ of the object (for $k_x = 10k_0$, for the calculations still using the assumption of treating the object-superlens as the layered system). These two figures reveal systematically the material influence of the investigated sphere on the imaging contrasts. It is clear that the reflection contrasts have a dependence on the dielectric permittivity of the investigated object. For example, when the dielectric permittivity of the object increases from $\epsilon_{\mathrm{obj}} = 1$ to $\epsilon_{\mathrm{obj}} = 5$, the transition wavelength corresponding to the reversion of the amplitude contrast (namely for $|r_{\mathrm{Air/SiC/}\epsilon_{\mathrm{obj}}}| = |r_{\mathrm{Air/SiC/Air}}|$) is shifted from $\lambda \approx$

10.55 $\mu$m to $\lambda \approx 11.2$ $\mu$m. Meanwhile, the transition wavelength corresponding to the reversion of the phase contrast (for $\mathrm{Arg}[r_{\mathrm{Air/SiC}/\epsilon_{\mathrm{obj}}}] - \mathrm{Arg}[r_{\mathrm{Air/SiC/Air}}] = 0$) is shifted from $\lambda \approx 10.6$ $\mu$m to $\lambda \approx 10.9$ $\mu$m. These dependences reveal the important fact that the spectroscopic contrasts of superlensing imaging are in principle able to reveal the dielectric property of the investigated sphere.

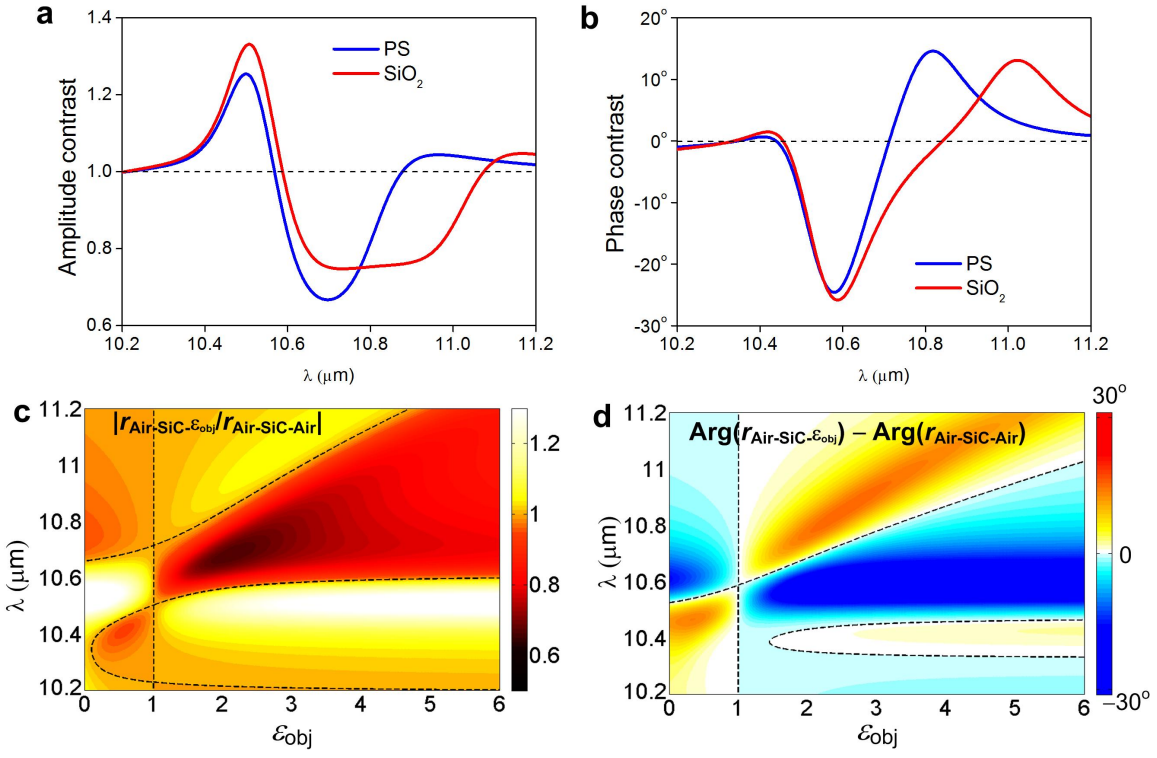


FIGURE 4.9: Wavelength-dependent reflection contrasts (for $k_x = 10k_0$) for PS and $SiO_2$ objects: (a) amplitude contrast, (b) phase contrast. (c) The reflection amplitude contrast as a function of the wavelength $\lambda$ and the dielectric permittivity $\epsilon_{\mathrm{obj}}$ of the investigated object for the component of $k_x = 10k_0$. Black dotted lines indicate the transition case that shows no amplitude contrast: $|r_{\mathrm{Air/SiC}/\epsilon_{\mathrm{obj}}}|/|r_{\mathrm{Air/SiC/Air}}| = 1$. (d) The reflection phase contrast as a function of the wavelength $\lambda$ and the dielectric permittivity $\epsilon_{\mathrm{obj}}$ of the investigated object for the component of $k_x = 10k_0$. Black dotted lines represents the case that show zero phase contrast: $\mathrm{Arg}(r_{\mathrm{Air/SiC}/\epsilon_{\mathrm{obj}}}) - \mathrm{Arg}(r_{\mathrm{Air/SiC/Air}}) = 0$.

It should be noted that all these theoretic analyses are based on the simplified approximation that treats the superlens-sphere system as the planar layers, which thus is different with the actual experimental cases. Nevertheless, they provide a qualitative picture of the sphere-modified SPhP dispersion to understand spectral variations of the imaging contrast in our superlens experiments. Moreover, for the sake of simplification, our discussions do not include the imaginary part of

the dielectric permittivity of the sphere, which contains the information of (vibrational) absorption of the imaged object. According to recent findings in near-field vibrational nanoscopy [68, 73], the absorption properties of nanoscale objects can be derived from the phase of probed near fields. Therefore, the absorption of the object can be explored in future researches by carefully analysing the phase information of the superlens-recorded images.

## 4.3 Conclusion

To summarize this Chapter, the dispersion relation of the superlens has been experimentally mapped through s-SNOM imaging of the launched SPhPs. The obtained dispersion relation clearly confirms the basic imaging mechanism of the superlens imaging: the resonant surface modes provide the enhancement of evanescent fields, enabling the reconstruction of high-spatial-frequency information of the investigated object.

Furthermore, infrared spectroscopic nanoimaging of dielectric objects (PS and $SiO_2$ sub-micron spheres) with the SiC superlens has been experimentally demonstrated. In addition to the high resolution, the obtained spectroscopic imaging results also for the first time reveal that the superlens imaging can identify the material properties of the imaged objects. Through examining the dispersion relation of the superlens, these phenomena are explained as the fact that the surface polariton modes in the superlens are sensitive to the dielectric index of the surrounding material. The presented work would open up the door to the superlens-based infrared spectroscopy for abundant imaging and sensing applications, such as subsurface imaging [85, 87, 94, 95], vibrational spectroscopy [70], material identification[68, 73] and the characterization of subsurface charge-carrier profiles in semiconducting devices [74, 96]. I expect that the results shown here are not only useful for the superlens researches, but are also instructive for other plasmonic and metamaterial imaging devices, such as the hyperlens [35] and the graphene superlens (c.f. Chapter 6).

# 5 Multiwavelength superlens with different phonon-resonant materials

## 5.1 Introduction and basic idea

As introduced before, a superlens requires to match as the superlensing condition of $\epsilon_{\mathrm{SL}}(\lambda) = -\epsilon_{\mathrm{diel}}(\lambda)$. Therefore, such a lens usually consists of a noble metal or a polar dielectric, the permittivity of which can be negative in a certain wavelength range due to the plasmon resonance (or the phonon resonance). Considering their frequency dispersions, usually only one suitable wavelength for superlensing can be found around a plasmon (phonon) resonance. From this point, designing a multiwavelength superlens requires to choose a material with multiple resonances. Although few polar crystals such as $SiO_2$ and BN may have multiple phonon resonances that could be used for superlensing, the number of such candidate materials are not enough for covering a broad infrared wavelength range.

In this Chapter[1], I propose a multilayered superlens that can work at many different wavelengths. Our idea is based on a multilayer superlensing theory, which has been discussed recently [97–99]. Since adding different polar dielectric layers can provide additional degrees of freedom for more resonances, a multiwavelength superlensing can be achieved in a single, multilayered superlens. According to that theory, a multilayer system (Fig. 5.1) consists of two different materials and can be seen as an effective anisotropic material with [97–99]

$$\epsilon_x = \epsilon_y = \left(\frac{\epsilon_1^{-1} d_1 + \epsilon_2^{-1} d_2}{d_1 + d_2}\right)^{-1}, \quad \epsilon_z = \frac{\epsilon_1 d_1 + \epsilon_2 d_2}{d_1 + d_2} \tag{5.1}$$

where $\epsilon_i$, $d_i$,(i = 1,2) are the corresponding permittivities and layer thicknesses. The superlensing effect can be also found in the condition of $\epsilon_1 = -\epsilon_2$ (for the

[1]Content of this Chapter involved in the publication [P1], Page 135

case of $d_1 = d_2$). Different from a simple sandwich superlens [10, 24, 25], this condition can be fulfilled in two cases (Fig. 5.1): (1) $\epsilon_1 > 0$, $\epsilon_2 < 0$ and (2) $\epsilon_1 < 0$, $\epsilon_2 > 0$. In most of multilayer superlensing designs, permittivities of investigated materials will not change sign in the wavelength range of interest, meaning that only one matching wavelength can be obtained [97–99]. In fact, the sign of permittivities in many real materials will be changed in distinct wavelength ranges. Polar dielectrics, such as SiC, indium phosphide (InP), indium antimonide (InSb) and so on, would be typical examples.

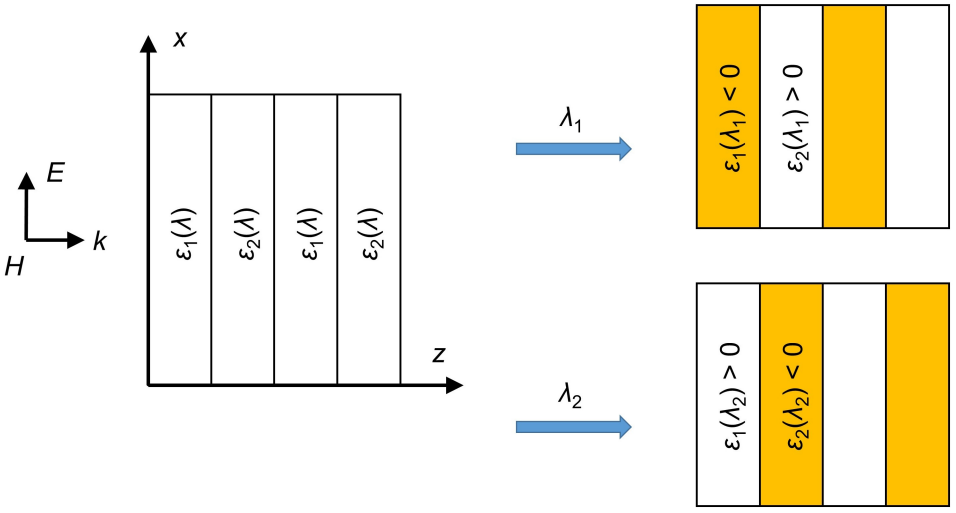


FIGURE 5.1: Schematic diagram of a multiwavelength superlens with two different polar dielectrics. Depending on the illumination wavelength, the permittivity of the used polar dielectric changes its sign.

As shown in Fig. 5.2, their dielectric permittivities (obtained using oscillator models from [100]) are negative in their reststrahlen band between the transverse and longitudinal optical-phonon frequencies, which allows for supporting SPhPs (c.f. Section 2.1.3). When the wavelength is out of the reststrahlen band, their permittivities become positive, and thus the material just acts as a 'dielectric spacer'. Exploiting different phonon resonances of multiple polar dielectrics can provide a way to achieve superlensing simultaneously at multiple wavelengths. It is clearly seen in Fig. 5.2 that the conditions for a SiC-InSb system are matched at two distinct wavelengths: $\mathrm{Re}[\epsilon_{\mathrm{InSb}}] = -\mathrm{Re}[\epsilon_{\mathrm{SiC}}] = 15.6$ at $\lambda_1 = 11.7$ $\mu$m, and $\mathrm{Re}[\epsilon_{\mathrm{InSb}}] = -\mathrm{Re}[\epsilon_{\mathrm{SiC}}] = -9.9$ at $\lambda_2 = 53.7$ $\mu$m. Moreover, it is also mentioned that the respective absorption of the two materials is small at the matching wavelengths

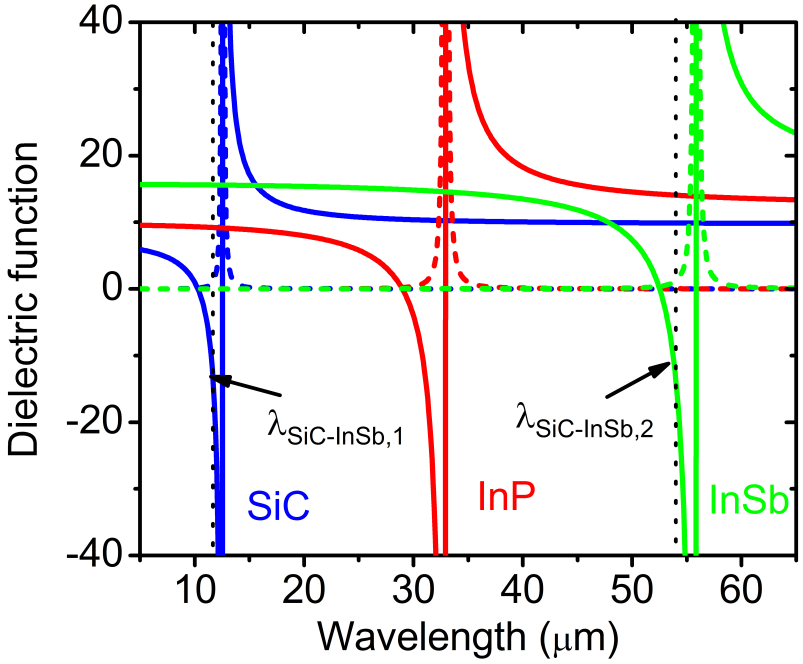


FIGURE 5.2: Real parts (solid lines) and imaginary parts (dashed lines) of dielectric permittivities of SiC, InP and InSb. Black dotted lines indicate the matched wavelengths of SiC-InSb system

($\mathrm{Im}[\epsilon_{\mathrm{InSb}}] \approx 0.1$, $\mathrm{Im}[\epsilon_{\mathrm{SiC}}] \approx 0.5$ at $\lambda_1$ and $\mathrm{Im}[\epsilon_{\mathrm{InSb}}] \approx 0.8$, $\mathrm{Im}[\epsilon_{\mathrm{SiC}}] \approx 0.1$ at $\lambda_2$]), which will significantly improve the resolution of our superlens. Thanks to the abundance of polar dielectrics, required wavelengths can be obtained with different composites: for examples, ($\lambda_1 = 11.7$ $\mu$m, $\lambda_2 = 30.3$ $\mu$m) for SiC-InP case, and ($\lambda_1 = 30.3$ $\mu$m, $\lambda_2 = 50.3$ $\mu$m) for InP-InSb lens. Based on these very promising dispersion properties, I will present detailed results of this multiwavelength sub-diffraction imaging system below.

## 5.2 Results of InSb-SiC superlens

To confirm the multiwavelength superlensing effect, I first perform numerical simulations using commercial finite-element software COMSOL. Our simulated structure is a simple four-layered structure composed of alternately InSb and SiC with a thickness of $d = 200$ nm for each layer. I assume that a Au layer of 60 nm thickness is deposited on the object side of the lens, and a double slit of 500 nm

width with 1 $\mu$m center-center separation is cut through the Au film. In all the simulated cases the structure is excited by a uniform plane wave impinging from the top of the figure. Figure 5.3 (top plots) shows the simulated distribution of

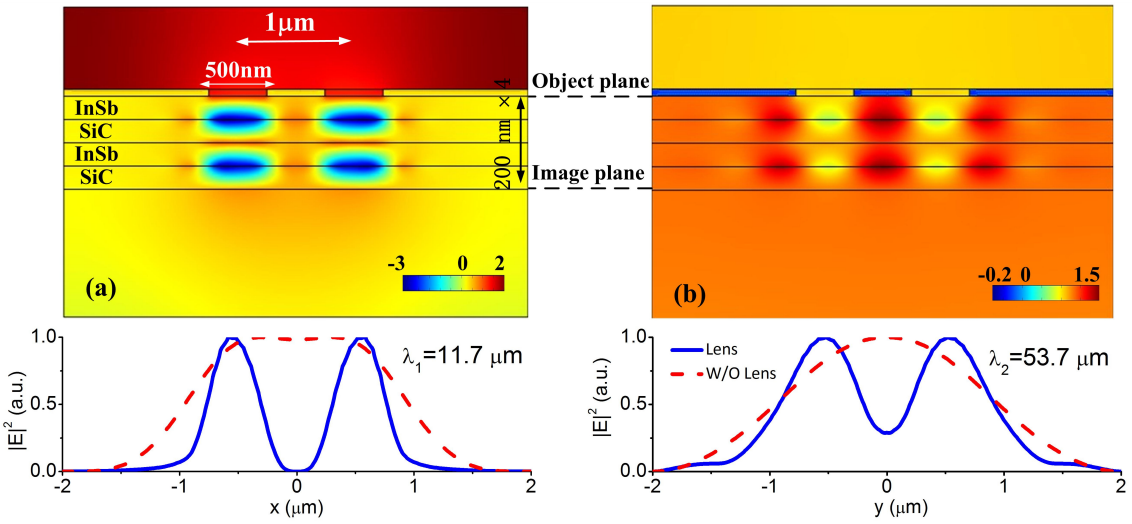


FIGURE 5.3: (Top) simulated distribution of magnetic fields for the SiC-InSb lens at two different operation wavelengths (a) $\lambda_1 = 11.7$ $\mu$m and (b) $\lambda_2 = 53.7$ $\mu$m. (Bottom) simulated electric field intensity through a 500 nm width double slit with 1 $\mu$m separation at the image plane behind the lens: blue solid line, with the superlens; red dashed line, without the superlens.

magnetic field $H$ for the designed structure at two different superlensing wavelengths: (a) $\lambda_1 = 11.7$ $\mu$m and (b) $\lambda_2 = 53.7$ $\mu$m. Strong field enhancement can be found at the InSb-SiC interface at both wavelengths, indicating the enhancement of evanescent waves. The simulated electric-field intensity at the image plane is also illustrated in Fig. 5.3 (bottom). For the case without our lens, only a single intensity peak is obtained, which means that two slits are not resolved (red dashed lines) because of the diffraction limit. However, when our lens is applied (blue solid lines), two peaks for the double slit with 1 $\mu$m separation are observed at both wavelengths. These results definitely confirm the multiwavelength superlensing effect of our lens and suggest that at least $\lambda/10$ resolution at $\lambda_1 = 11.7$ $\mu$m and $\lambda/50$ resolution at $\lambda_2 = 53.7$ $\mu$m are obtained. I also note that two peaks are not so well resolved at $\lambda = 53.7$ $\mu$m, although the performance of our lens is already good enough considering the fact that the double slit here is a deep subwavelength structure compared with the operation wavelength. One major reason is that at this wavelength, the permittivity of InSb is negative so that a large reflection at

the object plane (air-InSb interface) affects the performance of our lens [97]. In order to overcome this problem, by inserting an additional thin layer with positive permittivity material (for an example, a Si layer of 50 nm thickness) between the object and our lens, two peaks can be also well resolved.

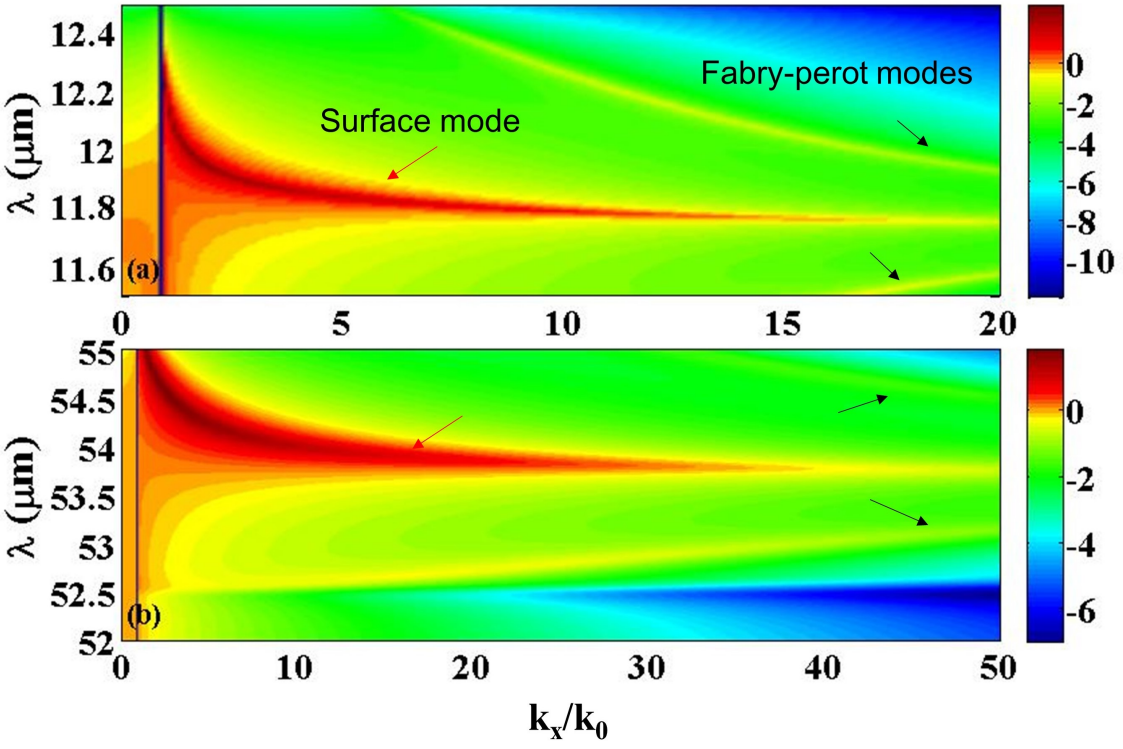


FIGURE 5.4: Variation of the transmittance ($\log_{10}[|T|^2]$) of the SiC-InSb superlens as a function of $k_x$ and the wavelength $\lambda$. Two pronounced surface modes allowing for superlensing are found at (a) 11.7 $\mu$m and (b) 53.7 $\mu$m. Additional Fabry-perot modes resulted from two negative-permittivity layers are also found. However, they cannot provide an uniform enhancement for all different spatial-frequency components.

The imaging ability and bandwidth performance of a superlens can be evaluated by its transfer function, which is the transmittance $|T|^2$ through the lens as a function of wave vector $k_x$ and the wavelength. In Fig. 5.4, I calculate the transmittance of our four-layered structure using a transfer matrix method in two different ranges near the superlensing wavelengths. For a perfect lens, $|T|^2 = 1$ is for all $k_x$ and thus a perfect image can be produced. However, in free space the transmittance decays exponentially for evanescent waves ($k_x/k_0 > 1$). Compared with that case, it can be seen that the transmittance of our four-layered superlens decays slowly at both superlensing wavelengths. It still maintains unity up to $k_x = 15k_0$ for $\lambda_1$

$= 11.7$ $\mu$m and $k_x = 36k_0$ for $\lambda_2 = 53.7$ $\mu$m. Here the lens works better at $\lambda = 53.7$ $\mu$m because it is much thinner compared with the wavelength. These good performances confirm that our lens at both operation wavelengths can enhance evanescent waves carrying subwavelength information, which is very crucial for our proposed multiwavelength superlensing. The bandwidth of our lens is also seen in Fig. 5.4. For $k_x = 10k_0$, it is about 0.13 $\mu$m when $\epsilon_{\text{SiC}} < 0$ and 0.7 $\mu$m when $\epsilon_{\text{InSb}} < 0$. Although the bandwidth of each superlensing mode is still narrow, the total working wavelength range is successfully broadened due to the additional superlensing wavelength in a single superlens.

I also showed intrinsic bandwidths of our lens under the condition that the SiC layer and InSb layer have the same thickness. In fact, from Equation 5.1, I know that superlensing wavelengths of our lens can be also tuned by changing the thickness ratio $f$ (defined as $d_1/(d_1 + d_2)$) of those two different layers. As examples

| Material | Covered Range ($\mu$m) | |
|---|---|---|
| SiC-InSb | 11 - 12.3 | 53 - 55 |
| SiC-InP | 11 - 12.3 | 30 - 32 |
| InP-InSb | 30 - 23 | 53 - 55 |

TABLE 5.1: Table 1. Covered range by changing the ratio $f$ from 0.2 to 0.8

shown in Table 5.1, when $f$ is changing from 0.2 to 0.8 (considering the fabrication feasibility), I can cover two relatively large ranges: $11 - 12.3$ $\mu$m and $53 - 55$ $\mu$m for SiC-InSb case, $11 - 12.3$ $\mu$m and $30 - 32$ $\mu$m for SiC-InP case, and $30 - 32$ $\mu$m and $53 - 55$ $\mu$m for InP-InSb case. From these figures, I obtain a practical guide for future superlens designs: 1) choosing a suitable material system to determine general positions of superlensing wavelengths; 2) fine tuning of the superlensing wavelengths with different thickness filling ratios.

## 5.3 Multiple-material configurations

Last section showed a way to a double-wavelength superlens based on the design of alternating InSb-SiC layers. An extension to a larger number of different layers, in order to achieve superlensing simultaneously at a larger number of wavelengths,

is feasible following a similar design. I rewrite Equation 5.1 to a more general form,

$$\epsilon_x = \epsilon_y = \sum_i (\frac{\epsilon_i^{-1} d_i}{D})^{-1}, \quad \epsilon_z = \sum_i \frac{\epsilon_i d_i}{D} \tag{5.2}$$

where the index $i$ corresponds to different materials, $D$ is the total thickness of the structure. The superlensing condition for a large number of different layers requires matched permittivies (for $1/\epsilon_x = 0$). According to this condition, the number of superlensing wavelengths can be controlled by simply increasing the number of phonon resonances in our system. For an example, Let us consider a case comprising three different phonon resonant dielectrics: InSb, InP and SiC. As is shown in Fig. 5.5, matching conditions of dielectric permittivities for the case that each layer has the same thickness are fulfilled at three different wavelengths (with low material absorption): $\lambda_1 = 11.2$ $\mu$m, $\lambda_2 = 30.4$ $\mu$m and $\lambda_3 = 53.3$ $\mu$m. By changing thickness ratios, this lens can also cover three ranges: $11 - 12.3$ $\mu$m, $30 - 32$ $\mu$m and $53 - 55$ $\mu$m. Thus, just a single lens can work in multiple

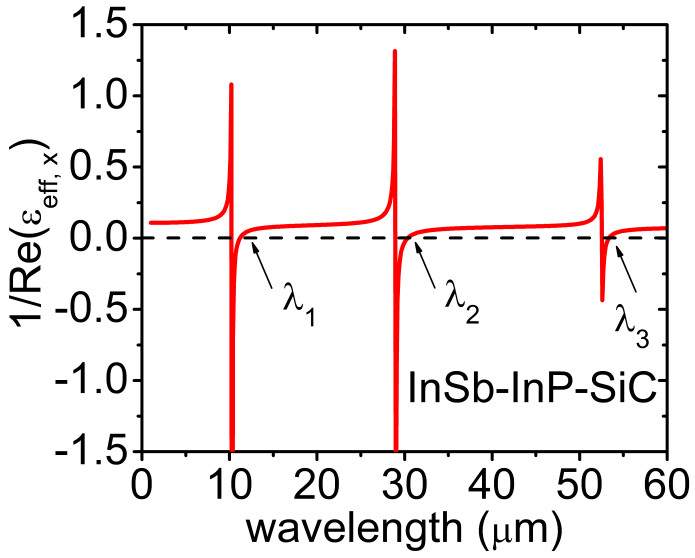


FIGURE 5.5: $1/\mathrm{Re}(\epsilon_{eff,x})$ of the InSb-InP-SiC system. The three arrows indicate the multilayered superlensing conditions

different wavelength ranges, which is an obvious advantage over other superlenses. I show the imaging ability of a six-layered (each layer thickness, 125 nm) InSb-InP-SiC superlens with a total thickness 800 nm (include a 50 nm thickness Si layer) in Fig. 5.6. The investigated object is the same double slit shown in Fig. 5.3. As expected, the two peaks of the double slit are well resolved with our lens

for three cases, which suggests that at least $\lambda/10$, $\lambda/30$ and $\lambda/50$ resolutions at each wavelength are obtained with the lens.

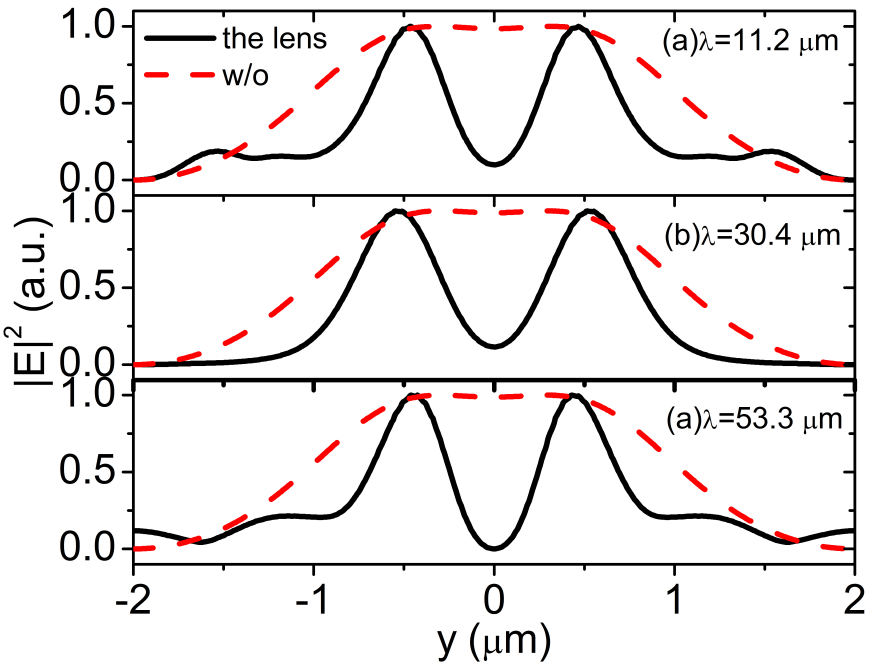


FIGURE 5.6: Distribution of the total electric field intensity for a 6-layered InSb-InP-SiC lens at three different wavelengths: (a) $\lambda = 11.2$ $\mu$m, (b) $\lambda = 30.4$ $\mu$m and (c) $\lambda = 53.3$ $\mu$m.

As mentioned before, previous reported superlenses can resolve only "one point" of the samples spectroscopic information due to their narrow bandwidths. The multiwavelength lens provides a promising way to perform the superlens-based spectroscopy. A possible application sample is the subsurface mapping of free-carrier concentrations of doped semiconductors. Different doping concentrations in doped semiconductors will lead to a large shift of the free-carrier plasma-resonance [74, 96], which requires that our superlens can cover a wide wavelength range from mid-infrared to THz. As shown in Fig. 5.7, using the same finite-dipole model as in [74], I calculate the infrared s-SNOM amplitude of n-doped InAs [100] for three different doping concentrations. The gray bars correspond to three covered ranges (bandwidths and tuning ranges) of the InSb-InP-SiC superlens. It can be seen that our lens can cover the resonances of three different cases with low, middle and high doping concentrations. For each doped InAs sample,

our proposed multiwavelength lens also has "three points" to record its spectral information. Especially for the case with doping concentration $n = 1.2\times10^{18}$ cm$^{-3}$, an almost complete spectroscopy including the information from the resonance, lower and upper branches of the $s_2$ curve, can be obtained together by using a single multiwavelength superlens. Based on this information, the proposed lens could be useful for identifying doped semiconductors and characterizing their free-carrier concentrations.

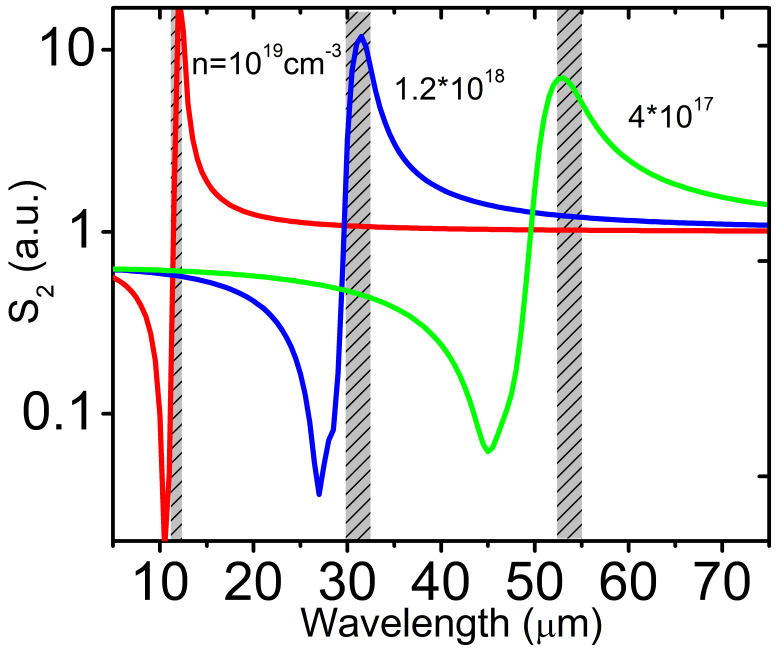


FIGURE 5.7: Infrared s-SNOM amplitude $s_2$ of $n$-doped InAs for three different doping concentrations. Gray bars correspond to three covered ranges of the InSb-InP-SiC superlens.

## 5.4 Conclusion

In conclusion, an idea of subwavelength imaging at multiple different wavelengths by a single superlens has been proposed and numerically demonstrated. The proposed scheme is based on the fact that additional degrees of freedom for superlensing at multiple wavelengths can be provided by increasing the number of phonon

resonant dielectrics in a multilayer system. In other words, a subwavelength image can be achieved at many different wavelengths by only one single lens, which is a large advantage over other recently proposed techniques for superlensing [25, 26]. Considering the abundance of polar dielectrics, our lens can cover a wavelength range from infrared to THz by choosing suitable materials [53]. Applying our multiwavelength lens to the spectroscopy of doped semiconductors, I present an example of how a novel superlens-based spectroscopy for mapping free-carrier concentrates of doped semiconductors could be realized. Based on these good performances of our lens, future applications at both infrared and THz frequencies simultaneously may be also envisioned in other fields, such as organic structure identification [91] and vibrational spectroscopy [70]. Moreover, I also note that our idea is not only restricted to superlensing, but should be also useful for other multilayer-based metamaterial concepts, especially for a hyperlens [35] and for negative refraction [36] at multiple wavelengths.

# 6 Tunable graphene lens for infrared broadband imaging

The superlensing effect relies on surface polariton modes that are sensitive to dielectric permittivities of both the superlens and the host media. Due to the dispersion relation of surface polariton modes, the superlens can only work at (or close to) the superlensing wavelength $\lambda$ fulfilling the matching condition of $\epsilon_{\mathrm{SL}}(\lambda) = -\epsilon_{\mathrm{diel}}(\lambda)$. Actually, the working bandwidth of the superlens is narrow, which is hard to be used for spectroscopic applications. The idea of the multi-wavlength superlens I proposed in Chapter 5 could broaden the working wavelength range of the superlens.

Another idea to extend the working wavelength range of the superlens is a wavelength-tunable superlens. Looking back to the superlensing condition, if the dielectric permittivity of the superlens can be controlled by one external quantity $A$, i.e., $\epsilon_{\mathrm{SL}}(\lambda, A) = -\epsilon_{\mathrm{h}}(\lambda)$, the superlensing wavelength can be tuned by varying the $A$ to cover a broader wavelength range. However, the dielectric permittivities of polar crystals and noble metals are hard to be tuned. New tunable plasmonic materials [101, 102], such as doped semiconductors [103] and graphene [104, 105], are promising candidates for this approach.

Recently, graphene with the electric-gate tuning possibility has been demonstrated to be a good tunable plasmonic material [78, 106]. In this context, I will introduce a new concept of a tunable graphene lens in Chapter 6[1]. In contrast to the SiC superlens, the non-resonant operation of the graphene lens provides the advantages of a broad intrinsic bandwidth and a low sensitivity to losses, while still maintaining a good subwavelength resolution of better than $\lambda/10$ [107]. Most importantly, thanks to the large tunability of the graphene, the graphene lens is a continuously frequency-tunable subwavelength-imaging device in a broad infrared wavelength

[1] Content of this Chapter involved in the publication [P2, P3], see Page 135

region, thus allowing for ultrabroadband spectral applications. I also experimentally demonstrate that a monolayer-graphene lens offers a 7-fold enhancement of evanescent information, improving conventional infrared near-field microscopy to resolve buried structures at a 500-nm depth with $\lambda/11$-resolution.

## 6.1 Introduction of graphene plasmons

The novel material−graphene is a monolayer of carbon atoms arranged in a two-dimensional honeycomb lattice, which has led to abundant applications in different fields [104, 105]. Recent theories and experiments have shown that a monolayer doped graphene is the thinnest (the thickness $d \sim 0.3$ nm ) plasmonic material with combined advantages of high field confinement, low intrinsic loss, high tunability and compact size [78, 79, 82, 106, 108–116]. Therefore, lots of conventional plasmonic concepts have be directly transferred to the emerging field of graphene plasmonics such as transformation optics [110], cloaking [111], and perfect absorption [112].

Different from the metal-based plasmonics, the plasmonic properties of one-atomic graphene cannot be simply described by the semi-infinite interface model. A semi-classic model depending on the surface conductivity $\sigma_{\mathrm{g}}$ of graphene has been used to fully explain the graphene plasmonic effects [110]. The graphene conductivity $\sigma_{\mathrm{g}}$ contains the intraband contribution $\sigma_{\mathrm{intra}}$ and the interband term $\sigma_{\mathrm{inter}}$, which can be evaluated as [111, 115],

$$\sigma_{\mathrm{g}}(\omega) = \sigma_{\mathrm{intra}}(\omega) + \sigma_{\mathrm{inter}}(\omega), \tag{6.1}$$

where

$$\sigma_{\mathrm{intra}}(\omega) = i\frac{e^2 k_{\mathrm{B}} T}{\pi\hbar^2(\omega + i\tau^{-1})}[\frac{\mu_c}{k_{\mathrm{B}}T} + 2\ln(\exp(-\frac{\mu_c}{k_{\mathrm{B}}T}) + 1)] \tag{6.2}$$

and

$$\sigma_{\mathrm{inter}}(\omega) = i\frac{e^2}{4\pi\hbar}\ln[\frac{2|\mu_c| - \hbar(\omega + i\tau^{-1})}{2|\mu_c| + \hbar(\omega + i\tau^{-1})}], \tag{6.3}$$

$\mu_c$ is the chemical potential in graphene, $e$ is the electron charge, $\hbar$ is the reduced Planck's constant, T is the temperature (set to be room temperature in this whole Chapter) and $\tau$ is the relaxation time of the carrier intraband scattering. For highly doped graphene $|\mu_c| \gg k_{\mathrm{B}}T$, the intraband term of graphene conductivity

can be further reduced to Drude model response like

$$\sigma_{\text{intra}}(\omega) = \frac{e^2\mu_c}{\pi\hbar^2}\frac{i}{(\omega + i\tau^{-1})}. \tag{6.4}$$

The interband terms dominate in the near-infrared and visible region, which introduce the well-known optical absorption of 2.3% [108]. In mid-infrared and THz frequency range, the Drude-like intraband contributions of doped graphene are more dominating, resulting in the novel plasmonic properties.

By treating the doped graphene as an infinitely thin conductive interface (because of $d \gg \lambda$), the dispersion relation of graphene SPPs under TM polarization can be described by[116]

$$\frac{\epsilon_1}{\sqrt{k_p^2 - \epsilon_1 k_0^2}} + \frac{\epsilon_2}{\sqrt{k_p^2 - \epsilon_2 k_0^2}} + \frac{i\sigma_g}{\omega} = 0, \tag{6.5}$$

where $k_0 = \omega/c$, $\epsilon_1$ is the permittivity of the superstrate material and $\epsilon_2$ is the permittivity of the substrate. $k_p$ is the polariton wavevector of the graphene SPPs. For the symmetric configuration ($\epsilon_1 = \epsilon_2 = 1$), the dispersion relation is given by

$$k_p = k_0\sqrt{1 - (\frac{2}{\sigma_g\eta_0})^2}, \tag{6.6}$$

where $\eta_0 = \sqrt{\mu_0/\epsilon_0} \approx 377\ \Omega$ is the wave impedance in free space.

When considering the finite layer thickness of the monolayer graphene $d$, an effective dielectric function of the graphene can be expressed as $\epsilon_g = \epsilon_0 + i\sigma/(\omega d)$. In this case, the dispersion relation of the SPPs on a highly doped graphene is described as [78, 116]

$$k_p \approx \frac{\pi\hbar^2}{e^2\mu_c}\epsilon_0(\epsilon_r + 1)\omega(\omega + i/\tau), \tag{6.7}$$

where $\epsilon_r$ is the permittivity of the substrate. Clearly, the polariton wavevector can be tuned by controlling the chemical potential of the graphene.

Recently, real-space imaging of the electric-tuned graphene SPPs has been reported independently by two groups [78, 79]. Both of them use a sharp s-SNOM tip to launch and image the graphene SPPs. They have succeeded in imaging the graphene SPPs with the polariton wavevector about $k_p \sim 40k_0$, corresponding

to $\lambda_p \sim 200$ nm. More importantly, they also demonstrated that these highly confined SPPs can be controlled by changing the electric-gate voltage applied on the graphene. Inspired by these two works, I propose to use the ultra-short and electriclly tunable graphene SPPs for realizing a new subwavelength imaging device, a electric-tunable graphene lens (GL).

## 6.2 Theory of tunable graphene lens

### 6.2.1 Evanescent-field enhancment in a graphene lens

In this section I will present the theory for the GL. The key process in the GL concept is the non-resonant enhancement of evanescent waves. In order to show this important effect, I start with a two-layer GL as illustrated in Fig. 6.1a, where two graphene sheets (GSs) are embedded in a host dielectric medium with a permittivity of $\epsilon_{\mathrm{h}} = 3$. The total thickness of the GL is $h = 800$ nm. I suppose that each graphene layer has the same complex conductivity $\sigma_g(\omega) = \sigma_1(\omega) + i\sigma_2(\omega)$, which relates with angular frequency $\omega$, operation temperature $T$, chemical potential $\mu_c$, and relaxation time $\tau$ as shown in Eq. 6.1-6.3.

Figure 6.1b plots the calculated $|T(f, k_x)|^2$ of the two-layer GL as a function of the frequency $f$ and the in-plane wavevector $k_x$ by treating the graphene layers as ideal conducting sheets with surface conductivity $\sigma_g$. The chemical potential is chosen as $\mu_c = 1.5$ eV. The relaxation time is set as $\tau = 0.5$ ps. For comparison, Fig. 6.1c also shows the result of a $SiO_2$-SiC-$SiO_2$ superlens with the same total thickness of 800 nm. Very different dispersive properties are found in these two cases. In the superlens case, two transmission modes approach and merge at the frequency possessing extraordinary transmission of evanescent waves. In contrast, for the GL two transmission modes (A and B in Fig. 6.1b) are also exited, but do not combine at a particular frequency because of geometric symmetry breaking (i.e. GSs non-symmetrically inserted into the dielectric layer, discussed in Fig. 6.3). Consistent with the findings in [98], these two modes have different physical origins. The first peak A corresponds to the surface mode located on each graphene sheet. And the peak B results from Fabry Perot resonances standing waves between graphene layers, which can be controlled by the number of graphene layers as shown in Fig. 6.2 and 6.3.

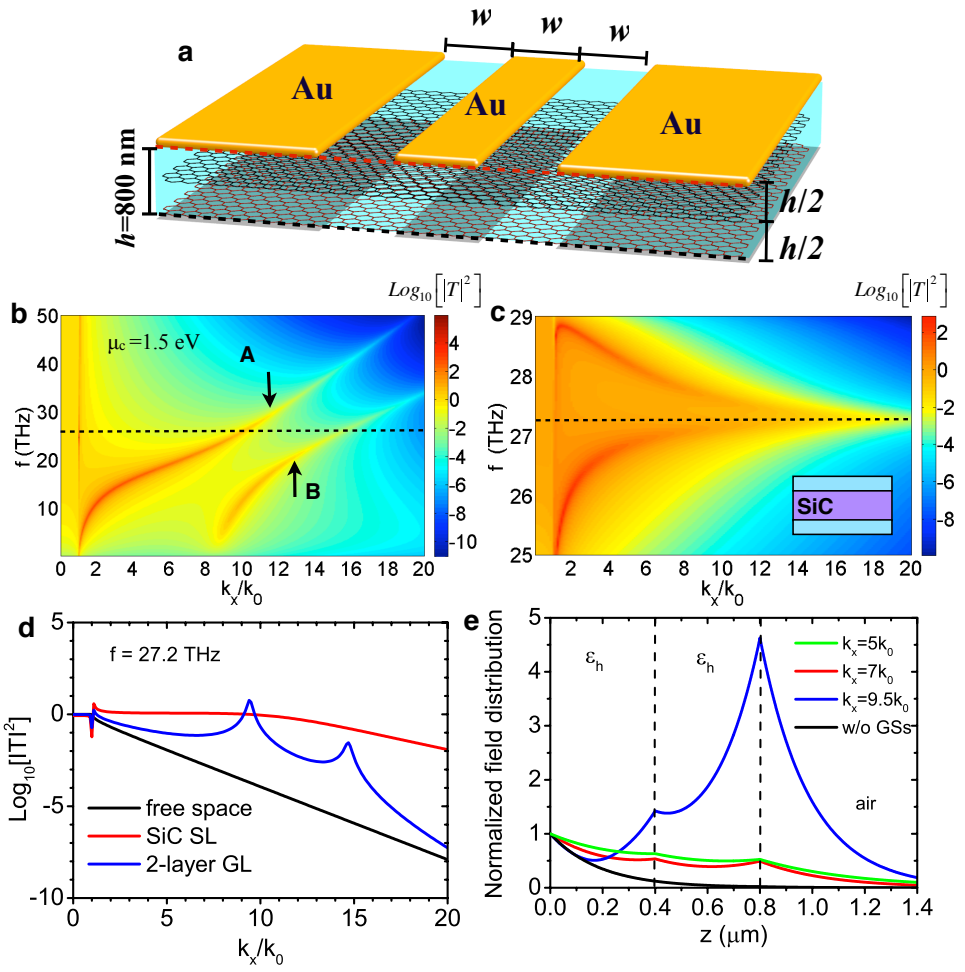


FIGURE 6.1: Comparison of the transmission of the 2-layered GL and the SiC superlens. (a) Sketch of a 2-layered GL under the Au double slit. The red and black dashed lines indicate the positions of object plane and image plane chosen for later numerical simulations. (b) The calculated spectral transmission of a 2-layered GL with the thickness of 800 nm under the applied chemical potential $\mu_c$ = 1.5 eV. (c) The spectral transmission of a typical superlens with the material combination of SiC and $SiO_2$. (d) Comparison of the transmission for those two cases in (b) and (c) at the same frequency $f = 27.2$ THz. (e) Calculated electric field distribution for different evanescent components through the 2-layered GL with $\mu_c = 1.5$ eV: $k_x = 5k_0$ (light green), $7k_0$ (red) and $9.5k_0$ (blue). The black dashed lines indicate the positions of the GSs. For comparison, the case without the GSs (black) is also shown in the same figure.

Moreover, in Fig. 6.1b a significant enhanced transmission (warm colors) is also observed in this GL at very high spatial frequencies, indicating the enhancement of evanescent fields. To better show this performance, let us compare the transmittance of the double-layer GL, the SiC-superlens and the case of free space at the same frequency $f = 27.2$ THz ($= 11$ $\mu$m, the resonance of the SiC-superlens) in Fig. 6.1c. It is clearly seen that in free space the transmittance of subwavelength components decays very fast. On the other hand, in the SiC superlens the transmittance for all evanescent waves is uniformly amplified due to the resonant nature of surface modes at the matching SiC-$SiO_2$ interface, leading to nearly perfect imaging in the near field. The two-layer GL is an intermediate case between the SiC-superlens and the case of free space. For example, for $k_x = 8k_0$, $|T_{\text{bare}}| = 0.02 < |T_{\text{GL}}| = 0.3 < |T_{\text{SL}}| = 0.9$. Practically, this enhancement ($|T_{\text{GL}}|/|T_{\text{bare}}| = 15$) can already enable near-field applications. For example, the probing tip in the s-SNOM can also detect weak evanescent fields emerging from structures buried below a surface, as demonstrated recently in subsurface imaging [85, 87]. Combining the GL with the SNOM, this capability will be dramatically improved by a further enhancement of the evanescent field, and thus yield a significant increase in sensitivity and resolution (c.f. Section 6.3).

For the possibility of near-field imaging, it can be noticed that the enhanced transmission curve ($|T| > 0.25$) stays relatively smooth and flat in the range before approaching the first peak A ($k_x \leq 8k_0$), which means that evanescent fields in this range can be effectively transferred through the GL avoiding signal distortion [117]. To better understand this nearly uniform enhancement, Figure 6.1e shows the calculated electric field distributions for different subwavelength components through the GL. It is seen that all these components are enhanced due to the presence of graphene layers, and the strongest enhancement is obtained at the position of peak A ($k_x = 9.5k_0$). Intuitively, one could assume that the larger the evanescent fields are, the better the subwavelength resolution would be. However, the strong field amplification at $k_x = 9.5k_0$ may not be useful for subdiffractive imaging because this non-uniform enhancement in the $k_x$ spectra could cause a potential distortion in the reconstructed image. For the components of $k_x \leq 8k_0$, the field enhancement is more uniform, which suggests a possibility of subwavelength imaging with a resolution in this spatial frequency range.

The two peaks in Fig. 6.1b do not combine at a particular frequency is because of geometric symmetry breaking. As seen in Fig. 6.2a, the two peaks will also

combine into at a specific frequency for a symmetric structure (d-g-d-g-d). When the system is non-symmetric (d-g-d-g-a), these two modes will separate as shown in Fig. 6.2b. Here I notice that the similar enhancement of evanescent fields can be also obtained for the symmetric structure. The reason for discussing the periodic structure shown in Fig. 6.1a is because it can be easily extended to the multilayered case.

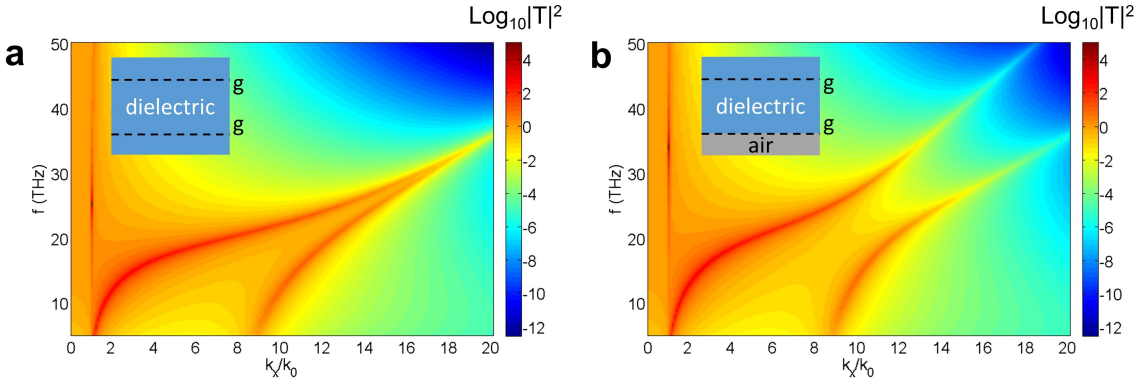


FIGURE 6.2: Comparison of a symmetric and non-symmetric structure. (a) Spectral transmission of a symmetric GL (dielectric-graphene-dielectric-graphene-dielectric). (b) Spectral transmission of a non-symmetric GL (dielectric-graphene–dielectric-graphene-air).

The second peak B in Fig. 6.1b results from standing waves between graphene layers. These Fabry-Perot resonances can be determined by the period of graphene layer in the total system following a relation as shown below,

$$\cos(\phi) = \cos(k_z d) - \frac{i\sigma_g k_z}{2\epsilon_0 \epsilon_d \omega} \sin(k_z d), \phi = k' m d = n\pi, \tag{6.8}$$

where $k_z = \sqrt{\epsilon_d k_0^2 - k_x^2}$, $k'$ is an effective wavevector, $d$ is the period of unit cell (the thickness of each dielectric layer), $m$ is the total period number and $n$ is an Integer. Figure 6.3 shows the transmission of layered GL with different periods. It is visible that the first peak A does not change too much at these cases, because periodically adding the graphene layer into the system will not obviously change the dispersion of surface modes supported by each graphene layer. In contrast, the Fabry-Perot resonant mode will split into multiple modes due to the addition of periods, following a simple relation of that the mode number $N = m - 1$, which is consistent with the results reported in [99, 118].

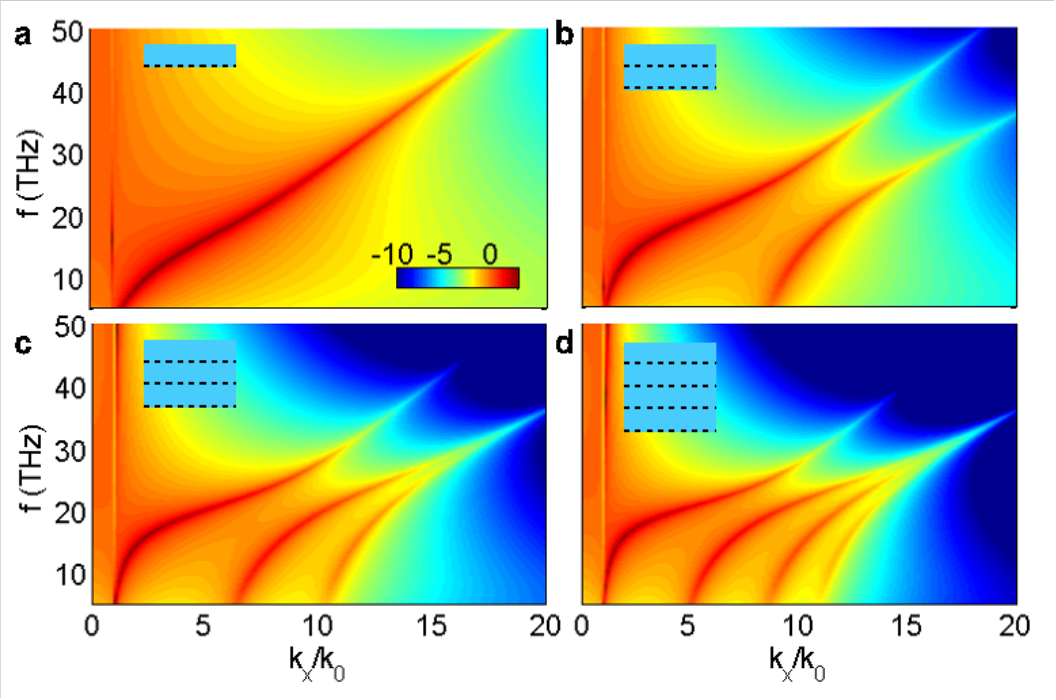


FIGURE 6.3: Transmission of layered GL with different periods. The period (a) 1 to (d) 4. Each period is 200 nm.

To demonstrate the imaging ability of the suggested GL, I perform numerical simulations using a commercial software based on the finite element method. In these simulations, the two-layer GL is used to image a typical resolution-testing pattern: an Au double slit. As sketched in Fig. 6.1a, the double slit with the width $w = 800$ nm locates on the dielectric layer of the GL. The center-to-center separation of the slit is chosen to be $2w = 1.6$ $\mu$m. For the sake of simulations, I treat graphene layers as thin metal layers (thickness 1 nm) with an equivalent permittivity $\epsilon_{\text{eq}}$ taking into account the realistic surface conductivity of the graphene [110, 111]. For example, $\text{Re}(\epsilon_{\text{eq}}) = -720$ is obtained at the frequency of 27.2 THz for the graphene chemical potential $\mu_c = 1.5$ eV.

The simulated intensity distribution of the total electric field at $f = 27.2$ THz is presented in Fig. 6.4a. The electric fields through each slit are effectively transferred (without obvious decreases) by the GL, and thus the slits are also easily distinguished. From the line profile at the image plane shown in Fig. 6.4b, two well-separated peaks are clearly resolved for the case of the double slit on the GL, showing an improved subwavelength resolution ($\sim \lambda/7$) compared with the case without the GL. Furthermore, I also show the performance of this GL at

different frequencies in the same figure. The double slit can be resolved by the GL in the range from 26 THz to 30 THz, suggesting an intrinsic operating frequency range of at least 4 THz. Obviously, the good performance of operation bandwidth of the GL will provide more convenience in future practical applications, such as spectroscopic imaging or near-field lithography without exactly matching the frequency.

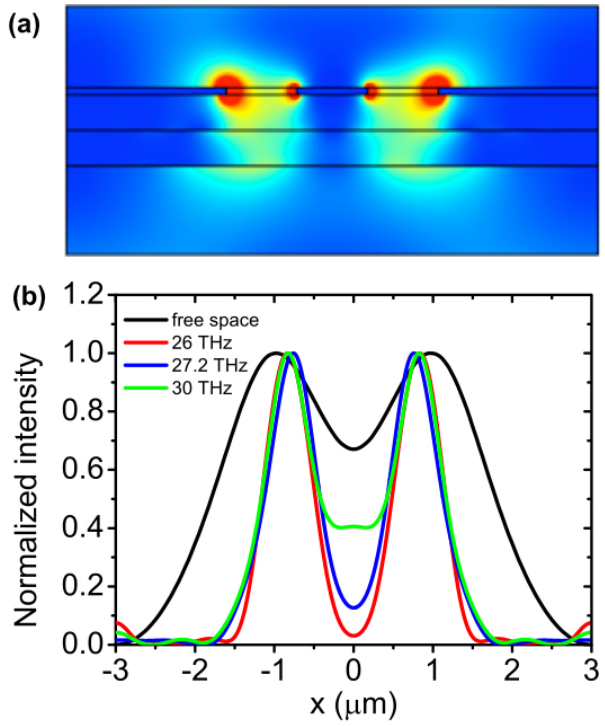


FIGURE 6.4: Imaging performance of the 2-layered GL. (a) Electric-field intensity distribution for the case using the 2-layered GL to image an Au double slit with the width $w = 800$ nm and the separation of $2w = 1.6$ $\mu$m at the frequency $f = 27.2$ THz. (b) Line profiles taken from the image plane at different frequencies: $f = 26$ THz (red), 27.2 THz (purple) and 30 THz (green). The case without the GL (black) is shown for comparison.

### 6.2.2 Bandwidth, tunability and loss-influence

The results of numerical simulations in Fig. 6.4 have proven that the proposed GL can achieve subwavelength imaging with a resolution of around $\lambda/7$ in a relatively wide frequency range for a constant chemical potential (or surface conductivity).

This covered frequency range can be also directly obtained in the calculation of the transmission. As shown in Fig. 6.5a, the transmittance of the component $k_x = 7k_0$ is plotted as a function of the frequency $f$ for the cases of the GL and the superlens. The frequency range obtained from the numerical simulations corresponds to the transmittance within the range $0.1 \leq |T| \leq 0.32$, roughly determining the condition where this GL can achieve subwavelength imaging. Based on this condition, I will present the possibility of tuning the imaging frequencies of the GL by changing chemical potentials.

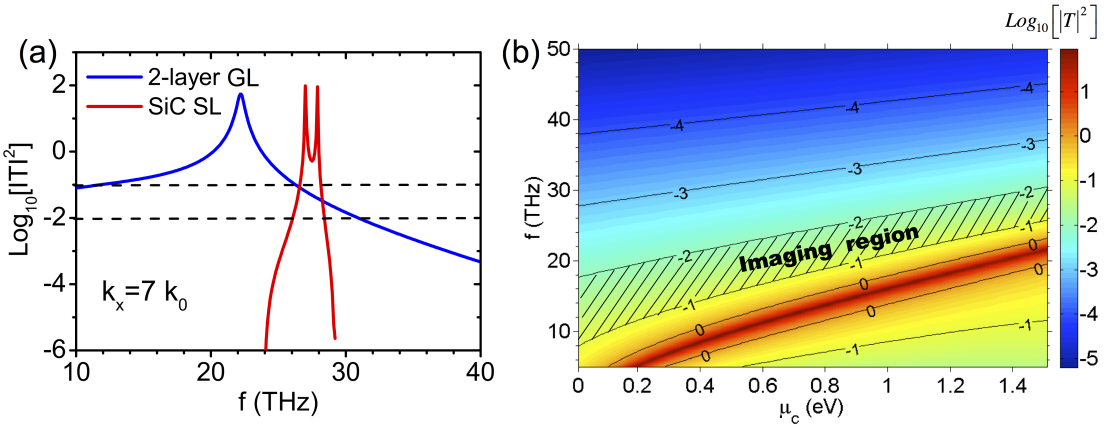


FIGURE 6.5: Tuning dependence on the chemical potential and the frequency. (a) The transmittance of the component $k_x = 7k_0$ as a function of the frequency $f$ for the cases of the GL (blue) and the superlens (red). (b) Contour plot of the transmittance of the GL as a function of the chemical potential and frequency. The imaging region is the green area marked with oblique lines.

Figure 6.5b displays the contour plot of the transmittance as a function of the chemical potential $\mu_c$ and frequency $f$. In principle, the imaging frequency range (marked with oblique lines) of the GL can be continuously tuned from mid- to far-infrared frequencies when decreasing the chemical potential from 1.5 eV to 0.1 eV. For example, the frequency corresponding to $|T| = 0.3$ (for $k_x = 7k_0$) will shift from 27.2 THz to 13 THz when changing the $\mu_c$ from 1.5 eV to 0.2 eV. It can be also noticed that the bandwidth of the GL will be broadened when it is tuned to work at lower frequencies. For the chemical potential $\mu_c = 0.2$ eV, the covered range of the GL is about 8 THz wide, from 12 THz to 20 THz. This better performance of the bandwidth at low frequencies is because the GL is becoming "thinner" compared to the operating wavelength, providing higher and more uniform transmission properties. In previous discussions, the chemical

potential of the graphene is chosen to be $\mu_c = 1.5$ eV for comparison with the SiC-superlens. However, a reasonable tuning range of the chemical potential is limited to $\mu_c \leq 1.2$ eV based on the current situation that a carrier density of up to $10^{14}$ $cm^{-2}$ has been realized in experiments [119, 120]. Therefore, as seen from Fig. 6.5b, the operating frequencies of our 2-layered GL are covering the range from 28 THz (maximum covered frequency at $\mu_c = 1.2$ eV) to 8 THz (minimum covered frequency at $\mu_c = 0.1$ eV). With this large tunability of imaging frequencies, our two-layer GL can definitely act as an ultra-broadband subdiffractional imaging system in the infrared regime.

In addition to the large tunability, I have also investigated the impact of material loss on the performance of the GL. The losses of our system may come from two different parts: the graphene and dielectric layers. According to recent experiments of s-SNOM imaging of graphene plasmons [78, 79, 121], both parts of losses can limit the performance of upcoming graphene-based plasmonic devices: in ref. [78], a small mobility of 1200 $cm^2V^{-1}s^{-1}$ resulted in high intrinsic graphene losses while in ref. [79] graphene with a higher mobility of 8000 $cm^2V^{-1}s^{-1}$ was used but IR losses of the $SiO_2$ substrate occurred. For the graphene, the momentum relaxation time $\tau$ indicates the level of the loss. Shorter relaxation time means larger scattering loss. In Sec. 6.2.1, a GL with a small loss was discussed: the relaxation time in graphene is $\tau = 0.5$ ps (corresponding to a mobility of about 15000 $cm^2V^{-1}s^{-1}$) and the dielectric layer is lossless. Now I will discuss the situation of the GL with larger losses. In Fig. 6.6a, I re-calculate the spectral transmission of the 2-layered GL by taking into account a large loss from both graphene ($\tau = 0.05$ ps for a mobility of about 1500 $cm^2V^{-1}s^{-1}$) and host material ($\mathrm{Im}[\epsilon_h] = 0.3$). At this case two transmission modes A and B (discussed in Fig. 6.1b) are suppressed due to the large loss, and the Fabry-Perot mode even totally disappears at this case. Interestingly, the transmission of evanescent components in the spatial frequency range of interest ($k_x \leq 8k_0$) is less influenced by the increased loss and still stays relatively large values. As shown in Fig. 6.6b, the transmission in this range does not change so much for different losses: the small loss, the reasonable loss ($\tau = 0.3$ ps for a mobility of about 8000 $cm^2V^{-1}s^{-1}$ and $\mathrm{Im}[\epsilon_h] = 0.3$) and the large loss. This loss-insensitivity means that the imaging performance of our GL will not be obviously affected by the loss, which is another important property for future practical applications.

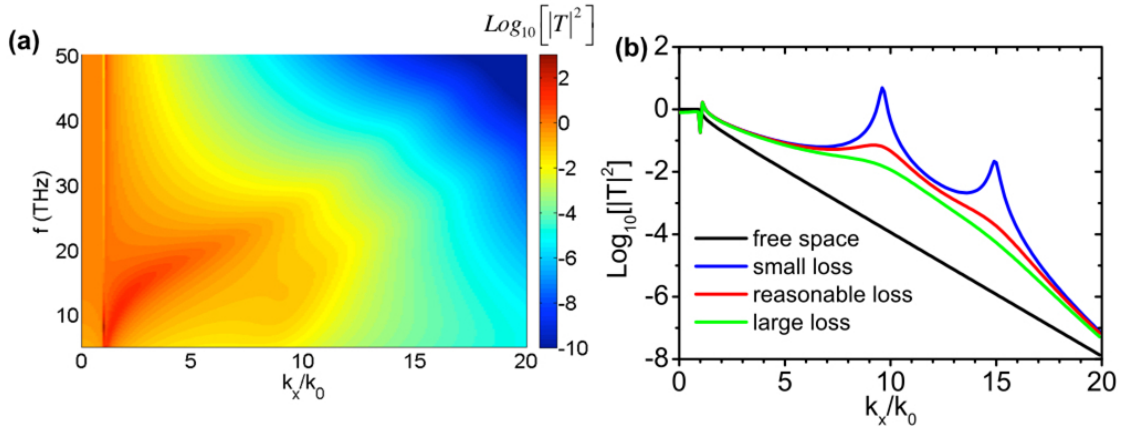


FIGURE 6.6: Effect of loss on the imaging properties of the GL. (a) Spectral transmission of a 2-layered GL with large losses ($\tau = 0.05$ ps and $\mathrm{Im}[\epsilon_h] = 0.3$) under the applied chemical potential $\mu_c = 1.5$ eV. (b) Comparison of the results for three cases with a small loss ($\tau = 0.5$ ps), a reasonable loss($\tau = 0.3$ ps and $\mathrm{Im}[\epsilon_h] = 0.3$), and a large loss ($\tau = 0.05$ ps and $\mathrm{Im}[\epsilon_h] = 0.3$) at the frequency $f = 27.2$ THz.

### 6.2.3 Multilayered configurations

As above discussed, higher imaging frequencies require larger chemical potentials in our GL. Decreasing the operating temperature of the system might lower the requirement of chemical potentials [110], but will introduce some experimental inconveniences compared to room temperature. Here I extend the GL to multilayer operation by adding more GSs and shortening the distance between two neighbour graphene layers, which also help our device to cover higher frequencies with lower chemical potentials. To demonstrate this idea, I choose the cases of a 4-layered GL and an 8-layer GL as the examples, while keeping the total thickness of each system to 800 nm constant for comparison. The separation of GSs is reduced to 200 nm for the 4-layer GL and 100 nm for the 8-layer GL. In Fig. 6.7a and b, I show the transmission for these two cases with relatively low chemical potentials: $\mu_c = 1$ eV for the 4-layer GL and $\mu_c = 0.6$ eV for 8-layer GL. Similar with the results of the two-layer GL, obviously large transmission of evanescent components is also found in both multilayered cases (detailed examination shown in Fig. 6.7c), which strongly demonstrates that a multilayered GL can enhance evanescent waves with low chemical potential.

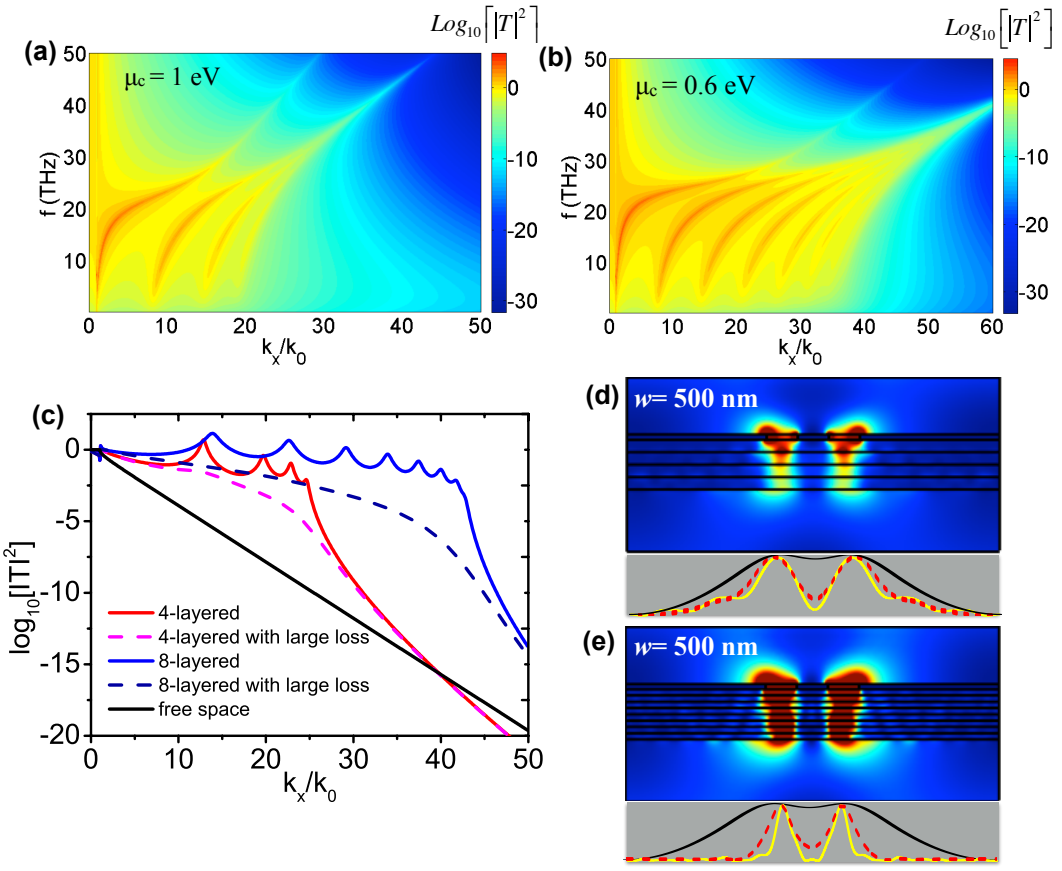


FIGURE 6.7: Performance of the multilayered GL. Spectral transmission of multilayered graphene lenses: (a) 4-layered GL with $\mu_c = 1$ eV and (b) 8-layered GL with $\mu_c = 0.6$ eV. (c) Comparison of the transmission for the 4-layered GL and 8-layered GL with different losses at the frequency $f = 27.2$ THz. Electric-field intensity distribution for the cases of (d) 4-layered GL and (e) 8-layered GL at 27.2 THz. Lines profiles of intensity distribution at the image plane for the cases of graphene lenses with different losses: small losses (yellow solid lines) and large losses (red dashed lines). The case without the GL (black) is shown for comparison.

These results are attributed to the increasing number of the GSs. In the two-layer GL case, only two GSs contribute to the enhancement of evanescent waves. Effectively transferring subwavelength information between these two sheets with a large separation of 400 nm requires the large surface conductivity (or chemical potential) in each layer. Here when the GL is extended to the multilayered configuration, more graphene layers with smaller separations can also provide the same enhancing effect of evanescent waves. Therefore, the average enhancement of each graphene layer is lower than that of 2-layered case, resulting in the lower requirement of chemical potential in each sheet.

Another consequence of the multilayered configuration is the improved resolution. As discussed before, the resolution of the GL is limited by surface plasmons on the GSs. Narrowing the separation of graphene layers can lead them to support surface modes with smaller wavelength, resulting in the improvement of resolutions. As seen in Fig. 6.7c, for both multilayered cases the first transmission peak A introduced by coupled surface modes shift to higher spatial frequency. For instance, for the 4-layered case the peak shifts to about $k_x = 14k_0$ and $k_x = 17k_0$ for the 8-layered case. Therefore, their resolutions are improved to over $\lambda/10$. In principle, the smaller the layer period is in the multilayered GL, the better resolution it can achieve. For an example of an 80-layered GL (the layer separation is 10 nm) at $f = 27.2$ THz, the resolution can be further improved to a value of better than $\lambda/50$. In an extreme situation that the separation between the GSs is reduced to match the realistic thickness of the graphene layer, the multilayered GL can work as a multilayered graphene-based SL at ultraviolet (UV) frequency, which is very similar with a recent proposal of an ultraviolet graphene-based hyperlens [122]. Therefore, another physical picture to understand the coupling of graphene layers is that the multilayer-graphene-based structure can be seen as a metamaterial with hyperbolic dispersion relation [123] (c.f. Section 1.2).

To further compare the resolution capabilities of the different multilayered graphene lenses, in Fig. 6.7d and e, these lenses are used to image a 500-nm wide double slit with the separation of 1 $\mu$m at $f = 27.2$ THz (about a resolution of $\lambda/11$). It appears that, the slits are well resolved for both cases. And consistent with the analysis, the performance of the 8-layered GL is better than that of the 4-layered case. Moreover, similar with the 2-layered case the effect of losses also does not obviously affect the performance of the multilayered lenses.

### 6.2.4 Hybrid graphene-superlens imaging system

In previous discussions, it is assumed that the graphene layer is supported by non-dispersive dielectric layers. However, in many practical cases, the graphene layer is transferred (or fabricated) onto a substrate (SiC, $SiO_2$/Si)with obvious phonon resonances [78, 79, 106]. The recently reported interaction between the graphene SPs and surface phonons of polar substrate enable even stronger local field enhancement and confinement [124–128]. Here I also investigate the case that two graphene layers are combined with a SiC-superlens as sketched in Fig.

6.8. I find that this new system exhibits the combined advantages of both the SiC-superlens and the GL.

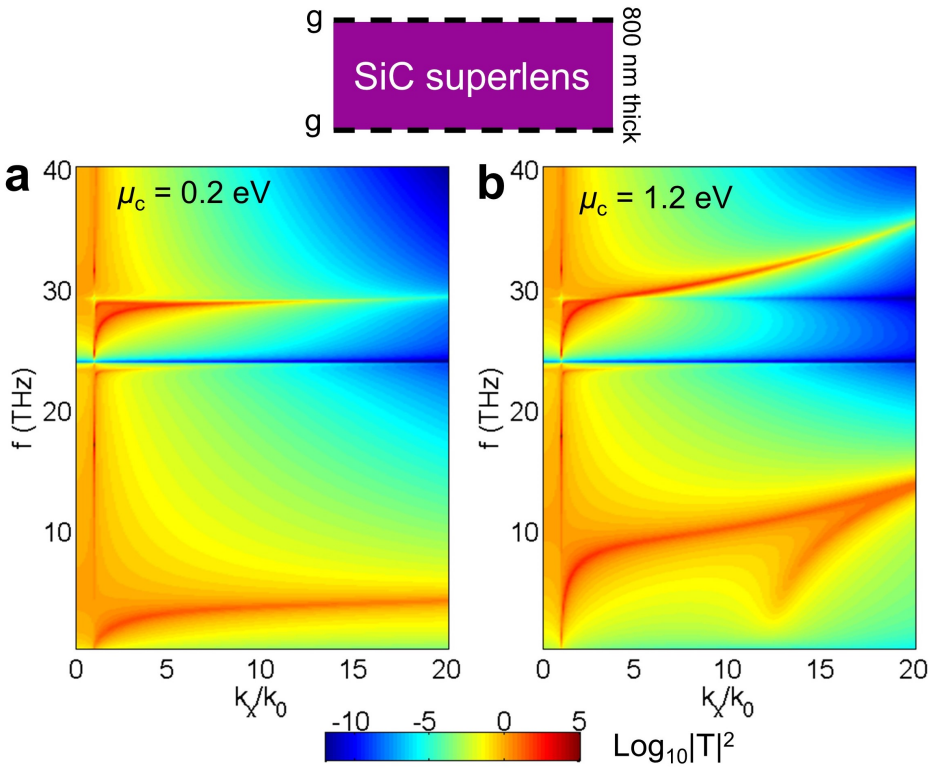


FIGURE 6.8: The combination of two graphene layers and a SiC superlens. (a) low doping ($\mu_c = 0.2$ eV) in graphene, (b) large doping ($\mu_c = 1.2$ eV) in graphene.

I calculate the transmission of this combined system for two different chemical potentials. At low doping (chemical potential $\mu_c = 0.2$ eV), I observe a transmission peak of high-$k_x$ components at about $f = 30$ THz, which is due to the enhancement of the SiC-superlens. Another transmission peak resulting from the graphene-plasmon enhancement is found at a lower frequency around $f = 3$ THz. When applying a higher chemical potential of $\mu_c = 1.2$ eV, both transmission peaks are tuned. Additional, a new Fabry-Perot peak (around 10 THz) appears due to the strong reflection between two highly doped graphene layers. This hybrid system can be seen as a new imaging combing the uniform enhancement of evanescent modes of the SiC-superlens and the tunablity of the GL. Promisingly, recent experimental advances on the graphene-hBN metamaterial structures provide the possibility to realize such a hybrid imaging system [80, 121].

## 6.3 Experiments on graphene-enhanced near-field imaging

As introduced in Chapter 3, the SNOM uses a near-field probe to pick up evanescent information before it is decayed, which allows the resolution down to 10-nm scale. However, this mechanism also implies that the SNOM probe needs to be close to the investigated object. However, for imaging deeply buried (or embedded) structures as sketched in Fig. 6.9a, evanescent fields already decay exponentially before being picked up by the probe. Thus the SNOM is unable to achieve a useful resolution.

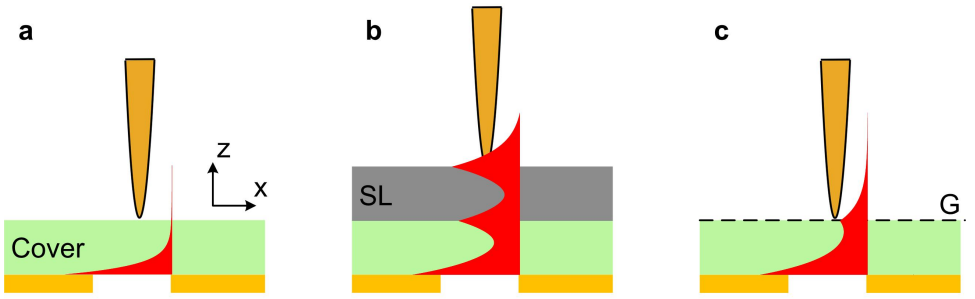


FIGURE 6.9: Distinct near-field imaging configurations for resolving deeply buried structures. (a), conventional SNOM. (b), superlens-combined SNOM. (c), graphene-enhanced SNOM. SL: superlens, G: graphene. Red plots in each sketch show the magnitude distribution of evanescent fields along the z-direction (without considering the influence of the SNOM tip).

In order to overcome the depth limitation in SNOM [85, 86, 95], one idea is to combine the SNOM with the superlens. In a superlens-SNOM combination as shown in Fig. 6.9b, the superlens significantly enhances evanescent fields and transfer a high-resolution image to its top surface. The SNOM tip further picks up this image for visualization. Recent experiments demonstrate that this combination can resolve $\lambda/15$-sized objects in a depth of several hundred nanometers [24, 25], offering a non-destructive way to characterize (deeply) buried objects. However, since it is highly challenging to prepare a good-quality (small intrinsic loss) superlens on top of the object of interest, this method would be hardly used in practical applications.

The concept of graphene lens might provide a more feasible solution to improve the performance of near-field subsurface imaging. Considering a monolayer graphene is transferred onto the top of the sample, it is also able to support surface plasmon polaritons with ultra-small plasmon wavelengths $\lambda_p$ [78, 79]. These subdiffractive waves can penetrate the sample surface (involving the vertical decay length) to enhance and probe the evanescent information of the subsurface and sub-diffraction-limited object. In this case, the resolution of the combined imaging system is not limited by the free-space wavelength, but mainly by the wavelength $\lambda_p$ of graphene plasmons. As shown in Fig. 6.9c, the graphene offers a weaker enhancement of evanescent fields compared to that in the superlens (see the comparison of field distributions in Fig. 6.9a-c), because it does not fulfill the resonant condition ($\epsilon_g = -\epsilon_h$). Here I experimentally verify that this enhancement provided by monolayer graphene is sufficient enough to improve the resolution of near-field subsurface microscopy. Since graphene can be easily transferred onto the sample of interest [129–131], this novel method would have great application prospects.

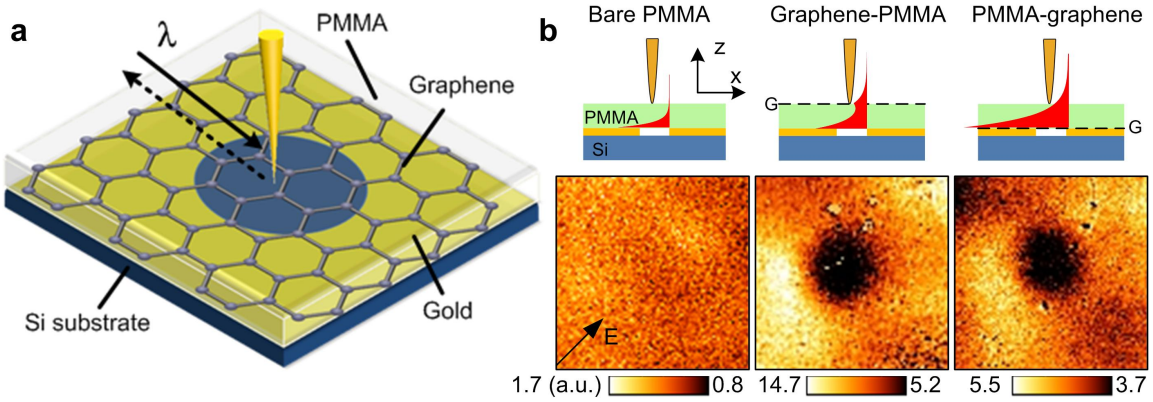


FIGURE 6.10: Graphene-enhanced near-field microscopy of a buried hole. (a) Sketch of the experiments. A 1.5-$\mu$m-diameter hole covered by monolayer graphene and a 500-nm-thick PMMA layer is imaged by the s-SNOM. (b) Infrared near-field amplitude images for the cases covered with a bare PMMA layer (left panel), graphene-PMMA (middle panel) and PMMA-graphene (right panel). In both graphene-involved cases, the subwavelength hole can be resolved due to the graphene enhancement. Black arrow indicates the polarization direction of the illumination light. Sizes of all images are 4 $\mu$m $\times$ 4$\mu$m. Red plots in each sketch indicate the magnitude distribution of evanescent fields along the z-direction.

The near-field imaging experiments are sketched in Fig. 6.10a. A 1.5-$\mu$m-diameter

hole is prepared in an Au layer (40-nm-thick, on Si substrate) by using the sphere-mask lithography [60]. Monolayer graphene attached with a 500-nm-thick PMMA (Poly(methyl methacrylate)) layer is transferred (in water) to cover the hole (c.f. Appendix A). Here, the PMMA layer does not only act as a spacer layer, but also introduces a strong n-type doping in graphene [131, 132]. As shown in Fig. 6.10b, two distinct graphene positions are investigated: 1) graphene on the top of the system (graphene-PMMA configuration) and 2) graphene adjacent to the hole (PMMA-graphene configuration). In both configurations, graphene can provide the same enhancement of evanescent fields (see red plots in Fig. 6.10b), avoiding the fast decay of subwavelength information in the case covered with a bare PMMA layer. Here, our calculations of field distributions do not include the influence of the scanning tip in the experiments, which are presented for qualitative indications of the graphene enhancement. In fact, the role of the SNOM tip is important, which might have certain differences for the two graphene positions. In the graphene-PMMA configuration, the tip is close enough to the graphene. Strongly concentrated near fields at the tip apex can excite graphene plasmons. In contrast, in the PMMA-graphene configuration, the tip is far away (500 nm) from the graphene layer. In this case, the near fields launched by the tip cannot be sufficiently coupled to the graphene for exciting the plasmons. Instead, the gold edges of the hole close to the graphene might launch the surface plasmons. It should be emphasized that in both cases the tip itself is 500 nm far away from the underlying subwavelength-sized hole. Thereby the recorded optical image of the hole should be due to the graphene enhancement.

All investigated samples are illuminated by an infrared line-tunable $CO_2$-gas laser. A metallic s-SNOM tip scans across the sample surface to collect the near-field optical information of the buried hole. For comparison, a control experiment is conducted in the case that the hole is only covered by a 500-nm-thick PMMA layer. Near-field amplitude images taken at 11.3 $\mu$m are shown in Fig. 6.10b. The deeply buried hole can be hardly seen in the case without the graphene. On the other hand, it is well resolved in both graphene-involved cases, indicating that graphene introduces an obvious enhancement of evanescent information. Interestingly, besides the dark contrasts of the hole, the field distribution (from the edge scattering [60]) outside the hole is also reconstructed in both graphene-enhanced images (see bright areas). Moreover, I notice that the near-field signals recorded in the graphene-PMMA configuration are higher than those in the PMMA-graphene case (for the same experimental condition). This might be as a consequence of

the tip-graphene interaction in the former configuration, which is missing in the latter case due to the 500-nm tip-graphene distance.

Figure 6.11a presents a detailed wavelength-dependent experimental study of the graphene-enhanced near-field imaging (the PMMA-graphene configuration). The

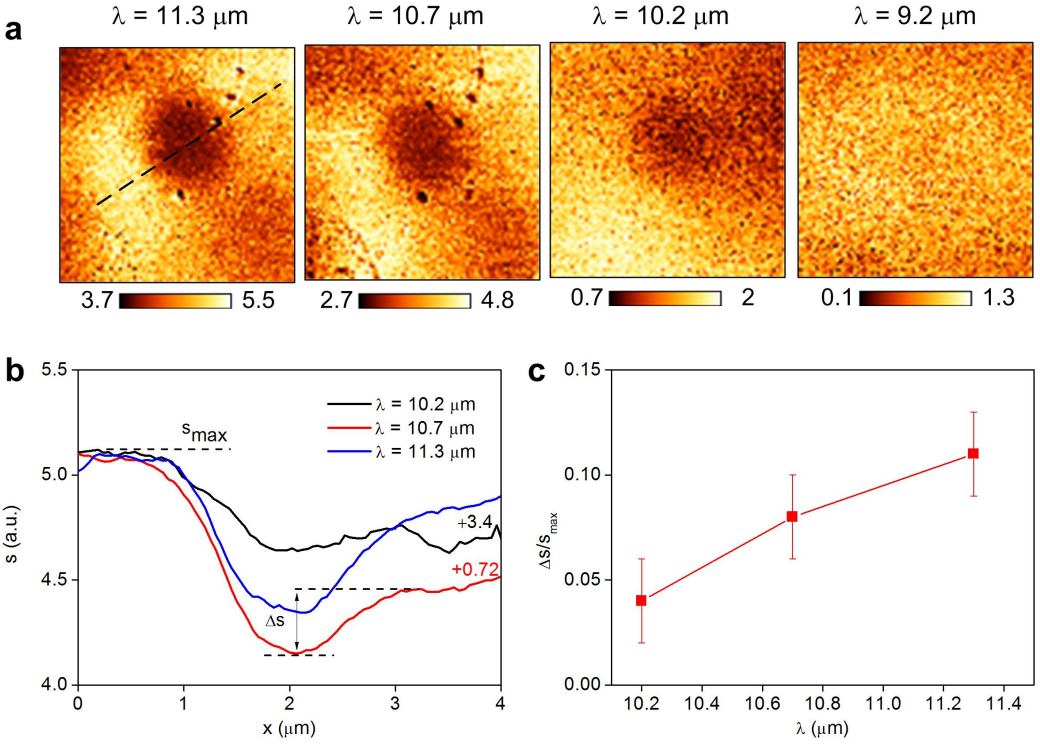


FIGURE 6.11: Wavelength dependence of graphene-enhanced near-field imaging. (a) Infrared near-field amplitude images of the buried hole taken at the wavelengths from $\lambda = 11.3$ $\mu$m to $\lambda = 9.2$ $\mu$m. Sizes of all images are 4 $\mu$m $\times$ 4 $\mu$m. (b) Line profiles of the SNOM signals s across the images taken along the dashed line in a. The curves taken at $\lambda = 10.7$ $\mu$m and $\lambda = 10.2$ $\mu$m are shifted vertically with corresponding values for a better comparison. (c) The estimated contrast ($\Delta s/s_{max}$) of the hole as a function of the wavelength.

buried hole is imaged over a relatively wide wavelength range ($> 10.2$ $\mu$m), showing a working bandwidth of at least 1.1 $\mu$m. Line plots across the hole are shown in Fig. 6.11b. The resolved optical width (defined as a distance between the half-maximum at each side) of the hole is almost the same ($\sim 1.3 \pm 0.1 \mu$m) for three different wavelengths. The extracted contrast of the hole ($\Delta s/s_{max}$) as a function of the wavelength is presented in Fig. 6.11c. Quantitatively, the contrast gets worse when decreasing the excitation wavelength: the contrast ($\Delta s/s_{max} = 0.11$)

obtained at the wavelength of 11.3 $\mu$m is nearly three times as high as that ($\sim$ 0.04) at $\lambda = 10.2\mu$m.

Generally, a shorter imaging wavelength should yield a better resolution considering the diffraction limit. However, our observations in Fig. 6.11 are contrary to this intuitive thought. To understand this phenomenon, in Fig. 6.12a I calculate the transmittance ($|T(k_x, \lambda)|^2$) of the PMMA-graphene system as a function of in-plane ($x$-axis) wavevector $k_x$ and the wavelength $\lambda$. I use the graphene conductivity model shown in Eq. 6.1. This transmission plot describes the complete electrodynamics of the PMMA-graphene system, not only in the near field, but also in the far field. This is because the transmission properties of all the in-plane components, both propagating ($k_x < k_0$, $k_0$ being the wavenumber in free space) and evanescent waves ($k_x > k_0$), can be evaluated in the plot. Two transmission peaks are found in this dispersion plot. The one around $k_x = k_0$ indicates the light line in air. The other transmission peak (indicated by the black dashed line) represents the graphene plasmon mode. The in-plane components matching the graphene plasmon ($k_x \sim k_p$, $k_p$ being graphene-plasmon wavevector) lead to the maximum transmission peak of high-$k_x$ components found in transmission. This mode shows a curved wavelength-dependent resonance behaviour. This dispersion characteristic is different from that of the superlens, which usually has a flat dispersion for nearly all the high-$k_x$ components at the superlensing wavelength.

Detailed transmittance profiles at two different wavelengths are plotted in Fig. 6.12b. The case without the graphene layer is shown in the same figure for comparison. It can be seen that the graphene enhancement is not strictly restricted to the components close to the plasmon wavevector ($k_p(\lambda = 9.2\ \mu\text{m}) \approx 24k_0$, $k_p(\lambda = 11.3\ \mu\text{m}) \approx 20k_0$). For the components below the $k_p$ (like $k_p < 15k_0$, marked by grey color), the enhancement is also clear. For example, for the component $k_x = 11k_0$, nearly 7-fold enhancement can be found between the cases with and without graphene at $\lambda = 11.3\ \mu$m. Although the enhancement in this off-resonance regime is weaker than the cases close to the $k_p$, it still can provide two obvious advantages. One is to avoid the imaging distortion of propagating graphene plasmons. The other is the less influence of the graphene losses (cf. Section 6.2.2). Actually, our imaging experiments of the hole (the spatial frequency of the hole, $k_{x,h} \sim 7k_0$) are pre-designed to work in this non-resonance regime.

It is also noticed that when the wavelength is tuned to the smaller wavelength of 9.2 $\mu$m, the graphene enhancement nearly vanishes. Another similar evidence

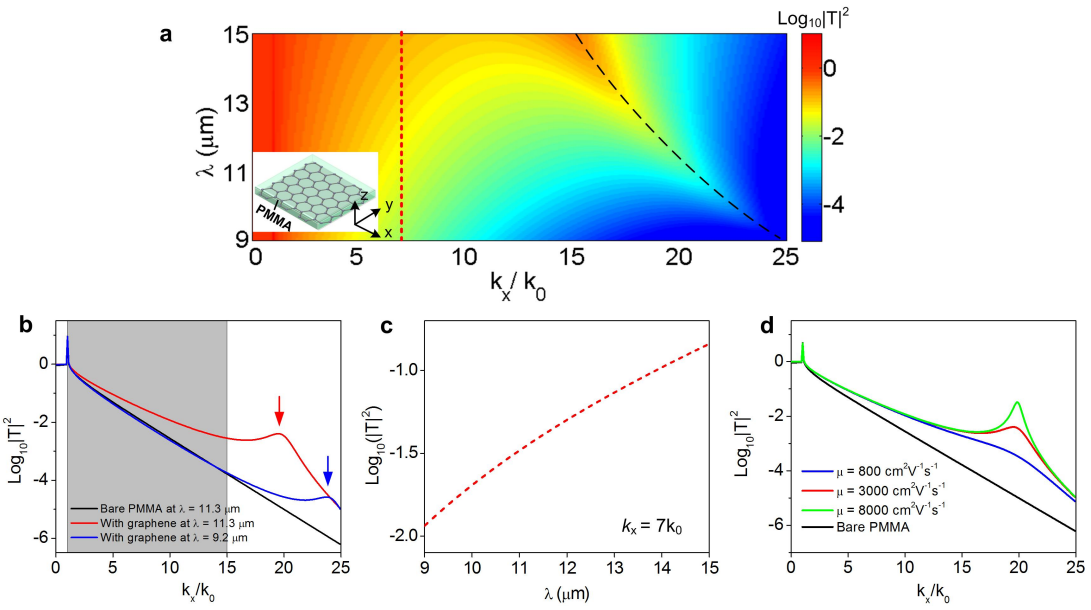


FIGURE 6.12: Monolayer GL for enhancing evanescent fields. (a) The transmittance of the graphene-PMMA system (sketched in the insert) as a function of $k_x$ and $\lambda$. Calculation parameters: Chemical potential $\mu_c = 0.6$ eV, graphene mobility $\mu = 3000$ cm$^2V^{-1}$s$^{-1}$ and PMMA permittivity $\epsilon_{\text{PMMA}} = 2.3$. The black dashed line indicates the position of the plasmon mode. The red dotted line marks the component of $k_x = 7k_0$ (the spatial frequency of the 1.5-$\mu$m-diameter hole). (b) The transmittance as a function at of $k_x$ at two distinct wavelengths. The case of a bare PMMA layer is also shown for comparison. (c) The $\lambda$-dependent transmittances for the component of $k_x = 7k_0$. Grey color marks the off-resonant regime discussed in the main text. (d) The $k_x$-dependent transmittances for different graphene mobilities.

is shown in Fig. 6.12c, in which the transmission of the component $k_x = 7k_0$ is plotted as a function of $\lambda$. The transmission is decreased with the decrease of the wavelength. These results agree with and explain our experimental observation that graphene-enhanced imaging only works sufficiently at larger wavelengths. It is worth to emphasize that in addition to the spatial resolution (limited by the $k_p$), it is also important to evaluate the signal level of transmitted evanescent fields (involving with the signal-to-noise ratio in the experiments). In order to obtain higher graphene enhancement at shorter wavelengths, it would be better to use a multi-layered configuration as discussed in Section 6.2.3.

The intrinsic graphene loss is an important material parameter influencing the imaging performance. A large loss due to small carrier mobility will result in a

plasmon damping, limiting the performance of graphene plasmonic devices [133–136]. For example, the propagation length of plasmon polaritons on graphene grown by chemical vapor deposition (CVD) [78, 137, 138] is shorter than that on exfoliated graphene [79] (note that the damping of CVD graphene can be reduced in a hBN/graphene heterostructure). Therefore, the graphene quality (i.e., large carrier mobility) is very crucial for most plasmonic applications. However, in our case, the graphene enhancement is not so sensitive to loss. This is because of its non-resonant nature (namely, working in the non-resonant regime of $k_x < k_p$), distinct from the resonant condition required in the conventional superlensing. Figure 6.12d shows the transmittance as a function of $k_x$ for three different mobilities: $\mu$ = 8000 cm$^2V^{-1}$s$^{-1}$ for typical exfoliated graphene [79], $\mu$ = 3000 cm$^2V^{-1}$s$^{-1}$ for CVD-grown graphene [78] (noting that the state of art CVD-growth graphene can also have very high mobility [121]) and $\mu_c$ = 800 cm$^2V^{-1}$s$^{-1}$ for heavily doped graphene [79]. It can be seen that, although the plasmon mode is suppressed with the decrease of the mobility, the transmittances in the range of $k_x < k_p$ are almost unchanged. This low influence of the loss would make the graphene enhancement very feasible for practical applications. From these theoretical results, I speculate that our heavily doped graphene layer suppresses propagating graphene plasmons in the experiments.

In order to quantify the graphene enhancement of evanescent fields, Line scans of s-SNOM tip across a graphene-covered Au grating (3.3-$\mu$m-period, 1.5-$\mu$m-gap) have been performed as sketched in the inset of Fig. 6.13a. Fourier transforms (normalized to the component of zero spatial frequency) of the line scans taken from the amplitude signals of s-SNOM are shown in Fig. 6.13a. Comparing the cases with and without graphene, the near-field graphene enhancement is clearly presented in this figure. In the graphene-covered case, the high spatial-frequency information of the grating (up to the third order harmonic) is recorded. In the case without graphene, only a small peak of the second order harmonic is found. I quantitatively estimate the enhancement using a peak visibility defined as $V = (F_p - F_b)/(F_p + F_b)$, where $F_p$ and $F_b$ are corresponding values of the grating harmonic peaks and the background, respectively. The background value $F_b$ is defined as the average value of two neighboring positions: $F_b = (F_A + F_B)/2$, as sketched in Fig. 6.13a. I obtain about 1.8-fold enhancement ($V_w/V_{wo}$, $V_w$ and $V_{wo}$ for the cases with and without graphene) for the first order grating harmonic ($k_x = 3.8k_0$), 3-fold for the second order ($k_x = 7.5k_0$) and 7-fold for the third order ($k_x = 11.3k_0$), respectively. Figure 6.13b presents Fourier transforms of the

graphene-covered sample taken at different illumination wavelengths. The peaks for the higher order harmonics are more pronounced at larger wavelengths. The third order harmonic can be revealed for the wavelengths $\lambda > 10.7$ $\mu$m, indicating a working-bandwidth of about 0.6 $\mu$m for this high-$k_x$ component.

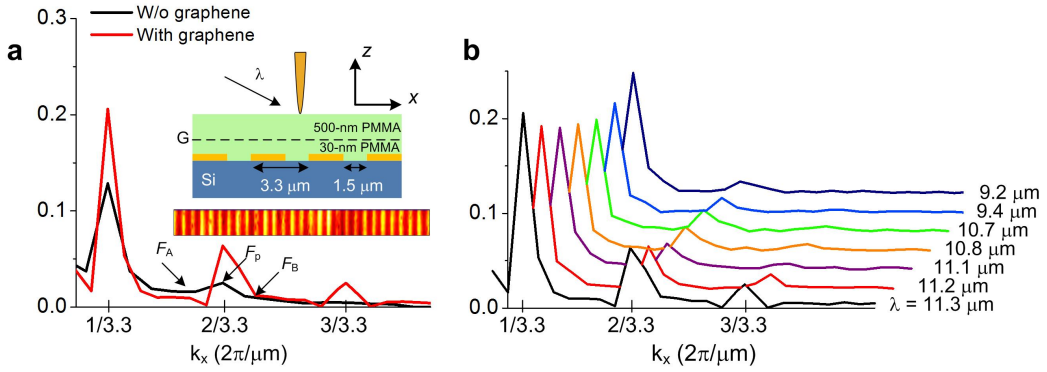


FIGURE 6.13: Near-field enhancement of monolayer graphene on an Au grating. (a) The insert shows the set-up of the experiments. A 3.3-$\mu$m-period grating is prepared on a Si substrate. A 30-nm-thick PMMA layer is coated as a spacer layer between the graphene and the grating. The s-SNOM tip scans across the 500-nm-thick PMMA layer. Fourier transform (red line) of line scans is taken from the amplitude image (at $\lambda = 11.3$ $\mu$m, shown below the sketch), normalized to the zero-frequency components. High spatial-frequency components, up to the grating's third order harmonic ($k_x = 11.3k_0$), are resolved by the graphene-enhanced s-SNOM system. The control case without the graphene (the grating covered with a bare 500-nm-PMMA film, black line) is shown for comparison. (b) Fourier transforms of the graphene-covered data taken at different wavelengths. They show that the graphene enhancement is weaker at shorter wavelengths.

## 6.4 Conclusion

In summary, I have introduced a novel graphene-based device enabling the enhancement of evanescent waves for near-field subwavelength imaging. Due to the non-resonant enhancement provided by the GSs, this GL yields new promising properties including broad intrinsic bandwidth and low sensitivity to loss, together with a still good subwavelength resolution of around $\lambda/7$ for a two-layer case and over $\lambda/10$ for the multilayered configuration. Most importantly, due to the large frequency-tunability via the dynamical tuning of chemical potentials, our proposed GL can act as an ultrabroadband sub-diffraction-limited imaging device to in principle cover the nearly whole mid- and far-infrared wavelength range. I also notice the fact that layered graphene structures are commonly used in graphene electronics (like graphene transistors) [139]. This does not only mean that the fabrication technology of such a GL is really mature, but also suggests that our concept may be directly useful for these electronic devices, such as for subsurface imaging of defects with the help of near-field microscopy.

Besides these presented exciting results, the GL concept further offers other bright prospects: for example, a possibility is to roll the planar GL into a cylindrical shape, which may provide a tunable magnifying lens for far-field imaging at IR and THz frequencies. Moreover, since graphene is two-dimensional (2D) conducting sheet, our concept of using conducting sheets for subwavelength imaging can also be generalized to that of a 'conducting sheet lens' and easily transferred to other conventional systems like 2D electron gases [140], opening up various exciting ways to achieve broadband subwavelength imaging with semiconductor heterostructures.

In addition to the theory of the GL, I have also experimentally demonstrated that monolayer graphene can significantly enhance evanescent fields for improving the subsurface imaging capability in near-field microscopy. The low influence of material losses and the great flexibility of sample integration will make graphene feasible in various practical applications such as nondestructive mapping of doping concentrations in semiconducting nanowires [96], subsurface defect detections in material growth [141] and noninvasive imaging of subcellular biological phenomena [69, 142]. Further tunable experiments by gate-tuning or chemical doping [143, 144] will yield a frequency-tunable effect to cover a broader wavelength range for infrared spectroscopic applications like vibration absorption spectroscopy [70]

and nanoscale material identification [73]. Moreover, I also note that the presented imaging mechanism is not only restricted to the use of graphene, but also suitable for other two-dimensional materials like transition metal dichalcogenides (for supporting SPPs) and hBN (for supporting SPhPs) [42].

# 7 Near-field imaging through a natural hBN hyperlens

Optical imaging beyond the diffraction limit was one of the primary motivations for negative-index metamaterials [17, 18, 32], resulting in Pendry's perfect lens [10] and the more attainable superlens [10, 11, 22, 24] (c.f. Chapter 1). While these approaches offer sub-diffractional resolution, they do not provide a mechanism for magnification of the image. The hyperlens based on hyperbolic metamaterials has been theoretically considered and experimentally demonstrated to provide simultaneously subdiffractive imaging and magnification [33–35]. However, man-made hyperbolic metamaterials are of large absorption losses and requires complex fabrication. In this Chapter, I present theoretical and experimental studies of near-field optical imaging through a flat slab of the low-loss, natural hyperbolic material, hBN [42, 43]. This thin hBN layer exhibits wavelength-dependent multifunctional operations, offering both an enhanced near-field imaging of single buried objects with down to $\lambda/32$ resolution (0.4 $\mu$m at $\sim$ 12.8 $\mu$m), as well as enabling an enlarged reconstruction of the geometric outline of the investigated objects. Both the excellent resolution and the multifunctional operation can be explained based on the volume-confined, wavelength dependent propagation angle of two types of hyperbolic polaritons. Our results provide both the understanding of near-field imaging performance through this natural hyperbolic media, as well as inspire their exciting potential for guiding and sensing of light at an extreme sub-diffractional scale.

[1] Content of this Chapter involved in the publication [P4]

## 7.1 Introduction

Hyperbolic media [32] enable many unusual optical applications such as hyperlensing [33–35], negative refraction [36, 37], enhanced quantum radiation [39], nanolithography [40] and sub-diffractional resonators [41, 43]. Very recently, it was demonstrated that the highly directional propagation of volume-confined, hyperbolic polaritons is key for these sub-diffractional phenomena [40, 42, 43]. Their directionality derives from the sign and magnitude of the two principal (in- and out-of-plane) components of the dielectric-permittivity tensor ($\overrightarrow{\epsilon} = \mathrm{diag}[\epsilon_{xx}, \epsilon_{yy}, \epsilon_{zz}]$ ), which have opposite signs in hyperbolic materials. The propagation angle $\theta$ (e.g. the angle between the Poynting vector and the $z$-axis) of hyperbolic polaritons in hyperbolic media can be roughly approximated as [43]

$$\theta = \frac{\pi}{2} - \frac{\sqrt{\epsilon_z(f)}}{i\sqrt{\epsilon_t(f)}}, \tag{7.1}$$

where $\epsilon_t = \epsilon_{xx} = \epsilon_{yy}$ and $\epsilon_z = \epsilon_{zz}$ are the in- and out-of-plane dielectric permittivities of the hyperbolic medium, respectively. The basic physics governing the hyperbolic polaritons can be understood similarly from the surface plasmon polariton propagating at a metal-dielectric interface. Since principal dielectric components of hyperbolic media show distinct dielectric responses (namely, $\epsilon_t < 0$ and $\epsilon_z > 0$ or $\epsilon_t > 0$ and $\epsilon_z < 0$), their angular-dependent dielectric perimittivities can equal zero at a special angle. This angle determines a virtual boundary between the negative-$\epsilon$ and positive-$\epsilon$ responses of hyperbolic media, which allows the propagation of polariton modes inside bulk hyperbolic media (n analogy with SPPs on a metal/dielectric interface). Therefore, by controlling the ratio of the two principal dielectric components, the propagation direction of hyperbolic polaritons can be tuned.

Hyperbolic media have been usually explored through man-made hyperbolic metamaterial structures, such as metal-dielectric multilayers [35, 36], nanowire [37, 38] or nano-pyramid arrays [41] embedded within a dielectric medium. In hyperbolic metamaterials, the effective dielectric permittivities are determined by the geometric parameters of their subwavelength unit cells [32]. As such, the maximum wavevector k that can be induced to propagate through the material is limited by the size of the artificial unit cell. This in turn limits the degree of optical confinement and spatial resolution that can be realized. Furthermore, the high losses

associated with noble metals [145–147] used in man-made hyperbolic metamaterial structures result in short propagation lengths, quite broad resonance linewidths and in terms of hyperlens designs, low transmission efficiency.

During the search for better 'plasmonic' materials [146, 147], polar dielectrics capable of supporting phonon-polaritons such as silicon carbide [53, 54, 59, 60, 148] and hBN [42, 43, 149] have been demonstrated as superior alternatives to metals at mid-infrared to THz frequencies. Interestingly, many phonon-resonant materials such as quartz [150], zinc oxide [151], calcite[44] and hBN [42, 43, 149] are natural hyperbolic materials [13, 14, 45]. These natural hyperbolic materials support hyperbolic polaritons within homogeneous crystals with atomic-scale unit cells, thus the upper limit on the highest propagating wavevectors k associated with artificial metal-dielectric hyperbolic metamaterials is no longer an issue. Instead, photonic confinement within tiny volumes in the few nanometer range becomes possible. This was recently demonstrated by Dai *et al.* [42] where surface phonon polariton propagation within a 3 monolayer ($<$ 1 nm) thin flake of hBN was reported. It is the propagation of such high-$k_x$ fields that are scattered off or launched from deeply sub-diffractional objects that is at the heart of super-resolution imaging. These benefits are also coupled with a drastic reduction in the optical losses compared to hyperbolic metamaterials, which results in improved performance, i.e. higher field confinement [42, 43] and improved image resolution.

In contrast to hyperbolic metamaterials reported to date, hBN offers the additional functionality of sub-wavelength imaging in different spectral regions through the presence of two separate spectral bands that exhibit inverted hyperbolic response (Fig. 7.1), making this an ideal material for exploring the basic phenomenon of hyperbolic polaritons. These two regimes are referred to as the lower and upper Reststrahlen bands [42, 43], where this term refers to the spectral range between the longitudinal (LO) and transverse (TO) optic phonons of a polar crystal where a negative real part of the dielectric function is observed. The presence of two bands results from the highly anisotropic crystal structure of hBN, where a,b- and c-axis oriented optical phonons are supported and are widely separated in frequency [152]. These two bands not only exhibit hyperbolic behavior, but the crystal axis featuring negative real permittivity is inverted, thus the lower and upper bands offer Type-I ($\mathrm{Re}(\epsilon_t) > 0$ and $\mathrm{Re}(\epsilon_z) < 0$ in $760 < f < 825$ cm$^{-1}$) and Type-II ($\mathrm{Re}\ (\epsilon_t) < 0$ and $\mathrm{Re}(\epsilon_z) > 0$ in $1360 < f < 1610$ cm$^{-1}$) hyperbolic

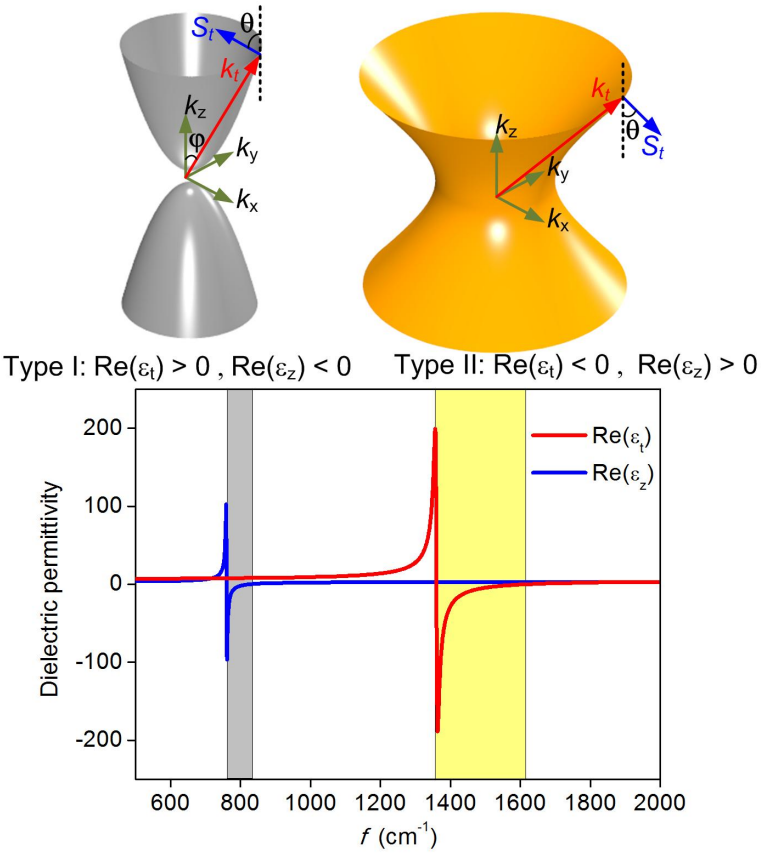


FIGURE 7.1: Hyperbolic dispersion in a hBN layer. Top, two types of hyperbolic dispersions (the Type I for $\mathrm{Re}(\epsilon_t) > 0$ and $\mathrm{Re}(\epsilon_z) < 0$ and the Type II for $\mathrm{Re}(\epsilon_t) < 0$ and $\mathrm{Re}(\epsilon_z) > 0$) and their corresponding vector diagrams. $\varphi$ is the angle between the wavevector $\mathbf{k_t}$ and $z$ axis. $\theta$ is the angle between the Poynting vector $\mathbf{S_t}$ and $z$ axis. For large wavevectors ($k_x \gg k_0$, $k_0 = 2\pi/\lambda$), $\varphi + \theta \approx \pi/2$. Bottom, in-plane and out-plane dielectric permittivities ($\epsilon_t$ , $\epsilon_z$) of hBN, taken from the ref.[43]. Two hyperbolic regions are marked in gray and yellow, respectively.

response, respectively. The inversion of the signs of the dielectric function results in novel behavior, such as a negative (positive) z-component of the group velocity in the upper (lower) Reststrahlen bands. This results in unique phenomenon such as higher order resonance modes occurring at lower (higher) frequency.

Until now, due to a lack of a homogeneous material exhibiting both types of hyperbolicity, a comprehensive study of the impact of these two unique regimes for nanoimaging and super-resolution focusing has not been experimentally probed. Caldwell *et al.* have provided an experimental study comparing the unique behaviors of these two regimes, albeit within the context of three-dimensionally confined cavities. In addition to providing a homogeneous medium exhibiting both Type

I and II hyperbolicity, hBN also exhibits much lower losses (higher efficiencies) than plasmonic materials, i.e., $\mathrm{Im}(\epsilon_t) \sim 0.1$ for $\mathrm{Re}(\epsilon_t) = -1$ at $f = 1573$ cm$^{-1}$ and $\mathrm{Im}(\epsilon_z) \sim 0.1$ for $\mathrm{Re}(\epsilon_z) = -1$ at $f = 809$ cm$^{-1}$. This is crucial for realizing extended propagation and detection of high-k polariton modes (deeply sub-diffractional confinement) [42, 43, 59].

## 7.2 Theory and simulations

The dielectric permittivities are also highly dispersive in these two regions, giving rise to a frequency-dependent ratio between $\epsilon_t$ and $\epsilon_z$. Thus, because of the presence of both Type I and II hyperbolicity, from Eq. 7.1 I can predict that the propagation angle $\theta$ will be an increasing (decreasing) function of the frequency in the lower (upper) Reststrahlen bands. As shown in Fig. 7.2a, as the frequency is increased, $\theta$ increases from about 16° to 87° ($\Delta\theta \approx 71^o$) within the Type I lower Reststrahlen band, while it decreases from $\theta \approx 83°$ to $\theta \approx 2°$($\Delta\theta \approx 81°$) in the Type II upper Reststrahlen band (Fig. 7.2b). Here, I experimentally verify this inversion of the propagation angle within the two spectral bands, providing near-field imaging of sub-diffractional objects under a thin slab of hBN. This investigation also enabled the experimental demonstration of the unusual imaging properties of both Type I and II hyperbolic media, thereby providing the physical description necessary to realize and optimize near-field imaging using natural hyperbolic materials.

This frequency-dependent tuning of the angular hyperbolic-polariton propagation in hBN and the suitability of this material for near-field imaging can be easily quantified and visualized via two-dimensional (2D) numerical calculations. For this, I consider a 0.3-$\mu$m wide gold stripe on a Si substrate with an hBN cover layer (the thickness h = 1 $\mu$m) illuminated by a $p$-polarized plane wave incident from the top. Simulated electric-field distributions ($|E_z|$) at six typical operation frequencies are presented in Fig. 7.2c- h, and demonstrate the directional nature of the hyperbolic polaritons. Here the high-k fields scattered from the edges of the embedded gold stripe are induced to propagate within the hBN flake (as marked in Fig. 7.2d), with the angle of propagation being directly dependent upon the frequency of operation. As stated previously [32], in the absence of the hyperbolic dispersion, such high-k modes would be evanescent (i.e. decay rapidly) within the medium. Each edge of the Au stripe excites two sub-diffractional hyperbolic

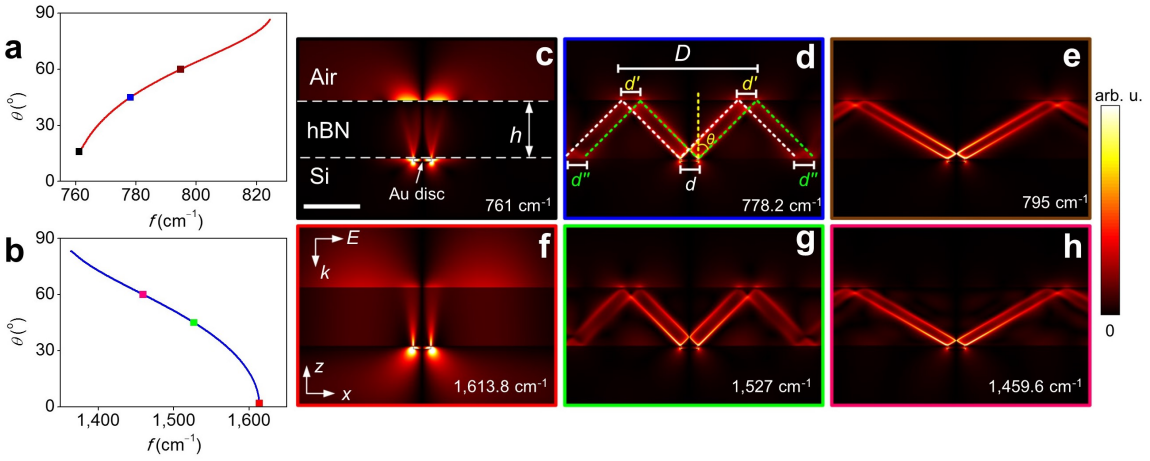


FIGURE 7.2: Frequency-dependent directional angles of the hyperbolic polaritons propagating inside the hBN. Solid lines in (a) and (b), the critical angle $\theta$ of the hyperbolic polaritons as a function of the frequency $f$ in the Type-I ($760 < f < 825$ cm$^{-1}$, $\epsilon_t > 0$ and $\epsilon_z < 0$) and Type-II ($1360 < f < 1610$cm$^{-1}$, $\epsilon_t < 0$ and $\epsilon_z > 0$) hyperbolic bands of the hBN. c-h, Simulated electric-field distribution ($|E_z|$) at various frequencies. The directional angles evaluated from these simulations are plotted in (a) and (b) (color dots) for comparison: $\theta = 16°$ ((c) at $f = 761$ cm$^{-1}$), $\theta = 2°$ ((f) at $f = 1613.8$ cm$^{-1}$), $\theta = 45°$ ((d) and (g), at $f = 778.2$ cm$^{-1}$ and $f = 1527$ cm$^{-1}$) and $\theta = 60°$((e) and (h), at $f = 795$ cm$^{-1}$ and $f = 1459.6$ cm$^{-1}$). The scale bar in (c) indicates 1 $\mu$m.

polaritons that propagate at the angles $+/-\theta$. This frequency dependent propagation angle (indicated by color dots in Fig. 7.2a and b) quantitatively agrees with the analytical predictions based on Eq. 7.1 (see solid lines in Fig. 7.2a and b), therefore the propagation angle can be predicted via the simple ratio of the extraordinary ($z$-axis) and ordinary ($x$-$y$ plane) components of the anisotropic dielectric function of hBN.

The anticipated super-resolution imaging performance of the hBN slab is directly tied to the propagation angle, as demonstrated in Fig. 7.2c-h, which as noted above is directly dependent upon the type of hyperbolicity. For instance, at wavelengths with very low propagation angles ( Fig. 7.2c and f), the image of the sub-diffraction Au stripe is nearly perfectly restored on the top surface of the hBN, similar to near-field superlensing [10, 22, 24]. Namely, the restored width $d$' is nearly identical to the actual width $d$ of the investigated stripe (e.g. $d' \approx 309$ nm, around $\lambda/40$-resolution at $f = 778.2$ cm$^{-1}$ or $\lambda = 12.85$ $\mu$m). However, as the angle is increased ( Fig. 7.2d, e for the lower and g, h for the upper Reststrahlen bands), an enlarged outline of the object image is obtained with the width $D(f) = d + 2h\ \tan\theta(f)$.

Note that due to the inversion of the dependence of $\theta$ on between the two spectral bands, superlensing-type response is observed at low and high frequencies within the lower and upper Reststrahlen bands, respectively, while the enlarged imaging behavior is observed at high and low frequencies.

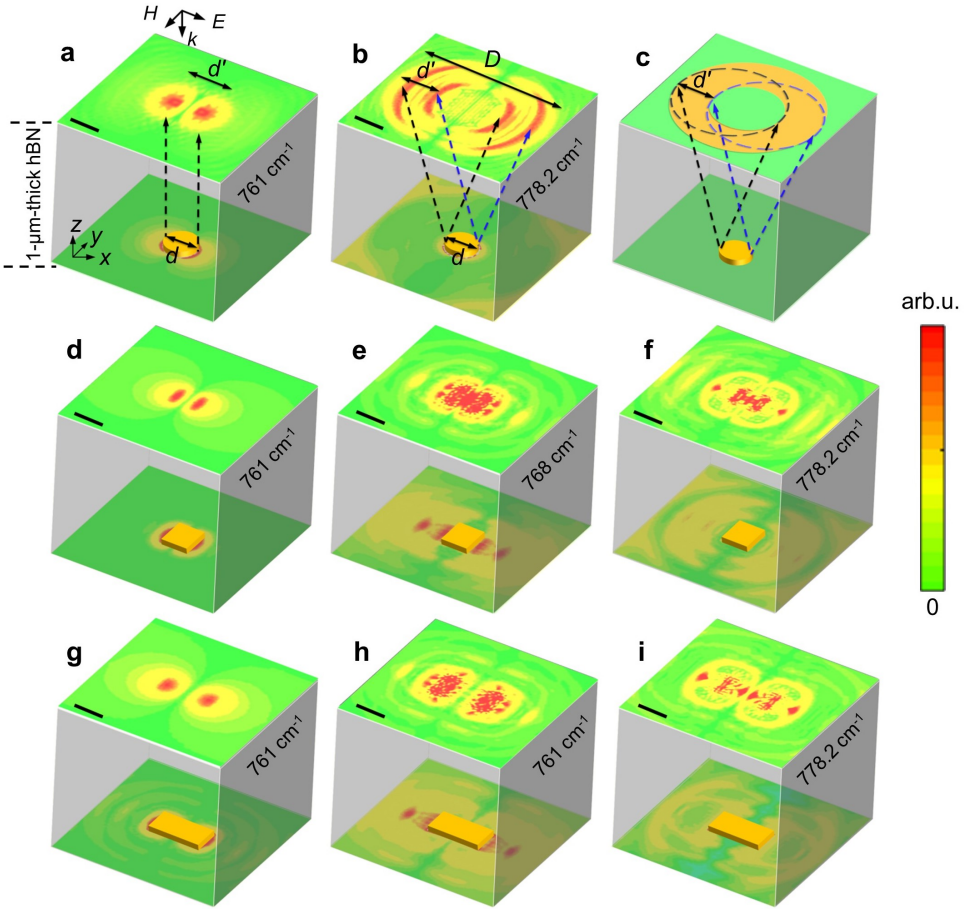


FIGURE 7.3: Three dimensional simulations of imaging different structures through the hBN layer. (a) and (b): 3D simulations of imaging a gold disc (0.6-$\mu$m diameter) below the 1-$\mu$m-thick hBN layer (scale bars, 0.6 $\mu$m). Simulated electric-field distributions ($|E_z|$) taken at top and bottom surface of the hBN layer for imaging, (a) at $f = 761$ cm$^{-1}$. (b) at $f = 778.2$ cm$^{-1}$ show the frequency-dependent transition between perfect imaging and enlarged imaging. (c) the sketch of the mechanism of the enlargement observed in (b). (In this sketch I do not consider the influence of the illumination polarization). (d-f) $|E_z|$-distributions of imaging a gold square (1-$\mu$m length, 50-nm height). (g-i) $|E_z|$-distributions of imaging a gold bar (1-$\mu$m width, 2-$\mu$m length, 50-nm height). All these images show the frequency-dependent transition between perfect imaging and enlarged imaging of the geometric outline of the structures. scale bars, 1.2 $\mu$m. The z-axis in all the images is not to scale for better visualization.

This novel enlargement can be clearly observed in the more practical three-dimensional (3D) cases. As shown in Fig. 7.3a, the 0.6-$\mu$m-diameter gold disc is once again restored at very shallow angles; however, at larger propagation angles a double concentric ring-like field distribution is recorded in the near-field (Fig. 7.3b), rather than a direct replication of the original field distribution of the object. This enlarged pattern results from the frequency-dependent propagation angle of the hyperbolic polaritons (the polariton fields forming a cone, as sketched in Fig. 7.3c). This novel phenomenon is also found for other shapes (like a Au square and stripe) as shown in Fig. 7.3d- i. Intriguingly, the trace of the hyperbolic-polariton cones reconstructs the enlarged and slightly distorted pattern that is still able to identify the outline (shape) information of the object. Quantitatively, through recording the hyperbolic-polariton-reconstructed outline ($D(f)$), I can extract the geometric size and shape from the strict relationship of $D(f) = d + 2h\tan\theta(f)$. These results suggest a new hyperbolic-polariton-based imaging scenario, which will be verified and visualized by our experiments below.

## 7.3 Experiments of near-field imaging through hBN

### 7.3.1 Experimental results in Type I hyperbolic band

The predicted imaging mechanism is verified by our experiments first in the Type I hyperbolic band, as presented in Fig. 7.4. A schematic of the experimental setup is provided in Fig. 7.4a where the images restored by the hBN layer are recorded using a scattering-type scanning near-field optical microscope (s-SNOM). I use a 0.15-$\mu$m-thick exfoliated hBN flake to image the underlying, 30 nm tall, gold nanodiscs with 0.3-$\mu$m diameter and 1.3-$\mu$m center-to-center separation. The metallic tip of the s-SNOM is illuminated by a home-built, tunable broadband infrared laser [66, 67] with the peak position of the laser spectrum (inset in Fig. 7.4a) matched to the lower, Type-I hyperbolic region of hBN (760 cm$^{-1}$ $< f <$825 cm$^{-1}$). Both the optical and topographic information at the top surface of the hBN layer are collected simultaneously (c.f. Chapter 3). In the obtained topographic image ( Fig. 7.4b), the gold discs are masked by the covering hBN layer,

[1]The broadband measurement was performed with the help of Martin Lewin and Fabian Gaussmann at the ILT.

while in the broadband-SNOM image ( Fig. 7.4c), all three nanodiscs are clearly resolved with bright contrast (i.e. high signal-to-background ratio). To ensure that the imaging is indeed due to the hyperbolic nature of the hBN slab, a control image was also collected at a frequency outside of the lower Reststrahlen band using a $CO_2$ laser at $f = 952$ cm$^{-1}$, where both components of the dielectric function are positive ($\mathrm{Re}(\epsilon_t) = 8.8$ and $\mathrm{Re}(\epsilon_z) = 2$). As shown in Fig. 7.4e, in contrast to the hyperbolic case, only weak features of the discs are observed through the thin hBN layer in the control experiment. This is further demonstrated by the line profiles taken across the two discs for both cases presented in Fig. 7.4f, with a dramatic enhancement in the imaging efficiency observed in the hyperbolic regime. Such an effect would be further amplified within thick hBN slabs, whereby any structural morphology would be totally lost, but the near-field imaging properties retained. The hyperbolic images also provided a narrower FWHM (full width at half maximum) of about 0.5 $\mu$m in addition to the dramatically improved contrast (signal-to-background ratio). Considering the resolved deeply subwavelength optical FWHM ($\sim \lambda/24$), this comparison clearly confirms the improved near-field imaging by the hBN layer.

Although the broadband s-SNOM image shown in Fig. 7.4c is able to resolve the discs, it does not reflect the actual field distribution of the image due to its detection scheme [67]. Because of the broadband light source used, the detection is not monochromatic as in the simulations presented in Fig. 7.2 and 7.3. Instead, the collected images are the superposition of all the different frequency components of the broadband laser and therefore the concentric-ring field distributions are not directly observed. Further, depending on the chosen interference phase difference (constructive or destructive phases, involving the position of a reference mirror in our setup), it can also show reversed imaging contrasts (see ref. [67]). Therefore, the broadband s-SNOM image alone cannot directly reveal the actual image of the field distributions of the discs and the frequency dependence of the hBN layer. For this, monochromatic s-SNOM images would be required; however, currently such sources are not readily available within this spectral range.

To determine the actual imaging response through the hBN layer at each individual wavelength, I performed Fourier transform infrared nanospectroscopy (nano-FTIR) [42, 67] along a line scan (dashed line in Fig. 7.4c) across two discs. At each pixel, nano-FTIR delivers a full infrared spectrum recorded at the spatial resolution of the probing tip (less than 50 nm). Thus the s-SNOM signals $s_2(f, x)$

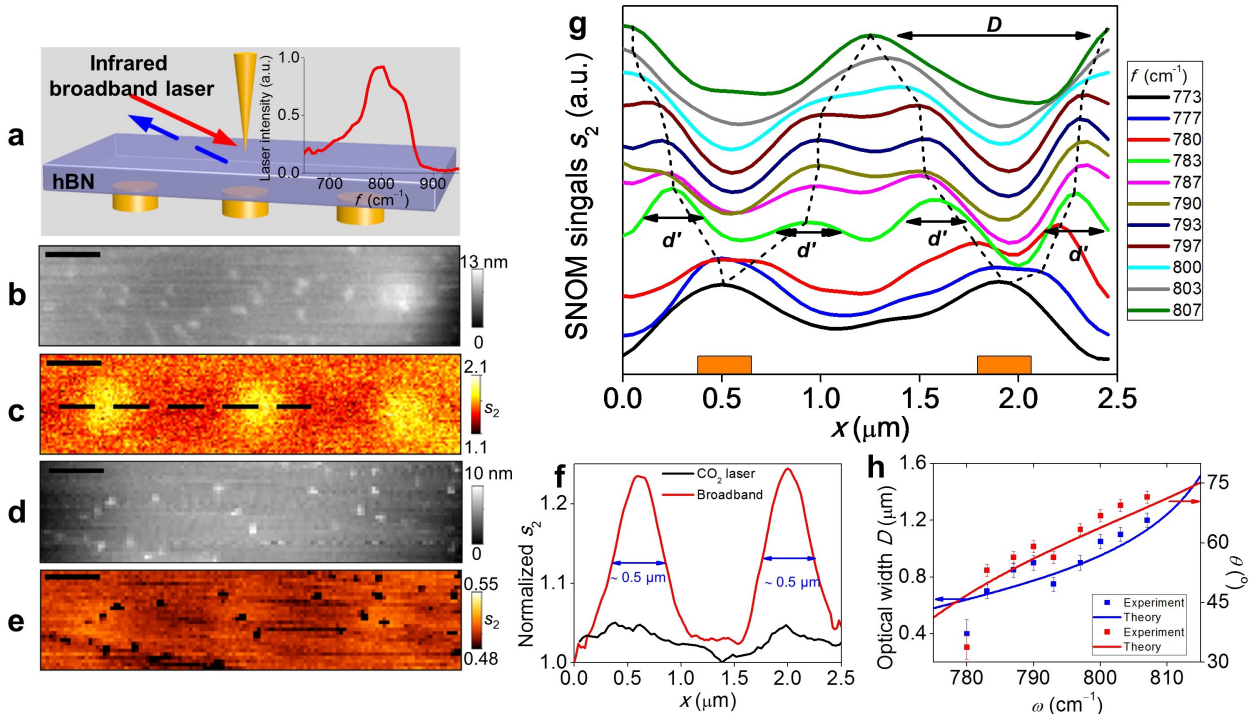


FIGURE 7.4: Experimental demonstration of super-resolution imaging with tunable hyperbolic polaritons in the Type I band. (a) Sketch of the experimental set-up. The right inset is the normalized laser spectrum of the used mid-infrared broadband laser. (b) The AFM topography taken at the top surface of the 0.15-$\mu$m-thick hBN hyperlens. (c) The 2D infrared optical images taken with the broadband laser. (e) The control infrared image taken with a $CO_2$ laser at $f$ = 952 cm$^{-1}$ that is out of the hyperbolic region of the hBN. The small black dots in the image are caused from topographic features (corresponding topographic image shown in (d)). Scale bars: 0.5 $\mu$m. (f) Detailed profiles of the s-SNOM signals across two neighbouring discs (along the line marked in (e), averaged over 5 scan lines) for the cases using the broadband laser (red line) and the $CO_2$ laser (black line), respectively. Both profiles are normalized to their respective minimum values outside the discs. The broadband imaging shows much stronger contrasts for the discs. (g) Detailed Nano-FTIR line profiles at various frequencies. Dashed line marks the position variations of the peak of edge-launched hyperbolic polaritons. (h) Optical widths and corresponding directional angles of the hyperbolic polaritons evaluated from the experimental results (dots) in comparison with the calculated results (solid lines). The error bars result from the spatial pixel size (50 nm) in nano-FTIR measurements.

as a function of the frequency $f$ and the spatial position $x$ are obtained [42, 67]. This hyperspectral imaging approach allows the extraction of detailed spatial line profiles at various frequencies as shown in Fig. 7.4g. For frequencies within the lower Reststrahlen band but $f > 780$ cm$^{-1}$, two peaks are observed for each disc (see the typical case at $f = 783$ cm$^{-1}$). These peaks (with the width $d' \approx 0.3$ $\mu$m) correspond to the edge-excited hyperbolic polaritons. The distance D between the two edge-launched peaks increases from about 0.4 $\mu$m to approximately 1.25 $\mu$m (for the right disc) when changing the frequency from 780 cm$^{-1}$ to 807 cm$^{-1}$ , with this distance being directly related to the frequency-dependent hyperbolic-polariton propagation angle. At frequencies $f < 780$ cm$^{-1}$, the two edge-launched peaks are not resolved by the hBN layer due to the very small directional angle of hyperbolic polaritons, leading to one single broad peak observed for each disc. Based on the smallest peak-to-peak separation $D$ in our results being approximately 0.4 $\mu$m at $f = 780$ cm$^{-1}$ ($\lambda = 12.8$ $\mu$m), this corresponds to a sub-diffractional resolution (defined by the wavelength over the peak-to-peak separation) of about $\lambda/32$.

For the comparison of the theoretically predicted propagation angles ( Fig. 7.2a) and those experimentally derived from the s-SNOM measurements, I plot the experimentally determined $D$ (blue curve and data) and corresponding directional angles $\theta$ (red curve and data) of the hyperbolic polaritons as functions of $f$ in Fig. 7.4h. The theoretical result [from $D(f) = d + 2h\tan\theta(f)$] is also shown for comparison. Good quantitative agreement is found between the experiments and theory. This verifies the predicted tuning range of the propagation angle of the hyperbolic polaritons to be about $35° - 70°$ and the tunable ratio ($D/d$) to range from 1.39 to 4.2. However, certain discrepancies are still found in this comparison, and I do not observe multiple peaks originating from the multi-reflection of the hyperbolic polaritons within the hBN slab. This may be because a higher hBN damping in this band.

### 7.3.2 Experimental results in Type II hyperbolic band

In order to extract the near-field frequency-dependent imaging and propagation angles, near-field imaging experiments were also performed in the Type II hyperbolic band by using a line-tunable quantum cascade laser (QCL, spanning from

1310 to 1430 $cm^{-1}$). This monochromatic laser allows us to present the hyperbolic-reconstructed imaging phenomenon in a more intuitive way compared to the case with the broadband laser. First, I performed the s-SNOM measurements to image a Au stripe (about 1 $\mu$m long, 100 nm wide, as sketched in Fig. 7.5a) that is covered by the 0.15-$\mu$m hBN layer (AFM topography in Fig. 7.5b). In comparison to the circular discs, this rectangular object can avoid the potential confusion caused by the cones of hyperbolic polaritons (circular cross section) for understanding the imaging results. Because the deeply sub-diffractional width ($\sim \lambda/70$) of the stripe, optical information cannot be recorded at frequencies outside the hyperbolic band, as shown in Fig. 7.5c. In contrast, I clearly observe enlarged optical

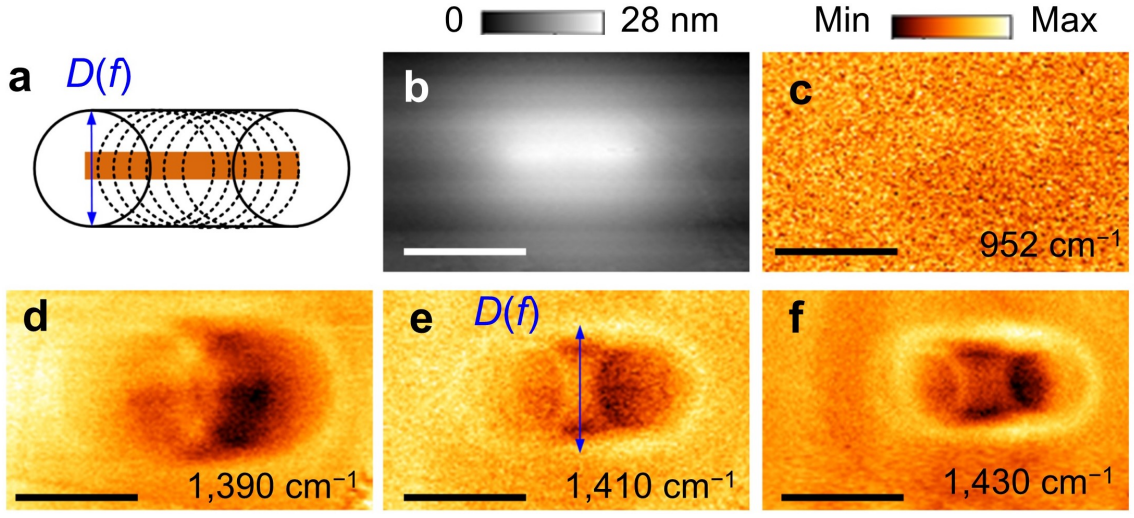


FIGURE 7.5: Experimental demonstration of enlarged imaging of a Au stripe with tunable hyperbolic polaritons in the Type II band. (a) Sketch of the imaged object - a Au stripe (not to scale), located below the 0.15 $\mu$m thick hBN flake. The length $l$ of the stripe is about 1 $\mu$m, and the width $w$ is around 0.1 $\mu$m. The dashed rings result from launched hyperbolic polaritons from the edges of the stripe. These hyperbolic polaritons form an enlarged outline that reveals the object information. (b) AFM topography taken from the hBN top surface. (c) The s-SNOM image taken at $f = 952$ $cm^{-1}$ outside the hyperbolic band. No optical feature is observed from the underlying structure. (d - f) Spectroscopic imaging the stripe in the Type II hyperbolic band. The bright outlines found in the images are formed by the hyperbolic-polariton cones, which are enlarged compared to the original structure. From the measured $D(\omega)$, I can estimate the width $w$ of the stripe (using the relationship $D(f) = w+2h\tan\theta(f)$) is about 0.12 $\mu$m, and the estimated length is about 1.1 $\mu$m. These results verify that from imaging the enlarged outline, it is able to reveal the object information due to the frequency-dependent directivity of hyperbolic polaritons. The scale bars indicate 1 $\mu$m.

patterns formed by the hyperbolic polaritons (Fig. 7.5d-f). Qualitatively, these elliptical, rectangular patterns carry and reflect the shape information of the original object. Quantitatively, from the measured width and length of the patterns, in conjunction with the known propagation angle of the hyperbolic polaritons, I can extract the geometric size of the investigated object. Using this approach, I estimate the width of the stripe is about 0.12 $\mu$m, and the estimated length is about 1.1 $\mu$m, which is consistent with SEM measurements of the stripe prior to hBN exfoliation. I note that for the cases at the frequencies where hyperbolic polaritons have smaller diffractional angles (namely, the hyperbolic-polariton cone with the very small diameter), the reconstructed image will be similar to the one-to-one near-field superlensing [10, 22, 24]. Therefore, in such hyperbolic-polariton-based imaging phenomenon, it has two frequency-dependent operation modes: the enlarged reconstruction and the one-to-one superlensing.

As previously discussed, I also experimentally demonstrated that the diameter of the hyperbolic-polariton cone increases with decreasing frequency, which is inverted with respect to the Type I band. These two distinct frequency dependences, found in two spectral regimes through imaging of the sub-diffractional objects, verify again that the two types of hyperbolic dispersion easily exist in the hBN crystal, without the need for fabricating different HMM structures.

In addition to the single structure, I also investigated periodic arrays of nanostructures. I imaged the arrays of the Au nanodiscs (5 $\times$ 5 array, sketched in Fig. 7.6a) with different separations. The diameter of the discs was fixed at 0.3 $\mu$m. The gap separation between two discs varied from g = 0.1 $\mu$m to g = 1 $\mu$m. The experimental results are shown in Fig. 7.6d- f. I observed the complicated overlapping of the hyperbolic-polariton cone launched by each disc. However, with these sub-diffractional hyperbolic polaritons, I have the opportunity to distinguish the deeply sub-diffractional structures that are not readily seen in either AFM topography or near-field imaging at frequencies outside of the hyperbolic regime (see the comparison of Fig. 7.6b-d).

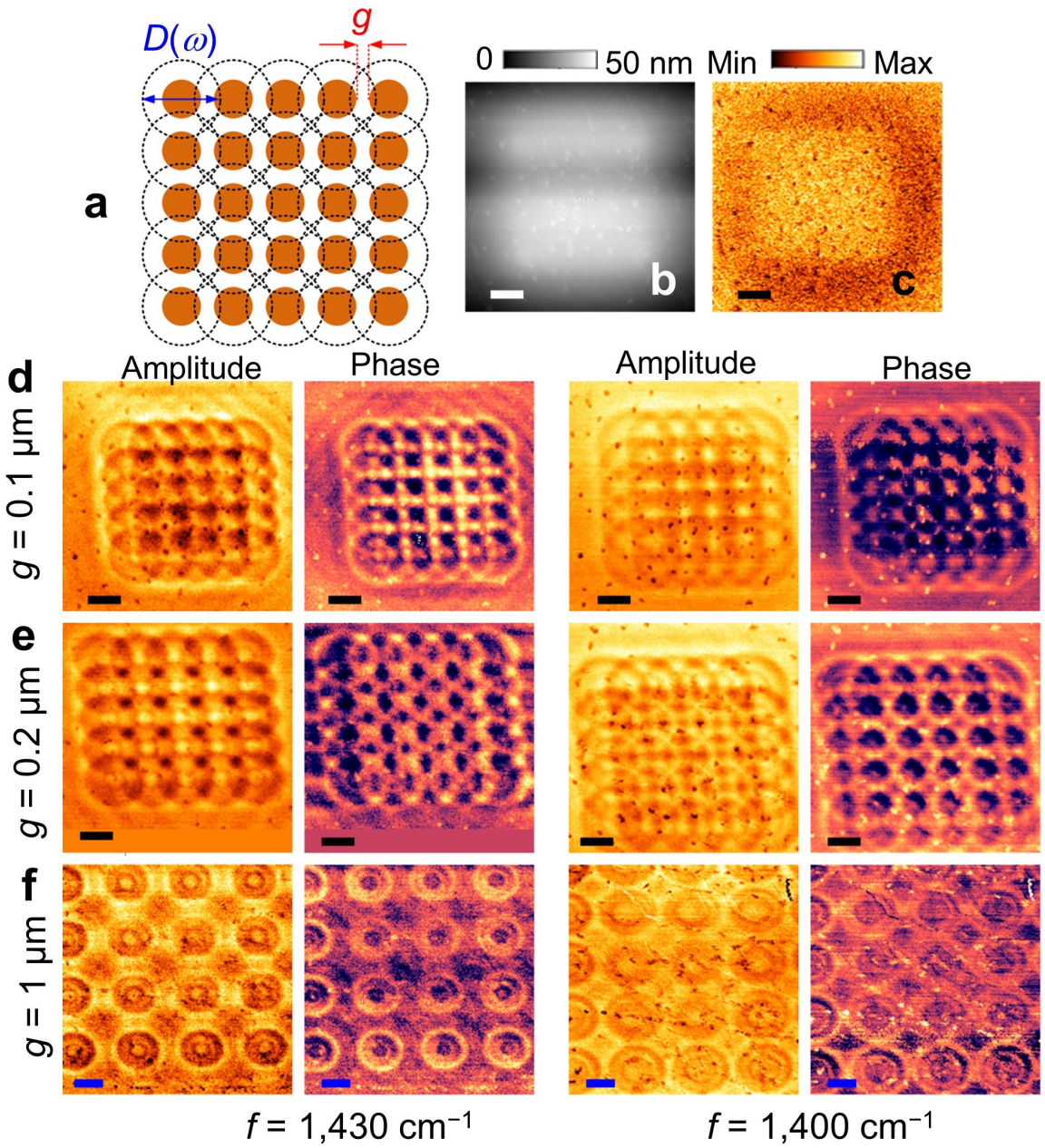


FIGURE 7.6: Experiments of imaging the arrays of Au nanodiscs with hyperbolic polaritons in the Type II band. (a) Sketch of the arrays of the Au nanodiscs. The diameter of the discs is fixed to be 300 nm. The gap separation between two discs varies from g = 0.1 $\mu$m to g = 1 $\mu$m. The dashed rings indicate the launched hyperbolic polaritons. (b) the AFM topography of the array with g = 0.1 $\mu$m, taken from the hBN top surface. (c) the s-SNOM image of the array with g = 0.1 $\mu$m taken at $f$ = 952 cm$^{-1}$ outside the hyperbolic band. No detailed optical feature is probed for resolving the structure. (d)-(f) Near-field images (amplitude and phase) of the arrays at two different frequencies of 1430 cm$^{-1}$ and 1400 cm$^{-1}$ inside the Type II hyperbolic band. Obviously, the launched hyperbolic polaritons help to reveal the single dics in the arrays. In (e), color spaces below the actual images are added in the amplitude and phase images taken at 1430 cm$^{-1}$, for keeping the square shape. All the scale bars indicate 0.5 $\mu$m.

## 7.4 Near-field focusing and waveguiding by hBN

In addition to the already proven high-resolution imaging with tunable enlargement of the outline of sub-diffractional objects using only a simple slab of hBN, the highly directional nature of hyperbolic polaritons can also result in sub-diffractional focusing behavior. When imaging the nanodiscs with a large diameter of 0.75 $\mu$m, I observe the focusing spot with the width of about 0.175 $\mu$m ($\sim \lambda/40$) at $f = 1420$ cm$^{-1}$ (see Fig. 7.7). This is because all the hyperbolic-polariton cones launched by the nanodisc superimpose into the center point, leading to the concentration of the light. I also investigate this focusing effect with the broadband laser in the Type I hyperbolic band. However, the obtained results are also the superposition of all the frequency components, which are not intuitive. I also note that this super-focusing effect is independently shown and discussed in Ref. [81], which was performed concurrently with the work discussed here. Both

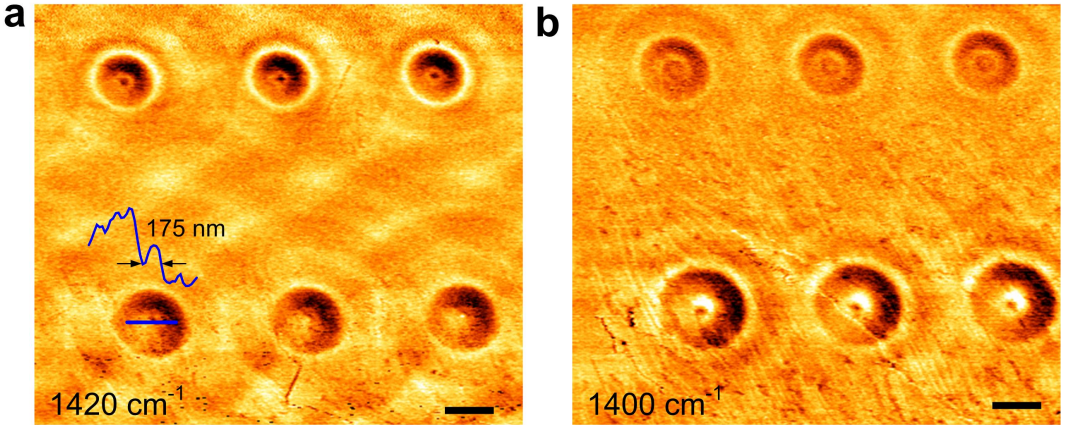


FIGURE 7.7: Experimental demonstration of near-field optical focusing and waveguiding of hyperbolic polaritons. Near-field images of the nanodiscs (top three with diameter 500 nm, bottom three with diameter 750 nm): (a) at 1420 cm$^{-1}$, (b) at 1400 cm$^{-1}$. Clear focusing and interference of hyperbolic polaritons are found. The scale bars indicate 1000 nm. From the line profile across the focusing spot (shown in a, along the blue line), a width of about 175 nm ($\sim \lambda/40$) of the spot are obtained.

the enlarged imaging and the super-focusing are based on the volume-confined, frequency-dependent propagation angle of hyperbolic polaritons in hBN. I can envision other potential disruptive technologies based on the great potential of

the highly directional hyperbolic polaritons. First, this frequency-selective waveguiding could be useful for photonic switching or computing, infrared filtering, or various other nanophotonic applications. Figure 6.8a shows numerical simulations of hyperbolic polaritons propagating inside an hBN waveguide structure (a horizontal hBN-layer connected with three vertical hBN-channels) at a frequency of $f = 762$ cm$^{-1}$. Due to the small propagation angle, the electromagnetic fields

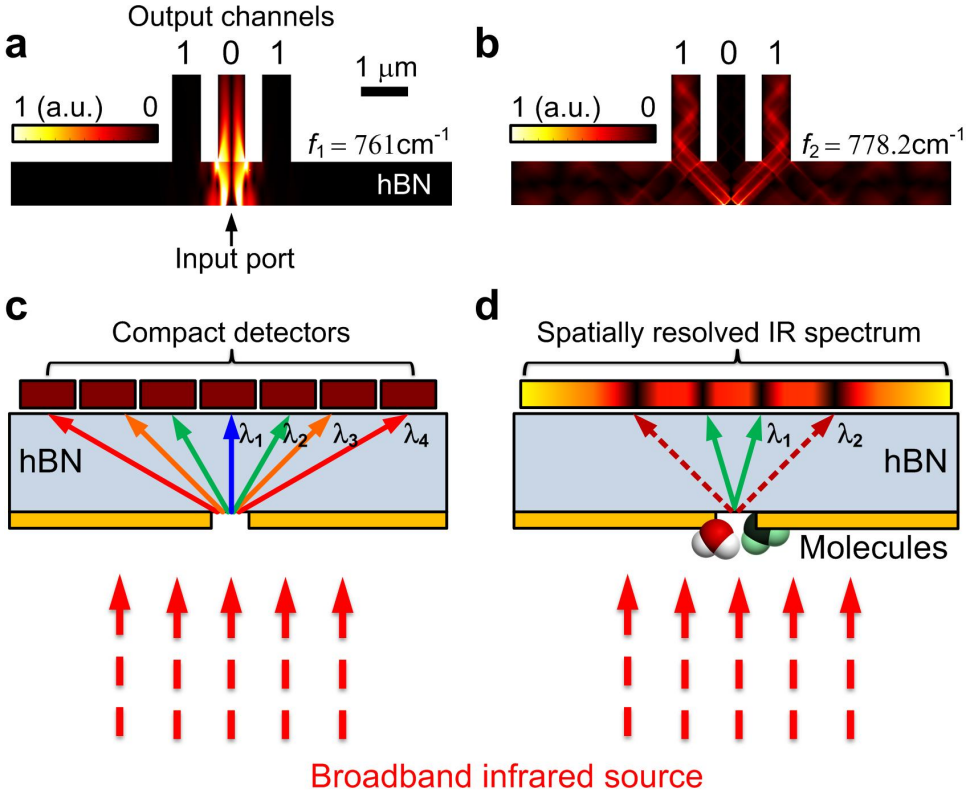


FIGURE 7.8: Further application proposals using the tunable highly directional hyperbolic polaritons. Simulated $|E_z|$-distributions inside an hBN waveguiding structure (a) at $f = 761$ cm$^{-1}$ , (b) at $f = 778.2$ cm$^{-1}$. (c), Sketches of an ultra-compact hBN-based infrared spectrometer. The thin hBN layer allows spatially splitting different wavelength components of the incoming infrared illumination. (d), Sketches of hBN-based spatially-resolved infrared spectroscopy for different molecules. The dark colors in the spectrum represent the absorption by the molecules (sketch).

primarily propagate into the inner '0'-channel. When tuning the frequency to $f = 778.2$ cm$^{-1}$ ( Fig. 7.8b), the fields propagate with an angle of $\sim 45°$ and therefore transmit into the two outer '1'-channels. More complicated geometries could also expand such approaches beyond a binary routing into more sophisticated multi-channel systems. Consequently, this frequency-selective waveguiding

could be useful for photonic switching or computing, infrared filtering, or various other nanophotonic applications.

Another potential application is realized in the form of an ultra-compact subwavelength spectrometer. As sketched in Fig. 7.8c, a natural hBN layer should allow for the spatial separation or filtering of incoming broadband light into different wavelength channels, which could then be detected by subwavelength infrared detector pixels. This particular spectrometer configuration could also be used for chemical and biological samples, in the form of spatially-resolved infrared spectroscopy. Under broadband mid-infrared illumination the hyperbolic polaritons could carry the vibration (or absorption) information of molecules in contact with the surface (Fig. 7.8d), dispersing the spectral information at different angles, enabling them to be spatially resolved by a near-field intensity detector (like the s-SNOM tip) without the need of spectrometers.

## 7.5 Conclusion

I demonstrate the complete hyperbolic imaging response of hBN and its potential for improving the near-field imaging of deeply embedded objects [82, 85] in both the Type I lower and Type II upper Reststrahlen bands, respectively. More specifically, I reveal the hyperbolic nature of the hBN layer for near-field waveguiding, imaging, focusing and its dependence upon the operational frequency. Although all our results are restricted in the near field, I also expect that these novel findings will benefit far-field imaging by introducing specific geometric designs, such as circular or wedge-shaped hyperlenses [33–35]. Furthermore, as a van der Waal's crystal [153], hBN lends itself to incorporation on non-planar and flexible substrates more amenable to true hyperlensing methodologies [33–35]. The realization of a naturally occurring, Type I and II hyperbolic media enable new opportunities for nanophotonics that go beyond sub-diffractional near-field imaging and potential hyperlensing. Due to the similar material anisotropy present in other polar dielectric van der Waals crystals [153], such as $MoS_2$ or $WS_2$, the natural hyperbolic response of hBN may be generalized to the entire class of polar two-dimensional crystals, thus expanding the potential spectral range of this behavior from the mid-infrared into the single digit THz spectral region [44, 53].

# 8 Summary and outlook

## 8.1 Summary

In conclusion, an in-depth understanding of the basic imaging mechanism of the superlens has been given in this thesis. This is on basis of the experiment of real-space imaging of sub-diffractional SPhP modes in the SiC superlens. From the determined dispersion relation of the superlens, I have demonstrated that the ultra-confined surface polariton modes in the superlens offer the enhancement of evanescent fields, reconstructing a high-resolution image of the investigated object.

Furthermore, I have succeeded in using the SiC superlens to image dielectric objects. The obtained spectroscopic imaging data for the first time have demonstrated that the superlens can be used for identifying the dielectric information of the imaged objects. This finding will open up great opportunities for abundant biological and chemical applications.

The superlens can only work in a narrow working wavelength range. This narrow bandwidth limits the superlens on applications of broadband infrared spectroscopy and microscopy. In order to overcome this limitation, in this thesis I have introduced two new superlens designs. First, I have theoretically proposed a multilayered polar-dielectric superlens system capable of achieving sub-diffraction limited imaging simultaneously at multiple wavelengths. My theory and simulation results have verified that the proposed multilayered superlens can fulfill the superlensing condition at different wavelengths. The number of superlensing wavelengths of the lens can be tuned by controlling the number of polar dielectrics. Ideally, by suitably choosing polar dielectrics, our lens can cover the wavelengths ranging from infrared to THz frequencies.

Another idea of extending the working wavelength range of the superlens is to use the graphene lens. Due to the non-resonant enhancement provided by graphene plasmons, the graphene lens yields new promising properties including broad intrinsic bandwidth and low sensitivity to loss, together with a good spatial resolution of around $\lambda/7$ for a bilayer case and over $\lambda/10$ for the multilayered configuration. Most importantly, due to the large tunability of the graphene, the proposed graphene lens can act as an ultrabroadband sub-diffraction-limited imaging device to in principle cover the nearly whole range from mid-infrared to THz frequencies.

In addition to the theory of the graphene lens, the first proof of concept experiment has been also shown. I have demonstrated that a monolayer graphene can offer a 7-fold enhancement of evanescent information, improving conventional infrared near-field microscopy to resolve buried structures at a 500-nm depth with $\lambda/11$-resolution.

Moreover, experiments of near-field optical imaging through a natural hyperbolic material- hBN, have been presented. I have shown that the flat hBN layer can work as a natural hyperlens exhibiting wavelength-dependent multifunctional operations. It can offer both an enhanced near-field imaging of single buried objects with down to $\lambda/32$ resolution (0.4 $\mu$m at $\sim$ 12.8 $\mu$m) and an enlarged reconstruction of the geometric outline of the investigated objects. Both the excellent resolution and the multifunctional operation can be explained based on the volume-confined, wavelength dependent propagation angle of two types of hyperbolic phonon polaritons.

I hope the results presented in this thesis will be useful for realizing superlens-based high-resolution infrared microscopy and spectroscopy.

## 8.2 Outlook

In the Outlook, I will discuss several remained problems, open questions and prospects after the thesis.

**Imaging using an ultrafast infrared broadband Laser**. In Section 4.1, the dispersion relation of SPhPs in the SiC superlens has been mapped by using the line-tunable monochromatic infrared laser. The whole experiments are time-consuming, because they require a series of monochromatic images (or scans) taken at multiple wavelengths. Additionally, the used $CO_2$-laser also has wavelength band gaps in the wavelength range of our interests, which cannot offer the possibility of recording the complete dispersion relation of the superlens. The measurement with a broadband laser covering the whole spectrum of the SiC superlens is able to determine the complete dispersion relation of the SPhPs in only one line scan.[1]

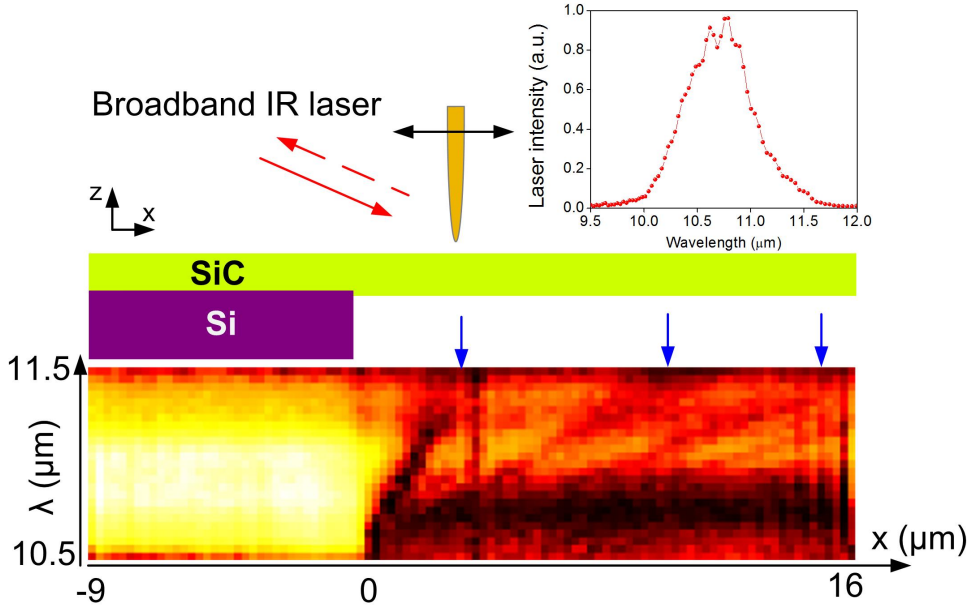


FIGURE 8.1: Top, sketch of the set-up of the broadband S-SNOM imaging of the Si edge through the 500-nm-thick SiC superlens. Right insert, the laser spectrum of the broadband laser. Bottom, the obtained map $s_2(\lambda, x)$ of the line scan across the underlying edge. Blue arrows mark the resolved minima of the SPhP interference.

[1]The broadband measurement was performed with the help of Dr. Fabian Gaußmann at the ILT.

As sketched in the top of Fig. 8.1, I repeat the measurements shown in Fig. 4.2. In contrast, at this time the s-SNOM is coupled with a broadband, tunable mid-infrared picosecond laser, which is built at the Fraunhofer ILT [66, 67]. The laser spectrum is tuned to cover the SiC-superlens spectrum as shown in the insert. The center wavelength of the laser is about 10.75 $\mu$m. The full bandwidth at half maximum is about 0.7 $\mu$m. I perform a line scan across the Si edge. At each pixel of the scan, I record a Fourier transform spectrum of the broadband s-SNOM signals (see ref. [67]). Therefore after only one line scan I obtain a map of s-SNOM signals $s_2(\lambda, x)$ as a function of wavelength $\lambda$ and the lateral position $x$, which is presented in the bottom of Figure 8.1. In this map I reveal a complete wavelength dependence of the SPhP fringes (indicate by black arrows), which also allows for extracting the dispersion relation of SPhPs in the SiC superlens. This preliminary data indicates that the broadband measurement would be a promising way to quickly determine the superlens dispersion. However, the quality of the data is not convincing, which could be improved in future intensive experiments. Furthermore, the used broadband laser with a 10-picosecond pulse duration could be used for investigating the superlensing effect in the time domain [154].

**Superlens determining absorption information of objects**. In Section 4.2 I have shown that the superlens imaging can be used for probing and identifying the material propensities (dielectric function) of the investigated object. However, in those discussions I neglect the imaginary part of the object dielectric function, which contains the (vibrational) absorption information of the imaged object. According to the findings in near-field vibrational nanoscopy [68, 73], absorption properties of objects can be derived from the phase of probed near fields. Therefore, the absorption of the object could be explored in future works by carefully analysing the phase information of the superlens-recorded images.

**Electric tuning of graphene superlens**. I have proposed the electrically tunable graphene superlens for broadband infrared subwavelength imaging in Section Chapter 6. However, although I have successfully shown the first proof-of-concept experiment, the electric-tuning effect is not achieved so far. Our group is planning to address this together with our collaborators using their well-designed sample layout [155].

**Experimental demonstration of multi-wavelength superlens**. The concept of the multi-wavelength superlens introduced in Chapter 5 could be experimentally realized with the SiC-GaN layers. The dielectric functions of SiC and GaN can

fulfill the superlensing condition at two wavelengths, 10.8 and 16.3 $\mu$m. As shown in the simulations (Fig. 8.2), the SiC-GaN sueprlens well resolves a subwavelength double slit at these two wavelengths. In order to prepare the GaN/SiC sueprlens, the GaN layer is needed to be growth on the SiC/Si substrate [156]. After that, by carefully etching the Si, the desired SiC/GaN superlens will be obtained.

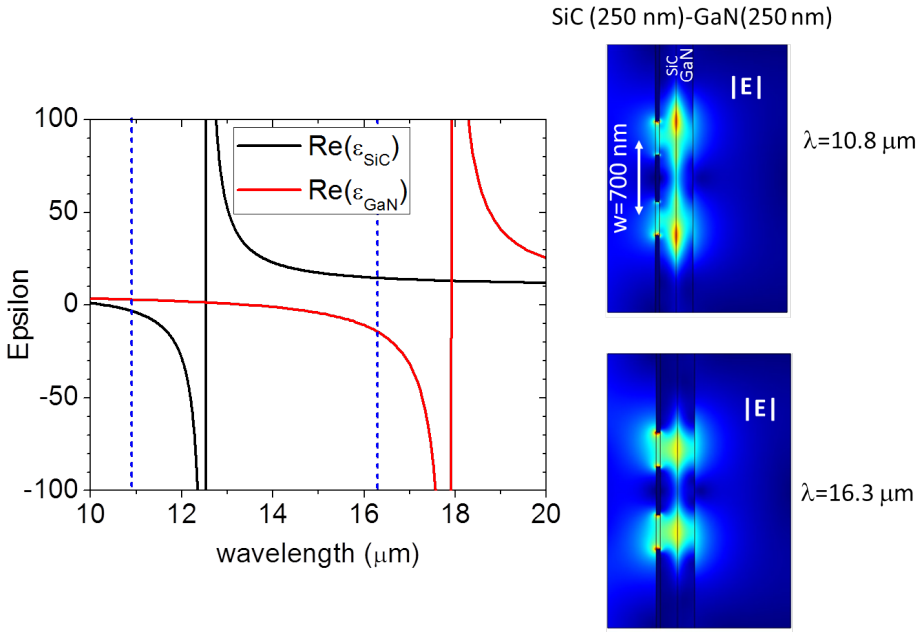


FIGURE 8.2: Left, real parts of dielectric function of SiC and GaN. Two matching wavelengths for the superlensing condition are obtained, 10.8 $\mu$m and 16.3 $\mu$m. Right, Simulated field distribution at the two matching wavelengths. In both cases, the double slit with the 700-nm separation can be resolved by the SiC-GaN sueprlens.

**Far-field hBN hyperlens**. In Chapter 7 I show that the flat hBN layer can work as a natural hyperlens for resolving the subwavelength-sized object. However, the imaging process is still limited in the near field. In order to project the restored image to the far field, a cylindrical or wedge-shape hBN structure [33–35] is needed. Our group is planning to fabricate such structures with the help of our collaborator, Joshua D. Caldwell.

**Phase-change-material switching of the superlens**. Recently, chalcogenide phase change material (PCM) widely used in rewriteable data storage applications is emerging as a promising platform for active nanophotonics [157, 158]. This is on basis of a drastic change in electronic (decreased resistivity by several orders

of magnitude) and optical properties (increased reflectivity, > 30 % in visible spectrum) of the PCMs occurring with a transition of their microscopic structure from a covalently bonded amorphous phase to a resonantly bonded crystalline

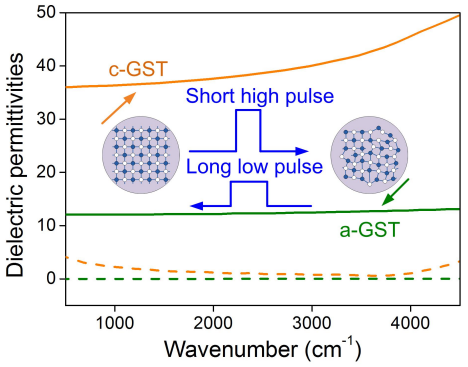


FIGURE 8.3: Real parts of dielectric function of the a-GST and the c-GST, respectively.

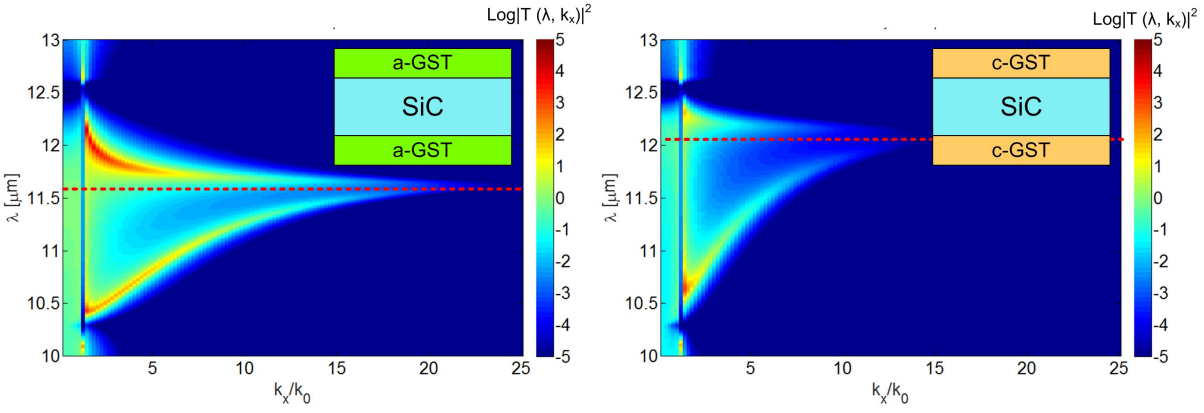


FIGURE 8.4: Calculated transmittance $|T(\lambda, k_x)|^2$ for the superlens under two GST phases. The SiC layer is 300 nm thick. The GST layer is 150 nm.

phase. In particular, these two room-temperature stable phases can be reversibly switched by either optical or electric pulses in very short time (nanosecond scale [159, 160]). Figure 8.3 plots the infrared dielectric function of a representative PCM – Germanium antimony telluride $Ge_3Sb_2Te_6$ (GST) [157, 158]. Both the amorphous (a-) and crystalline (c-) GST exhibit high-index and low-loss infrared dielectric properties ($\varepsilon_{a-GST}$ = 12 + 0.01i, $\varepsilon_{c-GST}$ = 36 + 2.5i) in a wide wavelength range. Very recently, it has been shown that the huge dielectric contrast ($\Delta$ Re($\varepsilon$) = 24) between two GST phases ensures the all-optical, reversible switching of the SPhPs [161]. Therefore, I would expect this material could be used to switch the superlensing wavelength of the superlens. As I calculated the transmission of

the GST/SiC/GST superlens in Fig. 8.4, the phase switching of the GST indeed switches the superlensing wavelength from about 11.6 $\mu$m to 12.1 $\mu$m.

# A Sample preparation

**Sample preparation of SiC-based superlensing.** In the experiment of mapping the dispersion relation of the superlens (Section 4.1), a cubic SiC epitaxial film with the thickness of 500 nm was grown on a Si substrate. By chemically etching an area of underlying Si substrate with the KOH solution, a free-standing SiC window (around 0.3 mm $\times$ 0.3 mm) was obtained. This sample preparation was done by our collaboration group (Prof. Gennady Shvets) in the University of Texas at Austin.

In the experiment of imaging dielecric spheres through the SiC superlens (Section 4.2), commercially available SiC membranes (polycrystalline, 300-nm thick, ordered from NTT-AT) with a large free-standing area (3 mm $\times$ 3 mm) were used for depositing PS and $SiO_2$ sub-micron spheres (from Polyscience). For the experiments shown in Fig. 4.7, PS spheres with two different diameters (0.5 $\pm$ 0.1 $\mu$m and 1 $\pm$ 0.1 $\mu$m) were mixed with a 1:1 concentration ratio in a water solution. The mixed solution was deposited on the backside of the free-standing SiC layer. The whole sample was naturally dried after about one hour. For the experiments shown in Fig. 4.8, $SiO_2$ spheres (diameter: about 0.5-$\mu$m) were deposited onto the backside of the SiC layer, which were mixed with the formerly deposited PS spheres. This sample preparation was done together with Dr. Tao Wang.

**Sample preparation of graphene-enhanced imaging.** Commercial CVD-grown monolayer graphene was ordered from ACS MATERIAL, LLC. The 500-nm thick PMMA layer is attached to protect and transfer the graphene onto the samples (the Au hole or the grating). The transfer process was done in the water. Typical Raman spectroscopy is used to characterize the monolayer graphene with the PMMA layer. The 2D-peak with a FWHM of 28 $cm^{-1}$ (Lorenz fit) is found at the position of 2680 $cm^{-1}$ (the 2D/G ratio is about 1.1), indicating an intrinsic n-doping (about 2 $\times$ $10^{13}$ $cm^{-2}$). This sample preparation was helped by Hannes Boeckmann and Dr. Tao Wang.

**Sample preparation of the hBN hyperlens.** The sample preparation was done by our collaborator, J. Caldwell. The gold nanostructures used for the near-field experiments were fabricated on a 1-$\mu$m-thick intrinsic silicon substrate using electron beam lithography into a bilayer PMMA resist. The nanostructures varied in size from 0.2 - 1 $\mu$m in diameter and in arrays with 0.1 - 1 $\mu$m edge-to-edge gaps. A standard liftoff procedure was used following the thermal evaporation of Cr (5 nm)/Au (30 nm) metallization.

Hexagonal BN crystals were grown using the high-pressure/high-temperature method [162, 163]. The standard exfoliation process was used to randomly deposit hBN flakes of various thicknesses onto a PMMA/PMGI bilayer spun on a separate silicon substrate. Here the PMMA layer played the role of the flake carrier membrane and the PMGI served as a sacrificial lift-off layer later dissolved by TMAH solution (MICROPOSIT® MF®-319). Atomic force microscopy was utilized to select specific flakes with both sufficient thickness and lateral size for the imaging experiments. The PMMA carrier membrane with an appropriate hBN flake was lifted-off from the substrate and put onto the supportive metal ring held by a home-made micromanipulator. With the help of the micromanipulator, the hBN flake was aligned and transferred face down onto the predefined gold nanostructure by releasing the carrier membrane from the metal ring. Following the transfer, the sample with the carrier membrane on was heated to 130°C for about 10 min to soften the PMMA membrane and improve the adhesion of hBN to the underlying nanostructures and silicon substrate. After that the carrier membrane was dissolved in acetone leaving the hBN flake covering the entire array of nanostructures. To improve the adhesion, an ultrasonic clean in acetone and isopropyl alcohol with subsequent oxygen plasma clean was performed on the silicon substrate prior to the hBN transfer. More details of this transfer technique are given in Ref. [164].

# B Theory Modeling

**Simulations of imaging dielectric objects.** I carried out electromagnetic simulations based on the finite element method (commercial software, COMSOL). The simulations are two-dimensional cases due to a limit of our computing resources. In all the simulations I modified the meshing size to ensure that the simulations reach proper convergence. In the simulations, an incident angle of 60° was used according to our experimental condition. For the cases needed to employ the scanning tip as discussed in Fig. 4.5f, the probing tip was modeled as an Au ellipse with the length $L = 600$ nm and the apex radius $a = 30$ nm.The tip end is 10-nm higher than the top surface of the SiC superlens. To simulate near-field imaging contrasts discussed in Fig. 4.7c and d, I first considered the case that the tip was on the top of the underlying PS sphere and obtained the simulated z-component of electric field $E_{z,s}$ from the bottom end of the tip. In a second simulation, I considered that the tip position was 2 $\mu$m away from the sphere and recorded the tip field $E_{z,o}$. Finally, I obtained the normalized amplitude contrasts ($|E_{z,s}|/|E_{z,o}|$) and phase contrasts (Arg($E_{z,s}$)-Arg($E_{z,o}$)).

To calculate the reflection contrasts discussed in Fig. 4.9 and 4.10, I used the total reflection coefficient $r$ of the air/SiC/object system as [165],

$$r = \frac{r_{12} + r_{23}\mathrm{e}^{2\mathrm{i}k_2 d}}{1 + r_{12}r_{23}\mathrm{e}^{2\mathrm{i}k_2 d}} \tag{B.1}$$

where $k_2 = \sqrt{\epsilon_{\mathrm{SiC}}k_0^2 - k_x^2}$. $r_{12}$ is the reflection coefficient at the air/SiC interface and $r_{23}$ is the reflection coefficient at the air/object interface. I used the equation of dielectric function of the SiC as [100]

$$\varepsilon_{\mathrm{SiC}} = \varepsilon_\infty(1 + \frac{f_{LO}^2 - f_{TO}^2}{f_{TO}^2 - if\gamma - f^2}) \tag{B.2}$$

where $\varepsilon_\infty = 6.5$, $f_{TO} = 796$ cm$^{-1}$, $f_{LO} = 972$ cm$^{-1}$. In the theoretical results shown in Fig. 4.9 and 4.10, $\gamma = 5$ cm$^{-1}$ is used for the best visualization of the reflection peaks corresponding to the SPhP modes. $\gamma = 30$ cm$^{-1}$ are assumed for the polycrystalline SiC used in Fig. 4.7c and d to fit the experimental results.

**Transmission calculation of graphene superlens.** To calculate the transmission of layered graphene lenses (Section 6.2), I use the transfer matrix method by treating graphene layers as ideal conducting sheets with surface conductivity $\sigma_g$. The characteristic matrix for the graphene can be obtained by using a mathematical trick similar with the process in Ref. [110]. First, I suppose the graphene layer with the thickness $\Delta$ has the equivalent complex permittivity $\varepsilon_{eq} = \varepsilon_0 + i\sigma_g/(\omega\Delta)$. Then I employ this equivalent permittivity with the thickness $\Delta$ into the commonly used characteristic matrix [165] for layered systems and let $\Delta \to 0$ . The thickness $\Delta$ will be cancelled in the formulas. Finally, I obtain the matrix of the graphene sheet as,

$$\begin{bmatrix} 1 & \sigma_g/\varepsilon_0\omega \\ 0 & 1 \end{bmatrix} \tag{B.3}$$

With this characteristic matrix, it is easier to calculate the transmission of any multilayered graphene superlenes.

I use a commercial software COMSOL based on the finite-element method to simulate the imaging performance of the graphene lens (Fig. 6.3). In the simulations, the graphene layer cannot be seen as the ideally thin sheet. So I assume that the thickness of graphene is 1 nm and use the corresponding permittivity $\varepsilon_{eq}$, taking into account the realistic surface conductivity of the graphene. For example, I obtain Re( $\varepsilon_{eq}$) $\approx$ - 720 at the frequency $f = 27.2$ THz for the graphene layer with chemical potential $\mu_c = 1.5$ eV. Due to the computation memory limitation introduced by the large mismatch between the ultrathin thickness and the long illuminating wavelength, the simulation is performed in two dimensions. The simulation domains have been assigned scattering properties following the same way as shown in [25], which act as the necessary open boundary conditions. all the simulations reached proper convergence.

**Simulations of imaging through hBN hyperlens.** 2D simulations (Fig. 7.2) were carried out by the finite-element software COMSOL Multiphysics. A plane-wave illumination was set by using scattering boundary condition. The surrounding boundaries used perfectly matched layer absorbing boundary conditions. 3D

simulations (Fig. 7.3) were done by using CST Microwave Studio$^{TM}$. Open boundary conditions were used. I also checked different mesh sizes to make sure that all the simulations reach proper convergence. The dielectric data of hBN used in all the simulations are extracted from far-field FTIR measurements [43].

# C Supplementary data

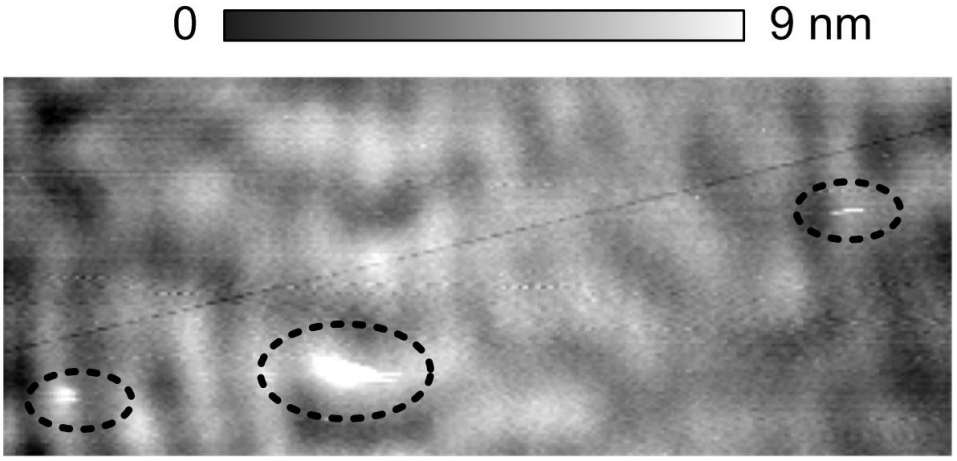


FIGURE C.1: The corrosponding topography image for the s-SNOM image (taken at the wavelength of 10.85 $\mu$m) shown in Fig. 4.7b. The dashed lines mark the mechanical artefacts appearing in the scans, which also cause the features in the s-SNOM image.

# Bibliography


[1] E. Abbe, "Beiträge zur Theorie des Mikroskops und der mikroskopischen Wahrnehmung," *Archiv für mikroskopische Anatomie*, vol. 9, no. 1, pp. 413–418, 1873.

[2] M. Knoll and E. Ruska, "Das Elektronenmikroskop," *Zeitschrift für Physik*, vol. 78, no. 5-6, pp. 318–339, 1932.

[3] D. B. Williams and C. B. Carter, *The transmission electron microscope*. Springer, 1996.

[4] A. Neice, "Methods and limitations of subwavelength imaging," *Advances in imaging and Electron Physics*, vol. 163, pp. 117–140, 2010.

[5] S. W. Hell and J. Wichmann, "Breaking the diffraction resolution limit by stimulated emission: stimulated-emission-depletion fluorescence microscopy," *Optics Letters*, vol. 19, no. 11, pp. 780–782, 1994.

[6] E. Betzig, G. H. Patterson, R. Sougrat, O. W. Lindwasser, S. Olenych, J. S. Bonifacino, M. W. Davidson, J. Lippincott-Schwartz, and H. F. Hess, "Imaging intracellular fluorescent proteins at nanometer resolution," *Science*, vol. 313, no. 5793, pp. 1642–1645, 2006.

[7] M. J. Rust, M. Bates, and X. Zhuang, "Sub-diffraction-limit imaging by stochastic optical reconstruction microscopy (STORM)," *Nature Methods*, vol. 3, no. 10, pp. 793–796, 2006.

[8] D. W. Pohl, W. Denk, and M. Lanz, "Optical stethoscopy: Image recording with resolution $\lambda/20$," *Applied Physics Letters*, vol. 44, no. 7, pp. 651–653, 1984.

[9] Y. Inouye and S. Kawata, "Near-field scanning optical microscope with a metallic probe tip," *Optics Letters*, vol. 19, no. 3, pp. 159–161, 1994.

[10] J. B. Pendry, "Negative refraction makes a perfect lens," *Physical Review Letters*, vol. 85, no. 18, p. 3966, 2000.

[11] X. Zhang and Z. Liu, "Superlenses to overcome the diffraction limit," *Nature Materials*, vol. 7, no. 6, pp. 435–441, 2008.

[12] J. Sun, J. Zhou, B. Li, and F. Kang, "Indefinite permittivity and negative refraction in natural material: Graphite," *Applied Physics Letters*, vol. 98, no. 10, p. 101901, 2011.

[13] X. Chen, M. He, Y. Du, W. Wang, and D. Zhang, "Negative refraction: an intrinsic property of uniaxial crystals," *Physical Review B*, vol. 72, no. 11, p. 113111, 2005.

[14] Y. Zhang, B. Fluegel, and A. Mascarenhas, "Total negative refraction in real crystals for ballistic electrons and light," *Physical Review Letters*, vol. 91, no. 15, p. 157404, 2003.

[15] R. A. Shelby, D. R. Smith, and S. Schultz, "Experimental verification of a negative index of refraction," *Science*, vol. 292, no. 5514, pp. 77–79, 2001.

[16] A. Grbic and G. V. Eleftheriades, "Overcoming the diffraction limit with a planar left-handed transmission-line lens," *Physical Review Letters*, vol. 92, no. 11, p. 117403, 2004.

[17] D. R. Smith, J. B. Pendry, and M. C. Wiltshire, "Metamaterials and negative refractive index," *Science*, vol. 305, no. 5685, pp. 788–792, 2004.

[18] V. M. Shalaev, "Optical negative-index metamaterials," *Nature Photonics*, vol. 1, no. 1, pp. 41–48, 2007.

[19] X. Rao and C. Ong, "Subwavelength imaging by a left-handed material superlens," *Physical Review E*, vol. 68, no. 6, p. 067601, 2003.

[20] E. Cubukcu, K. Aydin, E. Ozbay, S. Foteinopoulou, and C. Soukoulis, "Subwavelength resolution in a two-dimensional photonic-crystal-based superlens," *Physical Review Letters*, vol. 91, no. 20, p. 207401, 2003.

[21] A. A. Houck, J. B. Brock, and I. L. Chuang, "Experimental observations of a left-handed material that obeys snell's law," *Physical Review Letters*, vol. 90, no. 13, p. 137401, 2003.

[22] N. Fang, H. Lee, C. Sun, and X. Zhang, "Sub–diffraction-limited optical imaging with a silver superlens," *Science*, vol. 308, no. 5721, pp. 534–537, 2005.

[23] D. Melville and R. Blaikie, "Super-resolution imaging through a planar silver layer," *Optics Express*, vol. 13, no. 6, pp. 2127–2134, 2005.

[24] T. Taubner, D. Korobkin, Y. Urzhumov, G. Shvets, and R. Hillenbrand, "Near-field microscopy through a SiC superlens," *Science*, vol. 313, no. 5793, pp. 1595–1595, 2006.

[25] S. C. Kehr, Y. M. Liu, L. Martin, P. Yu, M. Gajek, S.-Y. Yang, C.-H. Yang, M. Wenzel, R. Jacob, H.-G. von Ribbeck, *et al.*, "Near-field examination of perovskite-based superlenses and superlens-enhanced probe-object coupling," *Nature Communications*, vol. 2, p. 249, 2011.

[26] S. C. Kehr, P. Yu, Y. Liu, M. Parzefall, A. I. Khan, R. Jacob, M. T. Wenzel, H.-G. von Ribbeck, M. Helm, X. Zhang, *et al.*, "Microspectroscopy on perovskite-based superlenses [invited]," *Optical Materials Express*, vol. 1, no. 5, pp. 1051–1060, 2011.

[27] M. Fehrenbacher, S. Winnerl, H. Schneider, J. Doering, S. C. Kehr, L. M. Eng, Y. Huo, O. G. Schmidt, K. Yao, Y. Liu, *et al.*, "Plasmonic superlensing in doped gaas," *Nano Letters*, vol. 15, no. 2, pp. 1057–1061, 2015.

[28] Z. Liu, S. Durant, H. Lee, Y. Pikus, N. Fang, Y. Xiong, C. Sun, and X. Zhang, "Far-field optical superlens," *Nano Letters*, vol. 7, no. 2, pp. 403–408, 2007.

[29] Z. Liu, S. Durant, H. Lee, Y. Pikus, Y. Xiong, C. Sun, and X. Zhang, "Experimental studies of far-field superlens for sub-diffractional optical imaging," *Optics Express*, vol. 15, no. 11, pp. 6947–6954, 2007.

[30] Y. Xiong, Z. Liu, S. Durant, H. Lee, C. Sun, and X. Zhang, "Tuning the far-field superlens: from uv to visible," *Optics Express*, vol. 15, no. 12, pp. 7095–7102, 2007.

[31] Y. Xiong, Z. Liu, C. Sun, and X. Zhang, "Two-dimensional imaging by far-field superlens at visible wavelengths," *Nano Letters*, vol. 7, no. 11, pp. 3360–3365, 2007.

[32] A. Poddubny, I. Iorsh, P. Belov, and Y. Kivshar, "Hyperbolic metamaterials," *Nature Photonics*, vol. 7, no. 12, pp. 948–957, 2013.

[33] Z. Jacob, L. V. Alekseyev, and E. Narimanov, "Optical hyperlens: far-field imaging beyond the diffraction limit," *Optics Express*, vol. 14, no. 18, pp. 8247–8256, 2006.

[34] A. Salandrino and N. Engheta, "Far-field subdiffraction optical microscopy using metamaterial crystals: Theory and simulations," *Physical Review B*, vol. 74, no. 7, p. 075103, 2006.

[35] Z. Liu, H. Lee, Y. Xiong, C. Sun, and X. Zhang, "Far-field optical hyperlens magnifying sub-diffraction-limited objects," *Science*, vol. 315, no. 5819, pp. 1686–1686, 2007.

[36] A. J. Hoffman, L. Alekseyev, S. S. Howard, K. J. Franz, D. Wasserman, V. A. Podolskiy, E. E. Narimanov, D. L. Sivco, and C. Gmachl, "Negative refraction in semiconductor metamaterials," *Nature Materials*, vol. 6, no. 12, pp. 946–950, 2007.

[37] J. Yao, Z. Liu, Y. Liu, Y. Wang, C. Sun, G. Bartal, A. M. Stacy, and X. Zhang, "Optical negative refraction in bulk metamaterials of nanowires," *Science*, vol. 321, no. 5891, pp. 930–930, 2008.

[38] S. Prokes, O. J. Glembocki, J. Livenere, T. Tumkur, J. Kitur, G. Zhu, B. Wells, V. Podolskiy, and M. Noginov, "Hyperbolic and plasmonic properties of Silicon/Ag aligned nanowire arrays," *Optics Express*, vol. 21, no. 12, pp. 14962–14974, 2013.

[39] H. N. Krishnamoorthy, Z. Jacob, E. Narimanov, I. Kretzschmar, and V. M. Menon, "Topological transitions in metamaterials," *Science*, vol. 336, no. 6078, pp. 205–209, 2012.

[40] S. Ishii, A. V. Kildishev, E. Narimanov, V. M. Shalaev, and V. P. Drachev, "Sub-wavelength interference pattern from volume plasmon polaritons in a hyperbolic medium," *Laser & Photonics Reviews*, vol. 7, no. 2, pp. 265–271, 2013.

[41] X. Yang, J. Yao, J. Rho, X. Yin, and X. Zhang, "Experimental realization of three-dimensional indefinite cavities at the nanoscale with anomalous scaling laws," *Nature Photonics*, vol. 6, no. 7, pp. 450–454, 2012.

[42] S. Dai, Z. Fei, Q. Ma, A. Rodin, M. Wagner, A. McLeod, M. Liu, W. Gannett, W. Regan, K. Watanabe, *et al.*, "Tunable phonon polaritons in atomically thin van der Waals crystals of boron nitride," *Science*, vol. 343, no. 6175, pp. 1125–1129, 2014.

[43] J. D. Caldwell, A. V. Kretinin, Y. Chen, V. Giannini, M. M. Fogler, Y. Francescato, C. T. Ellis, J. G. Tischler, C. R. Woods, A. J. Giles, *et al.*, "Sub-diffractional volume-confined polaritons in the natural hyperbolic material hexagonal boron nitride," *Nature Communications*, vol. 5, 2014.

[44] D. W. Thompson, M. J. DeVries, T. E. Tiwald, and J. A. Woollam, "Determination of optical anisotropy in calcite from ultraviolet to mid-infrared by generalized ellipsometry," *Thin Solid Films*, vol. 313, pp. 341–346, 1998.

[45] J. Sun, N. M. Litchinitser, and J. Zhou, "Indefinite by nature: from ultraviolet to terahertz," *ACS Photonics*, vol. 1, no. 4, pp. 293–303, 2014.

[46] A. V. Zayats, I. I. Smolyaninov, and A. A. Maradudin, "Nano-optics of surface plasmon polaritons," *Physics reports*, vol. 408, no. 3, pp. 131–314, 2005.

[47] S. A. Maier, *Plasmonics: fundamentals and applications: fundamentals and applications*. Springer Science & Business Media, 2007.

[48] E. Ozbay, "Plasmonics: merging photonics and electronics at nanoscale dimensions," *Science*, vol. 311, no. 5758, pp. 189–193, 2006.

[49] H. A. Atwater, "The promise of plasmonics," *Scientific American*, vol. 296, no. 4, pp. 56–62, 2007.

[50] H. A. Atwater and A. Polman, "Plasmonics for improved photovoltaic devices," *Nature Materials*, vol. 9, no. 3, pp. 205–213, 2010.

[51] D. K. Gramotnev and S. I. Bozhevolnyi, "Plasmonics beyond the diffraction limit," *Nature Photonics*, vol. 4, no. 2, pp. 83–91, 2010.

[52] J. A. Schuller, E. S. Barnard, W. Cai, Y. C. Jun, J. S. White, and M. L. Brongersma, "Plasmonics for extreme light concentration and manipulation," *Nature Materials*, vol. 9, no. 3, pp. 193–204, 2010.

[53] J. D. Caldwell, L. Lindsay, V. Giannini, I. Vurgaftman, T. L. Reinecke, S. A. Maier, and O. J. Glembocki, "Low-loss, infrared and terahertz nanophotonics using surface phonon polaritons," *Nanophotonics*, 2014.

[54] R. Hillenbrand, T. Taubner, and F. Keilmann, "Phonon-enhanced light–matter interaction at the nanometre scale," *Nature*, vol. 418, no. 6894, pp. 159–162, 2002.

[55] J.-J. Greffet, R. Carminati, K. Joulain, J.-P. Mulet, S. Mainguy, and Y. Chen, "Coherent emission of light by thermal sources," *Nature*, vol. 416, no. 6876, pp. 61–64, 2002.

[56] J. A. Schuller, R. Zia, T. Taubner, and M. L. Brongersma, "Dielectric metamaterials based on electric and magnetic resonances of silicon carbide particles," *Physical Review Letters*, vol. 99, no. 10, p. 107401, 2007.

[57] J. A. Schuller, T. Taubner, and M. L. Brongersma, "Optical antenna thermal emitters," *Nature Photonics*, vol. 3, no. 11, pp. 658–661, 2009.

[58] M. Ameen, A. Garcia-Etxarri, M. Schnell, R. Hillenbrand, and J. Aizpurua, "Infrared phononic nanoantennas: Localized surface phonon polaritons in sic disks," *Chinese Science Bulletin*, vol. 55, no. 24, pp. 2625–2628, 2010.

[59] J. D. Caldwell, O. J. Glembocki, Y. Francescato, N. Sharac, V. Giannini, F. J. Bezares, J. P. Long, J. C. Owrutsky, I. Vurgaftman, J. G. Tischler, *et al.*, "Low-loss, extreme subdiffraction photon confinement via silicon carbide localized surface phonon polariton resonators," *Nano Letters*, vol. 13, no. 8, pp. 3690–3697, 2013.

[60] T. Wang, P. Li, B. Hauer, D. N. Chigrin, and T. Taubner, "Optical properties of single infrared resonant circular microcavities for surface phonon polaritons," *Nano Letters*, vol. 13, no. 11, pp. 5051–5055, 2013.

[61] R. Merlin, "Analytical solution of the almost-perfect-lens problem," *Applied Physics Letters*, vol. 84, no. 8, pp. 1290–1292, 2004.

[62] A. S. McLeod, P. Kelly, M. Goldflam, Z. Gainsforth, A. J. Westphal, G. Dominguez, M. H. Thiemens, M. M. Fogler, and D. Basov, "Model for quantitative tip-enhanced spectroscopy and the extraction of nanoscale-resolved optical constants," *Physical Review B*, vol. 90, no. 8, p. 085136, 2014.

[63] N. Ocelic, A. Huber, and R. Hillenbrand, "Pseudoheterodyne detection for background-free near-field spectroscopy," *Applied Physics Letters*, vol. 89, no. 10, p. 101124, 2006.

[64] B. Hauer, "Nano-optical mapping of permittivity contrasts and electronic properties at the surface and beneath," *PhD thesis, RWTH Aachen Univeristy*, 2015.

[65] J. Faist, F. Capasso, D. L. Sivco, C. Sirtori, A. L. Hutchinson, and A. Y. Cho, "Quantum cascade laser," *Science*, vol. 264, no. 5158, pp. 553–556, 1994.

[66] J. Wueppen, B. Jungbluth, T. Taubner, and P. Loosen, "Ultrafast tunable mid-IR source," in *Infrared, Millimeter and Terahertz Waves (IRMMW-THz), 2011 36th International Conference on*, pp. 1–2, IEEE, 2011.

[67] S. Bensmann, F. Gaußmann, M. Lewin, J. Wüppen, S. Nyga, C. Janzen, B. Jungbluth, and T. Taubner, "Near-field imaging and spectroscopy of locally strained GaN using an ir broadband laser," *Optics Express*, vol. 22, no. 19, pp. 22369–22381, 2014.

[68] F. Huth, A. Govyadinov, S. Amarie, W. Nuansing, F. Keilmann, and R. Hillenbrand, "Nano-FTIR absorption spectroscopy of molecular fingerprints at 20 nm spatial resolution," *Nano Letters*, vol. 12, no. 8, pp. 3973–3978, 2012.

[69] S. Amarie, P. Zaslansky, Y. Kajihara, E. Griesshaber, W. W. Schmahl, and F. Keilmann, "Nano-FTIR chemical mapping of minerals in biological materials," *Beilstein journal of nanotechnology*, vol. 3, no. 1, pp. 312–323, 2012.

[70] B. Knoll and F. Keilmann, "Near-field probing of vibrational absorption for chemical microscopy," *Nature*, vol. 399, no. 6732, pp. 134–137, 1999.

[71] B. Knoll and F. Keilmann, "Enhanced dielectric contrast in scattering-type scanning near-field optical microscopy," *Optics Communications*, vol. 182, no. 4, pp. 321–328, 2000.

[72] J. D. Jackson and J. D. Jackson, *Classical electrodynamics*, vol. 3. Wiley New York etc., 1962.

[73] T. Taubner, R. Hillenbrand, and F. Keilmann, "Nanoscale polymer recognition by spectral signature in scattering infrared near-field microscopy," *Applied Physics Letters*, vol. 85, no. 21, pp. 5064–5066, 2004.

[74] A. J. Huber, F. Keilmann, J. Wittborn, J. Aizpurua, and R. Hillenbrand, "Terahertz near-field nanoscopy of mobile carriers in single semiconductor nanodevices," *Nano Letters*, vol. 8, no. 11, pp. 3766–3770, 2008.

[75] M. Schnell, A. Garcia-Etxarri, A. Huber, K. Crozier, J. Aizpurua, and R. Hillenbrand, "Controlling the near-field oscillations of loaded plasmonic nanoantennas," *Nature Photonics*, vol. 3, no. 5, pp. 287–291, 2009.

[76] M. Schnell, A. Garcia-Etxarri, J. Alkorta, J. Aizpurua, and R. Hillenbrand, "Phase-resolved mapping of the near-field vector and polarization state in nanoscale antenna gaps," *Nano Letters*, vol. 10, no. 9, pp. 3524–3528, 2010.

[77] A. Huber, N. Ocelic, D. Kazantsev, and R. Hillenbrand, "Near-field imaging of mid-infrared surface phonon polariton propagation," *Applied Physics Letters*, vol. 87, no. 8, p. 081103, 2005.

[78] J. Chen, M. Badioli, P. Alonso-González, S. Thongrattanasiri, F. Huth, J. Osmond, M. Spasenović, A. Centeno, A. Pesquera, P. Godignon, *et al.*, "Optical nano-imaging of gate-tunable graphene plasmons," *Nature*, vol. 487, no. 7405, pp. 77–81, 2012.

[79] Z. Fei, A. Rodin, G. Andreev, W. Bao, A. McLeod, M. Wagner, L. Zhang, Z. Zhao, M. Thiemens, G. Dominguez, *et al.*, "Gate-tuning of graphene plasmons revealed by infrared nano-imaging," *Nature*, vol. 487, no. 7405, pp. 82–85, 2012.

[80] S. Dai, Q. Ma, S.-E. Zhu, M. Liu, T. Andersen, Z. Fei, M. Goldflam, M. Wagner, K. Watanabe, T. Taniguchi, *et al.*, "Graphene on hexagonal boron nitride as an agile hyperbolic metamaterial," *arXiv preprint arXiv:1501.06956*, 2015.

[81] S. Dai, Q. Ma, T. Andersen, A. Mcleod, Z. Fei, M. Liu, M. Wagner, K. Watanabe, T. Taniguchi, M. Thiemens, *et al.*, "Subdiffractional focusing and guiding of polaritonic rays in a natural hyperbolic material," *Nature communications*, vol. 6, p. 6963, 2015.

[82] P. Li, T. Wang, H. Boeckmann, and T. Taubner, "Graphene-enhanced infrared near-field microscopy," *Nano Letters*, vol. 14, no. 8, pp. 4400–4405, 2014.

[83] A. García-Etxarri, I. Romero, F. J. G. de Abajo, R. Hillenbrand, and J. Aizpurua, "Influence of the tip in near-field imaging of nanoparticle plasmonic modes: Weak and strong coupling regimes," *Physical Review B*, vol. 79, no. 12, p. 125439, 2009.

[84] A. Cvitkovic, N. Ocelic, and R. Hillenbrand, "Analytical model for quantitative prediction of material contrasts in scattering-type near-field optical microscopy," *Optics Express*, vol. 15, no. 14, pp. 8550–8565, 2007.

[85] T. Taubner, F. Keilmann, and R. Hillenbrand, "Nanoscale-resolved subsurface imaging by scattering-type near-field optical microscopy," *Optics Express*, vol. 13, no. 22, pp. 8893–8899, 2005.

[86] L. M. Zhang, G. O. Andreev, Z. Fei, A. S. McLeod, G. Dominguez, M. Thiemens, A. Castro-Neto, D. Basov, and M. M. Fogler, "Near-field spectroscopy of silicon dioxide thin films," *Physical Review B*, vol. 85, no. 7, p. 075419, 2012.

[87] B. Hauer, A. P. Engelhardt, and T. Taubner, "Quasi-analytical model for scattering infrared near-field microscopy on layered systems," *Optics Express*, vol. 20, no. 12, pp. 13173–13188, 2012.

[88] A. Cvitkovic, N. Ocelic, J. Aizpurua, R. Guckenberger, and R. Hillenbrand, "Infrared imaging of single nanoparticles via strong field enhancement in a scanning nanogap," *Physical Review Letters*, vol. 97, no. 6, p. 060801, 2006.

[89] Z. Liu, N. Fang, T.-J. Yen, and X. Zhang, "Rapid growth of evanescent wave by a silver superlens," *Applied Physics Letters*, vol. 83, no. 25, pp. 5184–5186, 2003.

[90] N. Fang, Z. Liu, T.-J. Yen, and X. Zhang, "Regenerating evanescent waves from a silver superlens," *Optics Express*, vol. 11, no. 7, pp. 682–687, 2003.

[91] M. Brehm, T. Taubner, R. Hillenbrand, and F. Keilmann, "Infrared spectroscopic mapping of single nanoparticles and viruses at nanoscale resolution," *Nano Letters*, vol. 6, no. 7, pp. 1307–1310, 2006.

[92] H. Liu, B. Wang, L. Ke, J. Deng, C. C. Chum, S. L. Teo, L. Shen, S. A. Maier, and J. Teng, "High aspect subdiffraction-limit photolithography via a silver superlens," *Nano Letters*, vol. 12, no. 3, pp. 1549–1554, 2012.

[93] H. Liu, B. Wang, L. Ke, J. Deng, C. C. Choy, M. S. Zhang, L. Shen, S. A. Maier, and J. H. Teng, "High contrast superlens lithography engineered by loss reduction," *Advanced Functional Materials*, vol. 22, no. 18, pp. 3777–3783, 2012.

[94] A. P. Engelhardt, B. Hauer, and T. Taubner, "Visibility of weak contrasts in subsurface scattering near-field microscopy," *Ultramicroscopy*, vol. 126, pp. 40–43, 2013.

[95] R. Krutokhvostov, A. A. Govyadinov, J. M. Stiegler, F. Huth, A. Chuvilin, P. S. Carney, and R. Hillenbrand, "Enhanced resolution in subsurface near-field optical microscopy," *Optics Express*, vol. 20, no. 1, pp. 593–600, 2012.

[96] J. Stiegler, A. Huber, S. Diedenhofen, J. Gomez Rivas, R. Algra, E. Bakkers, and R. Hillenbrand, "Nanoscale free-carrier profiling of individual semiconductor nanowires by infrared near-field nanoscopy," *Nano Letters*, vol. 10, no. 4, pp. 1387–1392, 2010.

[97] P. A. Belov, C. R. Simovski, and P. Ikonen, "Canalization of subwavelength images by electromagnetic crystals," *Physical Review B*, vol. 71, no. 19, p. 193105, 2005.

[98] B. Wood, J. Pendry, and D. Tsai, "Directed subwavelength imaging using a layered metal-dielectric system," *Physical Review B*, vol. 74, no. 11, p. 115116, 2006.

[99] X. Li, S. He, and Y. Jin, "Subwavelength focusing with a multilayered fabry-perot structure at optical frequencies," *Physical Review B*, vol. 75, no. 4, p. 045103, 2007.

[100] E. D. Palik, *Handbook of optical constants of solids*, vol. 3. Academic press, 1998.

[101] P. R. West, S. Ishii, G. V. Naik, N. K. Emani, V. M. Shalaev, and A. Boltasseva, "Searching for better plasmonic materials," *Laser & Photonics Reviews*, vol. 4, no. 6, pp. 795–808, 2010.

[102] A. Boltasseva and H. A. Atwater, "Low-loss plasmonic metamaterials," *Science*, vol. 331, no. 6015, pp. 290–291, 2011.

[103] S. Law, V. Podolskiy, and D. Wasserman, "Towards nano-scale photonics with micro-scale photons: the opportunities and challenges of mid-infrared plasmonics," *Nanophotonics*, vol. 2, no. 2, pp. 103–130, 2013.

[104] K. Novoselov, A. K. Geim, S. V. B. Morozov, D. Jiang, M. I. K. I. V. Grigorieva, S. V. Dubonos, and A. A. Firsov, "Two-dimensional gas of massless dirac fermions in graphene," *Nature*, vol. 438, no. 7065, pp. 197–200, 2005.

[105] A. K. Geim and K. S. Novoselov, "The rise of graphene," *Nature Materials*, vol. 6, no. 3, pp. 183–191, 2007.

[106] Z. Fei, G. O. Andreev, W. Bao, L. M. Zhang, A. S. McLeod, C. Wang, M. K. Stewart, Z. Zhao, G. Dominguez, M. Thiemens, *et al.*, "Infrared nanoscopy of dirac plasmons at the graphene–$SiO_2$ interface," *Nano Letters*, vol. 11, no. 11, pp. 4701–4705, 2011.

[107] P. Li and T. Taubner, "Broadband subwavelength imaging using a tunable graphene-lens," *ACS Nano*, vol. 6, no. 11, pp. 10107–10114, 2012.

[108] A. Grigorenko, M. Polini, and K. Novoselov, "Graphene plasmonics," *Nature Photonics*, vol. 6, no. 11, pp. 749–758, 2012.

[109] F. J. G. de Abajo, "Graphene nanophotonics," *Science*, vol. 339, no. 6122, pp. 917–918, 2013.

[110] A. Vakil and N. Engheta, "Transformation optics using graphene," *Science*, vol. 332, no. 6035, pp. 1291–1294, 2011.

[111] P.-Y. Chen and A. Alù, "Atomically thin surface cloak using graphene monolayers," *ACS Nano*, vol. 5, no. 7, pp. 5855–5863, 2011.

[112] S. Thongrattanasiri, F. H. L. Koppens, and F. J. G. de Abajo, "Complete optical absorption in periodically patterned graphene," *Physical Review Letters*, vol. 108, no. 4, p. 047401, 2012.

[113] E. H. Hwang and S. D. Sarma, "Dielectric function, screening, and plasmons in two-dimensional graphene," *Physical Review B*, vol. 75, no. 20, p. 205418, 2007.

[114] L. Ju, B. Geng, J. Horng, C. Girit, M. Martin, Z. Hao, H. A. Bechtel, X. Liang, A. Zettl, Y. R. Shen, *et al.*, "Graphene plasmonics for tunable terahertz metamaterials," *Nature Nanotechnology*, vol. 6, no. 10, pp. 630–634, 2011.

[115] F. H. Koppens, D. E. Chang, and F. J. Garcia de Abajo, "Graphene plasmonics: a platform for strong light–matter interactions," *Nano Letters*, vol. 11, no. 8, pp. 3370–3377, 2011.

[116] X. Luo, T. Qiu, W. Lu, and Z. Ni, "Plasmons in graphene: Recent progress and applications," *Materials Science and Engineering: R: Reports*, vol. 74, no. 11, pp. 351–376, 2013.

[117] S. A. Ramakrishna, J. Pendry, D. Schurig, D. Smith, and S. Schultz, "The asymmetric lossy near-perfect lens," *journal of modern optics*, vol. 49, no. 10, pp. 1747–1762, 2002.

[118] P. Li and Y. Liu, "Multichannel filtering properties of photonic crystals consisting of single-negative materials," *Physics Letters A*, vol. 373, no. 21, pp. 1870–1873, 2009.

[119] J. Ye, M. F. Craciun, M. Koshino, S. Russo, S. Inoue, H. Yuan, H. Shimotani, A. F. Morpurgo, and Y. Iwasa, "Accessing the transport properties of graphene and its multilayers at high carrier density," *Proceedings of the National Academy of Sciences*, vol. 108, no. 32, pp. 13002–13006, 2011.

[120] D. K. Efetov and P. Kim, "Controlling electron-phonon interactions in graphene at ultrahigh carrier densities," *Physical Review Letters*, vol. 105, no. 25, p. 256805, 2010.

[121] A. Woessner, M. B. Lundeberg, Y. Gao, A. Principi, P. Alonso-González, M. Carrega, K. Watanabe, T. Taniguchi, G. Vignale, M. Polini, *et al.*, "Highly confined low-loss plasmons in graphene–boron nitride heterostructures," *Nature Materials*, vol. 14, pp. 421–425, 2014.

[122] J. Wang, Y. Xu, H. Chen, and B. Zhang, "Ultraviolet dielectric hyperlens with layered graphene and boron nitride," *Journal of Materials Chemistry*, vol. 22, no. 31, pp. 15863–15868, 2012.

[123] I. V. Iorsh, I. S. Mukhin, I. V. Shadrivov, P. A. Belov, and Y. S. Kivshar, "Hyperbolic metamaterials based on multilayer graphene structures," *Physical Review B*, vol. 87, no. 7, p. 075416, 2013.

[124] Y. Liu and R. F. Willis, "Plasmon-phonon strongly coupled mode in epitaxial graphene," *Physical Review B*, vol. 81, no. 8, p. 081406, 2010.

[125] E. Hwang, R. Sensarma, and S. D. Sarma, "Plasmon-phonon coupling in graphene," *Physical Review B*, vol. 82, no. 19, p. 195406, 2010.

[126] R. Koch, T. Seyller, and J. Schaefer, "Strong phonon-plasmon coupled modes in the graphene/silicon carbide heterosystem," *Physical Review B*, vol. 82, no. 20, p. 201413, 2010.

[127] V. W. Brar, M. S. Jang, M. Sherrott, J. J. Lopez, and H. A. Atwater, "Highly confined tunable mid-infrared plasmonics in graphene nanoresonators," *Nano Letters*, vol. 13, no. 6, pp. 2541–2547, 2013.

[128] V. W. Brar, M. Jang, M. Sherrott, S. Kim, J. Lopez, L. Kim, M. Choi, and H. A. Atwater, "Hybrid surface-phonon-plasmon polariton modes in graphene/monolayer h-BN heterostructures," *Nano Letters*, pp. 2541–2547, 2014.

[129] J. D. Caldwell, T. J. Anderson, J. C. Culbertson, G. G. Jernigan, K. D. Hobart, F. J. Kub, M. J. Tadjer, J. L. Tedesco, J. K. Hite, M. A. Mastro, *et al.*, "Technique for the dry transfer of epitaxial graphene onto arbitrary substrates," *ACS Nano*, vol. 4, no. 2, pp. 1108–1114, 2010.

[130] J. W. Suk, A. Kitt, C. W. Magnuson, Y. Hao, S. Ahmed, J. An, A. K. Swan, B. B. Goldberg, and R. S. Ruoff, "Transfer of CVD-grown monolayer graphene onto arbitrary substrates," *ACS Nano*, vol. 5, no. 9, pp. 6916–6924, 2011.

[131] Y. Ren, C. Zhu, W. Cai, H. Li, Y. Hao, Y. Wu, S. Chen, Q. Wu, R. D. Piner, and R. S. Ruoff, "An improved method for transferring graphene grown by chemical vapor deposition," *Nano*, vol. 7, no. 01, 2012.

[132] V. Geringer, D. Subramaniam, A. Michel, B. Szafranek, D. Schall, A. Georgi, T. Mashoff, D. Neumaier, M. Liebmann, and M. Morgenstern, "Electrical

transport and low-temperature scanning tunneling microscopy of microsoldered graphene," *Applied Physics Letters*, vol. 96, no. 8, pp. 082114–082114, 2010.

[133] A. Principi, G. Vignale, M. Carrega, and M. Polini, "Impact of disorder on dirac plasmon losses," *Physical Review B*, vol. 88, no. 12, p. 121405, 2013.

[134] H. Yan, T. Low, W. Zhu, Y. Wu, M. Freitag, X. Li, F. Guinea, P. Avouris, and F. Xia, "Damping pathways of mid-infrared plasmons in graphene nanostructures," *Nature Photonics*, vol. 7, no. 5, pp. 394–399, 2013.

[135] A. Principi, G. Vignale, M. Carrega, and M. Polini, "Intrinsic lifetime of dirac plasmons in graphene," *Physical Review B*, vol. 88, no. 19, p. 195405, 2013.

[136] P. Tassin, T. Koschny, and C. M. Soukoulis, "Graphene for terahertz applications," *Science*, vol. 1242253, no. 620, p. 341, 2013.

[137] Z. Fei, A. Rodin, W. Gannett, S. Dai, W. Regan, M. Wagner, M. Liu, A. McLeod, G. Dominguez, M. Thiemens, *et al.*, "Electronic and plasmonic phenomena at graphene grain boundaries," *Nature Nanotechnology*, vol. 8, no. 11, pp. 821–825, 2013.

[138] J. Chen, M. L. Nesterov, A. Y. Nikitin, S. Thongrattanasiri, P. Alonso-González, T. M. Slipchenko, F. Speck, M. Ostler, T. Seyller, I. Crassee, *et al.*, "Strong plasmon reflection at nanometer-size gaps in monolayer graphene on sic," *Nano Letters*, vol. 13, no. 12, pp. 6210–6215, 2013.

[139] F. Schwierz, "Graphene transistors," *Nature Nanotechnology*, vol. 5, no. 7, pp. 487–496, 2010.

[140] A. Ohtomo and H. Hwang, "A high-mobility electron gas at the $LaAlO_3/SrTiO_3$ heterointerface," *Nature*, vol. 427, no. 6973, pp. 423–426, 2004.

[141] J. Stiegler, R. Tena-Zaera, O. Idigoras, A. Chuvilin, and R. Hillenbrand, "Correlative infrared–electron nanoscopy reveals the local structure–conductivity relationship in zinc oxide nanowires," *Nature Communications*, vol. 3, p. 1131, 2012.

[142] O. Khatib, J. D. Wood, A. S. McLeod, M. D. Goldflam, M. Wagner, G. L. Damhorst, J. C. Koepke, G. P. Doidge, A. Rangarajan, R. Bashir, *et al.*, "Graphene-based platform for infrared near-field nanospectroscopy of water and biological materials in an aqueous environment," *ACS Nano*, vol. 9, no. 8, pp. 7968–7975, 2015.

[143] Z. Fang, S. Thongrattanasiri, A. Schlather, Z. Liu, L. Ma, Y. Wang, P. M. Ajayan, P. Nordlander, N. J. Halas, and F. J. García de Abajo, "Gated tunability and hybridization of localized plasmons in nanostructured graphene," *ACS Nano*, vol. 7, no. 3, pp. 2388–2395, 2013.

[144] Z. Fang, Y. Wang, A. E. Schlather, Z. Liu, P. M. Ajayan, F. J. GGarcía Abajo, P. Nordlander, X. Zhu, and N. J. Halas, "Active tunable absorption enhancement with graphene nanodisk arrays," *Nano Letters*, vol. 14, no. 1, pp. 299–304, 2013.

[145] J. B. Khurgin and A. Boltasseva, "Reflecting upon the losses in plasmonics and metamaterials," *MRS bulletin*, vol. 37, no. 08, pp. 768–779, 2012.

[146] P. R. West, S. Ishii, G. V. Naik, N. K. Emani, V. M. Shalaev, and A. Boltasseva, "Searching for better plasmonic materials," *Laser & Photonics Reviews*, vol. 4, no. 6, pp. 795–808, 2010.

[147] P. Tassin, T. Koschny, M. Kafesaki, and C. M. Soukoulis, "A comparison of graphene, superconductors and metals as conductors for metamaterials and plasmonics," *Nature Photonics*, vol. 6, no. 4, pp. 259–264, 2012.

[148] Y. Chen, Y. Francescato, J. D. Caldwell, V. Giannini, T. W. Maß, O. J. Glembocki, F. J. Bezares, T. Taubner, R. Kasica, M. Hong, *et al.*, "Spectral tuning of localized surface phonon polariton resonators for low-loss mid-ir applications," *ACS Photonics*, vol. 1, no. 8, pp. 718–724, 2014.

[149] X. G. Xu, B. G. Ghamsari, J.-H. Jiang, L. Gilburd, G. O. Andreev, C. Zhi, Y. Bando, D. Golberg, P. Berini, and G. C. Walker, "One-dimensional surface phonon polaritons in boron nitride nanotubes," *Nature Communications*, vol. 5, p. 4782, 2014.

[150] R. E. da Silva, R. Macêdo, T. Dumelow, J. da Costa, S. Honorato, and A. Ayala, "Far-infrared slab lensing and subwavelength imaging in crystal quartz," *Physical Review B*, vol. 86, no. 15, p. 155152, 2012.

[151] V. A. Fonoberov and A. A. Balandin, "Polar optical phonons in wurtzite spheroidal quantum dots: theory and application to ZnO and ZnO / MgZnO nanostructures," *Journal of Physics: Condensed Matter*, vol. 17, no. 7, p. 1085, 2005.

[152] R. Geick, C. Perry, and G. Rupprecht, "Normal modes in hexagonal boron nitride," *Physical Review*, vol. 146, no. 2, p. 543, 1966.

[153] A. Geim and I. Grigorieva, "Van der Waals heterostructures," *Nature*, vol. 499, no. 7459, pp. 419–425, 2013.

[154] A. Archambault, M. Besbes, and J.-J. Greffet, "Superlens in the time domain," *Physical Review Letters*, vol. 109, no. 9, p. 097405, 2012.

[155] M. Müller, A. Gumprich, F. Schütte, K. Kallis, U. Künzelmann, S. Engels, C. Stampfer, N. Wilck, and J. Knoch, "Buried triple-gate structures for advanced field-effect transistor devices," *Microelectronic Engineering*, vol. 119, pp. 95–99, 2014.

[156] T. Takeuchi, H. Amano, K. Hiramatsu, N. Sawaki, and I. Akasaki, "Growth of single crystalline GaN film on Si substrate using 3C-SiC as an intermediate layer," *Journal of Crystal Growth*, vol. 115, no. 1, pp. 634–638, 1991.

[157] A.-K. U. Michel, D. N. Chigrin, T. W. Mass, K. Schoenauer, M. Salinga, M. Wuttig, and T. Taubner, "Using low-loss phase-change materials for mid-infrared antenna resonance tuning," *Nano Letters*, vol. 13, no. 8, pp. 3470–3475, 2013.

[158] A.-K. U. Michel, P. Zalden, D. N. Chigrin, M. Wuttig, A. M. Lindenberg, and T. Taubner, "Reversible optical switching of infrared antenna resonances with ultrathin phase-change layers using femtosecond laser pulses," *ACS Photonics*, vol. 1, no. 9, pp. 833–839, 2014.

[159] G. Bruns, P. Merkelbach, C. Schlockermann, M. Salinga, M. Wuttig, T. Happ, J. Philipp, and M. Kund, "Nanosecond switching in GeTe phase change memory cells," *Applied Physics Letters*, vol. 95, no. 4, p. 043108, 2009.

[160] D. Loke, T. Lee, W. Wang, L. Shi, R. Zhao, Y. Yeo, T. Chong, and S. Elliott, "Breaking the speed limits of phase-change memory," *Science*, vol. 336, no. 6088, pp. 1566–1569, 2012.

[161] P. Li, X. Yang, T. W. Mass, A.-K. U. Michel, T. Kalix, A. De Rose, M. Salinga, M. Wuttig, and T. Taubner, "All-optical, non-volatile, reversible switching of highly confined surface polaritons with an ultrathin phase change material," *Submitted*, 2015.

[162] T. Taniguchi and K. Watanabe, "Synthesis of high-purity boron nitride single crystals under high pressure by using ba–bn solvent," *Journal of crystal growth*, vol. 303, no. 2, pp. 525–529, 2007.

[163] K. Watanabe, T. Taniguchi, and H. Kanda, "Direct-bandgap properties and evidence for ultraviolet lasing of hexagonal boron nitride single crystal," *Nature Materials*, vol. 3, no. 6, pp. 404–409, 2004.

[164] A. V. Kretinin, Y. Cao, J.-S. Tu, G. Yu, R. Jalil, K. S. Novoselov, S. Haigh, A. Gholinia, A. Mishchenko, M. Lozada, *et al.*, "Electronic properties of graphene encapsulated with different two-dimensional atomic crystals," *Nano Letters*, vol. 14, no. 6, pp. 3270–3276, 2014.

[165] M. Born and E. Wolf, *Principles of optics: electromagnetic theory of propagation, interference and diffraction of light*. Cambridge university press, 1999.

# List of Own Publications

### Thesis related

[P1] **P. Li** and T.Taubner, "Multi-wavelength superlensing with layered phonon-resonant dielectrics", *Optics Express*, vol. 20, no. 11, pp. 11787−11795, 2012.

[P2] **P. Li** and T. Taubner, "Broadband subwavelength imaging using a tunable graphene-lens", *ACS Nano*, vol. 6, no. 11, pp. 10107−10114, 2012.

[P3] **P. Li**, T. Wang, H. Boeckmann, and T. Taubner, "Graphene-enhanced infrared near-field microscopy", *Nano Letters*, vol. 14, no. 8, pp. 4400−4405, 2014.

[P4] **P. Li**, M. Lewin, A. V. Kretinin, J. D. Caldwell, K. S. Novoselov, T. Taniguchi, K. Watanabe, F. Gaussmann, T. Taubner, "Hyperbolic phonon-polaritons in boron nitride for near-field optical imaging and focusing", *Nature Communications*, vol.6, 7507, 2015.

### Other publications during the thesis study

[P5] T. Wang, **P. Li**, B. Hauer, D. N. Chigrin, T. Taubner, "Optical properties of single infrared resonant circular microcavities for surface phonon polaritons", *Nano Letters*, vol. 13, no. 11, pp. 5051−5055, 2013.

[P6] D. Shang, **P. Li**, T. Wang, E. Carria, J. Sun, B. Shen, T. Taubner, I. Valov, R. Waser, M. Wuttig, "Understanding the conductive channel evolution in Na:WO $_{3-x}$-based planar devices", *Nanoscale*, vol. 7, no. 14, pp. 6023−6030, 2015.

[P7] **P. Li**, X. Yang, T. Maß, A. U. Michel, M. Wuttig, T. Taubner, "Optical reversible switching of highly confined surface polaritons with an ultrathin phase change material", Submitted.

[P8] T. Wang, **P. Li**, D. N. Chigrin, J. D. Caldwell, T. Taubner, "Phononic bowtie nanoantennas: controlling ultra-narrow-band infrared thermal radiation at the nanoscale", Submitted.

# Acknowledgements

It is the time to express my sincere gratitude to everyone who supported me during my studies. I really appreciate your help and encourages.

First of all, I would like to thank my supervisor, Prof. Dr. Thomas Taubner. I really remember the first time that we met in Beijing during the NFO-11 conference, 2010. Thank you for providing me the opportunity to join your group and conduct my PhD studies. I thank your patient and inspiring advices and guidances over my studies. I enjoy the free studying environment that you create in the group. Together with state-of-art experimental conditions that your provide, I can perform these experiments presented in the thesis. I also thank your support for the nine academic conferences that I attended, which is a great number for a student. The time I was with you not only broadens my scientific knowledge, but also teaches me the positive and optimistic attitude in life.

I thank Prof. Dr. Matthias Wuttig, the head of our institute, for the perfect facilities and environment. I thank the scientific talks and seminars that he invited, from which I extend my research insight and also learn the research attitude from both speakers and him. I thank Prof. Dr. Gero von Plessen for being my thesis reporter. I also thank his valuable advices in the regular plasmonic meetings. I thank your careful and constructive comments for the proof reading of our manuscripts.

Importantly, my colleagues created an enjoyable and inspiring atmosphere over the years. For this I thank Stefanie Bensmann, Dr. Fabian Gaußmann, Xinghui Yin, Jón Mattis Hoffmann, Dr. Benedikt Hauer, Ann-Katrin Michel, Dr. Tao Wang, Dr. Dmitry Chigrin, Tobias Maß, Lena Jung, Martin Lewin. I also thank the students, Andreas Engelhardt, Kathrin Schönauer, Jens Richter, Hendrik Janssen, Michael Smeets, Hannes Böckmann, Zhao Chao, Alfred van Munster, Thomas Kalix, Tianchi Xu, Xiaosheng Yang, Angela De Rose, Johannes Reindl, Mike

Prämassing. A special thank is to Tao for the experiments that we performed together in the laboratory. I also would like to thank the other colleagues in the Institute of Physics 1A for the help and the support during my studies.

I thank our collaborator, Dr. Joshua D. Caldwell, for providing the nice samples and the active communications.

I would like to thank my Chinese friends in Aachen, Dr. We Zhang and Lei Li, Dr. Dashan Shang and his family, Chao Chen, Dr. Ming Xu, Dr. Rui Lan, Zhe Yang. I enjoy our funny time.

I would like to thank the most important supports from my family. I would like to thank my parents, Ronghua Pei and Gaochao Li, for their selfless support of my PhD studies abroad. For them, being so far away from their son is really tough. I would like to say a big thank to my wife, Ju Chai. Thank you for always being my strongest supporter. Thank you for giving those encourages when I was lost in the failures. Thank you for coming to Aachen and staying with me. You make me to enjoy my life in Germany.

*Thank you very much!*

*Danke schön!*